Modeling Polarized Radiances Toward the Development of an Aerosol Retrieval Method

By
Matthew Lebsock and Graeme L. Stephens

Department of Atmospheric Science
Colorado State University
Fort Collins, Colorado

Research was supported through the Ball Aerospace-CSU Joint Research program under Agreement #PO 03DLB10045.

Colorado State University

Department of Atmospheric Science

Paper No. 761

MODELING POLARIZED RADIANCES TOWARDS THE DEVELOPMENT OF AN AEROSOL RETRIEVAL METHOD

Matthew Lebsock and Graeme L. Stephens

Research supported through the Ball Aerospace-Colorado State University Joint Research Program under Agreement # PO 03DLB10045

MODELING POLARIZED RADIANCES TOWARDS THE DEVELOPMENT OF AN AEROSOL RETRIEVAL METHOD

Matthew Lebsock and Graeme L. Stephens

Research Supported by the Ball Aerospace-Colorado State University Joint Research Program

Principal Investigator: Graeme L. Stephens

Department of Atmospheric Science
Colorado State University
Fort Collins, CO 80523

October, 2005

Atmospheric Science Paper No. 761

ABSTRACT

MODELING POLARIZED RADIANCES TOWARDS THE DEVELOPMENT OF AN AEROSOL RETRIEVAL METHOD

Polarized radiances reflected from aerosol laden atmospheres were modeled. An atmospheric aerosol model was defined which corresponds to a clean oceanic environment composed mainly of sulfate particles. This model specifies an aerosol size distribution and optical properties. Fifteen atmospheric scenes composed of varying solar zenith angles and aerosol optical depths were defined to explore the scene dependent nature of the top of the atmosphere total and polarized radiances. The sensitivity of the forward model to aerosol optical depth was examined for these fifteen cases. A comprehensive error assessment was also performed for each of the fifteen cases. This assessment included the explicit modeling of errors due to aerosol model assumptions. The sensitivities were combined with the error estimates to produce signal to noise ratios for each scene. The signal to noise ratio demonstrates a significant viewing angle dependence for all of the fifteen cases. It was found that the angles with the largest signal to noise ratio for the total radiance are in the backscatter direction while angles in the sun glint demonstrated the lowest signal to noise ratio. It was also observed that the model sensitivity tends to decrease with optical depth while errors are shown to increase with optical.

Consequently, the signal to noise ratio tends to decrease strongly with optical depth. Finally, it was found that the signal to noise ratio for the total radiances tends to be about three times as large as the polarized radiances.

The total error estimates are used to develop an optimal estimation two-channel optical depth retrieval. Due to the greater signal to noise ratio of the total radiances, the polarized radiances were not used in the retrieval. Synthetic data were created to test the retrieval functionality. Two sources of bias were demonstrated. First, an a priori bias was shown which biases the retrieval towards the a priori initial guess. A second source of bias is introduced through the necessity to assume an aerosol model. It is demonstrated that these assumptions may bias the retrieval either high or low. Viewing geometries with small signal to noise ratios are shown to have a larger bias than those with large signal to noise ratio. It was concluded that the ideal multi-angular retrieval will utilize viewing geometries with large signal to noise ratios to limit the degree of the above biases. Finally, the retrieval is applied to a small sampling of POLDER II radiance data. The retrieved optical depths tend to be in qualitatively good agreement with the POLDER optical depths.

Matthew Lebsock
Atmospheric Science Department
Colorado State University
Fort Collins, Co 80523
Fall 2005

ACKNOWLEDGEMENTS

We would like to thank Drs. Christian Kummerow and Steven Reising for their evaluation of this work. Thanks are also due to Drs. Phillip Gabriel, Tristan L'Ecuyer and Steve Cooper for their many insightful comments and suggestions. This work was supported through the Ball Aerospace-Colorado State University Joint Research Program/Fellowship under agreement # PO 03DLB10045.

CONTENTS

CHAPTER 1

INTRODUCTION

1.1 The Importance of Aerosols in Climate

Aerosols are a ubiquitous feature of the Earth's atmosphere. A multitude of natural sources exist for aerosols from wind generated disintegration of the surface to gas to particle conversions. The two primary sinks for aerosols are dry and wet deposition back to the Earth's surface. Despite the large natural background aerosol concentrations, human activities have modified the aerosol content of the atmosphere through industrialization and land use changes. As the lifetime of an atmospheric aerosol is on the order of minutes to days, the anthropogenic aerosol burden represents a short lived but persistent forcing of the climate system.

Understanding and quantifying the effects of aerosols on the climate system remains a significant challenge for the scientific community. The radiative effect of anthropogenic changes to aerosol concentrations has the largest single uncertainty of any single climate forcing, IPCC (2001). The large uncertainty associated with the effects of anthropogenic aerosols on the climate system stems from several difficulties. First, there are difficulties in quantifying the increase in aerosol numbers due to anthropogenic effects relative to natural sources. Second, our current ability to observe aerosol properties on the global scale is less than satisfactory. Third,

the secondary effects of aerosols on the climate have proven to be extremely difficult to observe and quantify with any reliability, Schwartz (2004).

Three primary pathways for interaction of aerosols with the climate system have been identified in the literature, King et al. (1999). The first order, direct effect, of aerosols is to scatter and absorb incident solar radiation. These first order effects may in turn affect heating rates and subsequently alter the atmospheric circulation. It has also been proposed that aerosols have a secondary, or indirect effect on atmospheric radiation, Twomey (1977). The theory is that increased aerosol concentrations produce increased numbers of cloud condensation nuclei (CCN). The increased number of CCN inhibit the growth of large cloud droplets through water vapor competition. The result is clouds with an increased number of small droplets. These clouds will be longer lived due to their decreased precipitation efficiency. They also demonstrate an increased reflectivity and subsequently scatter an increased amount of solar radiation back to space. The net radiative effect is to cool the Earth's surface relative to the unmodified cloud. This indirect effect would be most likely observed to modify the climate system in regions of pristine ocean in which natural aerosol concentrations are small. The third pathway is through indirect effects on heterogeneous chemistry, which can alter the chemical composition of radiatively active gases.

1.2 Aerosol Remote Sensing

The large oceanic area of the planet combined with the dearth of direct measurements of aerosol have made global aerosol monitoring difficult. Satellite remote sensing offers the best method to obtain a global picture of atmospheric aerosols. Satellites offer a continuous data stream and near global coverage on relatively short time scales.

Numerous algorithms have been developed for the satellite remote sensing of atmospheric aerosols. The fundamental physical basis for existing satellite aerosol remote sensing retrievals is to quantify the aerosol burden based on the reflection of solar radiation to space. This approach has been applied from the ultraviolet (UV) through the near infrared (NIR) spectra, King et al. (1999). The primary remotely sensed aerosol parameter is the aerosol optical depth (AOD). Using a reflection based algorithm to remotely sense AOD requires some prior knowledge of the Earth-atmosphere system. First, it is required that molecular extinction properties as well as surface reflection can be properly modeled. Second, this method also requires the assumption of the scattering and absorption properties of the aerosol. The reflection due to aerosols may then be inferred as a residual in the total reflection of the system.

Several operational algorithms exist to infer AOD from measurements at a single viewing angle. In particular these methods have been applied to the Advanced Very High Resolution Radiometer (AVHRR), Ignatov and Stowe (2000) and the Moderate Resolution Imaging Spectroradiometer (MODIS), Kaufman and Tanre (1998) instruments. With the successful flights of the Multi-angle Imaging SpectroRadiometer (MISR) and Polarization and Directionality of the Earth's Reflectances (POLDER) I and II instruments, AOD retrievals based on a sampling of the aerosol scattering phase function have been implemented, Deuze et al. (2000), Kahn et al. (2005). Both MISR and POLDER make multi-spectral measurements of the same geophysical location from several viewing geometries. The multi-angular nature of these measurements allow for the reduction of errors associated with identification of an aerosol model and surface reflection. The POLDER instrument has the added benefit of polarization measurements in three of its nine channels. The addition of polarization information to multi angular radiance measurements has been shown to provide information about the more

fundamental quantities of an aerosol size distribution and refractive index, Chowdhary et al. (2004).

1.3 Scientific Objectives and Chapter Outline

The scientific objective of this thesis is to examine the utility of multi-angular and polarized radiances to the remote sensing of the spectral AOD in the visible and NIR. The specific channels considered are the two aerosol channels of the POLDER instrument. These channels have band centers at 670.2 and 860.8 nm. This work is a first step toward the development of a multi-sensor A-train aerosol retrieval. The Parasol satellite successfully joined the A-train in December of 2004 carrying the POLDER III instrument. The CALIPSO Lidar will join the A-train constellation imminently, providing additional size distribution and vertical distribution characteristics. In addition, the MODIS instrument provides multi-spectral information at longer wavelengths than POLDER. It is hoped that an integration of the available multi-sensor information will enable an improved characterization of atmospheric aerosols.

This thesis can be divided into two broad sections. The first section describes the two theoretical tools used in the research. The first is a theoretical framework for calculating the optical properties of atmospheric constituents. The second tool is a polarized radiative transfer model. The second broad section of the thesis is an application of these tools. A sensitivity study of the model to aerosol optical properties was performed. The results of this sensitivity study were then used in the development and analysis of an aerosol optical depth retrieval.

Chapter 2 outlines the theoretical basis for the calculation of optical properties used in the thesis. Of particular interest to this work were the absorption and scattering properties of aerosol particles as well as the molecular atmosphere. The absorption properties of the molecular

atmosphere in the visible and near infrared spectrum were calculated using the HITRAN database. The scattering properties of molecules were calculated using the Rayleigh approximation. Spherical aerosols were assumed and Mie theory was implemented in the calculation of their scattering properties. Both the Rayleigh and Mie scattering calculations were performed for the full polarized scattering phase matrix. These matrices were expanded in a series of generalized spherical functions.

Chapter 3 details the development of a fully polarized radiative transfer model for the propagation of solar radiation in the atmosphere. The motivation for the development of this model was to add a realistic reflecting surface to a multi-stream radiative transfer model. The model uses the approximate doubling solution method. The adding method is implemented to allow for an arbitrary number of homogenous atmospheric layers. Two surface boundary conditions are allowed. The first is a simple Lambertian reflecting surface. The second option is a realistic rough ocean reflecting surface. The model may be run with an arbitrary number of Stokes parameters. Therefore, it may be collapsed down to the case of scalar radiative transfer. Both Gaussian and Lobatto quadrature are permitted. The fundamental inputs to the model for each layer are the extinction and scattering coefficients along with the generalized spherical function expansion of the phase matrix.

Chapter 4 outlines the results of a sensitivity study into the feasibility of an aerosol optical depth retrieval over oceans. The sensitivity study includes an in depth analysis of the errors associated with forward model assumptions. Also, included in the study is an analysis of the scene dependent nature of the problem. Specifically, the effects of the solar and viewing geometries, as well as the optical depth of the aerosol layer are examined. The most important

result of the sensitivity analysis is the signal to noise ratio, which describes the quality of the information contained in a particular measurement.

The angular averaged value of signal for both the total and polarized radiance is seen to decrease with optical depth and increase with solar zenith angle. The angular average errors, on the other hand, are shown to increase with optical depth and with solar zenith angle. Consequently, the signal to noise ratio decreases strongly with optical depth and has a weak functional dependence on solar zenith angle. The angular structure of each of these quantities is also analyzed. It is demonstrated that the angles with the largest signal to noise ratios for both the total and polarized radiances are in the solar backscatter direction while those with the lowest signal to noise ratios tend to be in the glint direction. Finally, it is shown that the total radiance tends to have a signal to noise ratio about three times as large as the polarized radiance.

The sensitivity analysis is the precursor to the development of a two-channel aerosol optical depth retrieval utilizing multi-angular intensity measurements. Chapter 5 describes the optimal estimation framework, upon which the retrieval is based. The retrieval is subsequently analyzed for several cases using synthetic measurements. Two sources of bias are identified and discussed. First, an a priori bias is demonstrated which biases the retrieved answer towards the a priori estimate. A second source of bias is shown to result from the assumption of an aerosol model. A measurement viewing geometry dependence is demonstrated. It is shown that viewing geometries with high signal to noise ratios are less biased than those with low signal to noise ratio. It is expected that in an average sense these biases will tend to cancel due to the linear nature of the biases. Finally, a small set of data from the POLDER II instrument are applied to the retrieval algorithm and are shown to be in qualitative agreement with the POLDER operational product. The optimal estimation framework can easily be extended to include the

more fundamental parameters defining the aerosol model. An approach for pursuing these parameters within this retrieval framework is introduced.

Chapter 6 offers some concluding remarks as well as a look to the future. The key points of the thesis are outlined and some suggestions are made regarding the future of this research. The scene dependent error analysis of the aerosol retrieval problem quantifies the non-uniqueness of retrieved aerosol optical depths. The measurement errors are shown to be primarily a function of aerosol model assumptions. It is not uncommon for the scene dependent nature of measurement errors to be ignored in a retrieval algorithm. The aerosol optical depth optimal estimation retrieval which was developed allows for a unique examination and quantification of the effects of aerosol model assumptions on the retrieval problem.

This work has illustrated that a retrieval using multi-angular radiance measurements offers a method to improve the assumed aerosol model, a posteriori. This a posteriori model may then be used as the a priori model for a retrieval utilizing polarized radiances. Other measurements could also be added to this measurement vector. In considering a possible multi-sensor A-train aerosol retrieval, MODIS and CALIPSO may offer valuable information to help constrain the solution. The MODIS NIR measurements at wavelengths longer than 1 micron have been shown to be relatively insensitive to the small mode of the size distribution, Cairnes et al. (2005). This offers a constraint on the large mode of the size distribution with diminished noise from the small mode. CALIPSO measurements will offer further constraint as well as aerosol vertical profiles. It is further suggested that CALIPSO optical depth measurements could be used to determine the a priori aerosol model.

CHAPTER 2

ATMOSPHERIC ABSORPTION AND SCATTERING

2.1 Introduction

Of particular interest to the remote sensing of aerosols is the reflection of sunlight from the Earth-Atmosphere system. In order to use measurements of reflected sunlight to remotely sense aerosols, it is necessary to be able to model the physics of the extinction of sunlight in the atmosphere. There are two mechanisms for the extinction of sunlight; absorption and scattering. This chapter outlines the methods that will be used in this research to calculate both the absorption and scattering properties of atmospheric gases as well as aerosols.

2.2 Gaseous Absorption

There is relatively little molecular absorption in the visible and near infrared regions of the spectrum. Nonetheless, absorption by Oxygen and water vapor affect several of the POLDER channels. Absorption in this region was modeled using the HITRAN database which is a database of absorption line positions and strengths, Rothman (2004). Absorption line strengths are given at standard temperature and pressure. The strength of a line is a function of temperature. This temperature dependence is given by Liou (1992)

$$S(T) = S(T_o)\left(\frac{T_o}{T}\right)^m \frac{1-\exp(-hc\nu_o/KT)}{1-\exp(-hc\nu_o/KT_o)}\exp\left[-\frac{hcE_i}{K}\left(\frac{1}{T}-\frac{1}{T_o}\right)\right] \tag{2.1}$$

Absorption lines are not located at perfectly discrete positions. Instead there is broadening of absorption lines which leads to a smearing out of any given absorption line. The absorption coefficient at any given wave number is given by

$$\sigma_a = \sum_j S_j f_j(\nu - \nu_o) \tag{2.2}$$

where f is a probability distribution function known as the line shape, or line profile, and the summation is over all nearby absorption lines. The line shape represents the broadening of absorption lines due to various effects. Liou (1992) gives the following outline for the calculation of the line shape.

Below about 20 km the primary mechanism for line broadening is pressure broadening. This broadening is the result of collisions between molecules. For pressure broadened lines the line shape is given by the Lorentz profile

$$f_L(\nu - \nu_o) = \frac{\alpha_L}{\pi\left[(\nu-\nu_o) + {\alpha_L}^2\right]} \tag{2.3}$$

where

$$\alpha_L = \alpha_o\left(\frac{p}{p_o}\right)\left(\frac{T_o}{T}\right)^n$$

Above 50 km the primary mechanism for line broadening is Doppler broadening. At these elevations the density of air is low and the temperatures increase. Under these conditions the velocity of absorbing molecules becomes important in causing Doppler broadening of absorption lines. This line shape is described by the normally distributed Doppler profile

$$f_D(\nu - \nu_o) = \frac{1}{\alpha_D\sqrt{\pi}}\exp\left[-\frac{(\nu-\nu_o)^2}{{\alpha_D}^2}\right] \tag{2.4}$$

where

$$\alpha_D = \frac{\nu_o}{c}\sqrt{2RT}$$

Between roughly 20 and 50 km both Pressure and Doppler broadening play a significant role. Under these conditions the line shape is given by the convolution of the Lorentz and the Doppler profiles

$$f_\nu(\nu - \nu_o) = \int_{-\infty}^{\infty} f_L(\nu' - \nu_o) f_D(\nu - \nu')d\nu'$$

This is referred to as the Voight profile. A simplified, numerically efficient parameterization of the Voigt profile is given by Liou (1992)

$$\begin{aligned} f_V(\nu - \nu_o) = {} & \sqrt{\frac{\ln 2}{\pi}}\frac{1}{\alpha_V}(1-\xi)e^{-\eta^2 \ln 2} + \frac{1}{\pi\alpha_V}\xi\frac{1}{1+\eta^2} \\ & - \frac{1}{\pi\alpha_V}\xi(1-\xi)\left(\frac{1.5}{\ln 2} + 1 + \xi\right)\left(0.066e^{-0.4\eta^2} - \frac{1}{40 - 5.5\eta^2 + \eta^4}\right) \end{aligned} \tag{2.5}$$

where $\xi = \alpha_L/\alpha_V$, $\eta = (\nu - \nu_o)/\alpha_V$ and the Voigt half width is given by

$$\alpha_V = 0.5\left(\alpha_L + \sqrt{{\alpha_L}^2 + 4\alpha_D \ln 2}\right) + 0.5\alpha_L\left(1 - \frac{2\alpha_L}{\alpha_L + \sqrt{{\alpha_L}^2 + 4\alpha_D \ln 2}}\right) \tag{2.6}$$

All absorption calculations used in this work assume the Voight profile. This profile is valid for all layers of the atmosphere. In the lower atmosphere it tends towards the Lorentz profile while in the upper atmosphere it tends towards the Doppler profile.

2.3 Polarization

In order to fully describe the scattering of solar radiation in the atmosphere, it is necessary to consider the polarization state of the radiation. The polarization state describes the

preferred orientation and phase of the radiation. The parameters that define the polarization state will be introduced in the sections which follow.

2.3.1 The Stokes Vector

The fully polarized state of the radiance field can be described by the Stokes parameters. The Stokes parameters are defined in terms of the parallel and perpendicular electric field vectors, Van DeHulst (1981)

$$\begin{aligned} I &= E_l E_l^* + E_r E_r^* \\ Q &= E_l E_l^* - E_r E_r^* \\ U &= E_l E_r^* + E_r E_l^* \\ V &= i\left(E_l E_r^* - E_r E_l^*\right) \end{aligned} \tag{2.7}$$

The Stokes vector is defined from the Stokes parameters as $\tilde{I} = \left[I,Q,U,V\right]^T$. The first parameter represents the total radiant intensity. The remaining three parameters fully describe the polarization state of the radiation. The polarization state can range from fully polarized $Q^2 + U^2 + V^2 = I^2$ to unpolarized $Q^2 + U^2 + V^2 = 0$.

Incident solar radiation is made up of many randomly oriented incoherent waves and is thus unpolarized, or natural light. In general, the radiance field within Earth's atmosphere is polarized. The source of this polarization is scattering of sunlight within the Earth-Atmosphere system. In particular interest to this research, molecular Rayleigh scattering at solar wavelengths will create polarization while atmospheric aerosols tend to have a depolarizing effect.

2.3.2 The Scattering Matrix

The Stokes parameters are not scattered independently. Instead, they are coupled during a scattering event. In general, the scattering matrix for the Stokes vector follows then as

$$\begin{bmatrix} I \\ Q \\ U \\ V \end{bmatrix} = \begin{bmatrix} F_{11} & F_{12} & F_{13} & F_{14} \\ F_{21} & F_{22} & F_{23} & F_{24} \\ F_{31} & F_{32} & F_{33} & F_{34} \\ F_{41} & F_{42} & F_{43} & F_{44} \end{bmatrix} \begin{bmatrix} I \\ Q \\ U \\ V \end{bmatrix}' \tag{2.8}$$

where

$$F_{11} = \tfrac{1}{2}\left(|S_1|^2 + |S_2|^2 + |S_3|^2 + |S_4|^2\right)$$
$$F_{12} = \tfrac{1}{2}\left(|S_2|^2 - |S_1|^2 + |S_4|^2 - |S_3|^2\right)$$
$$F_{13} = \mathrm{Re}\left\{S_2 S_3^* + S_1 S_4^*\right\}$$
$$F_{14} = \mathrm{Im}\left\{S_2 S_3^* - S_1 S_4^*\right\}$$
$$F_{21} = \tfrac{1}{2}\left(|S_2|^2 - |S_1|^2 - |S_4|^2 + |S_3|^2\right)$$
$$F_{22} = \tfrac{1}{2}\left(|S_2|^2 + |S_1|^2 - |S_4|^2 - |S_3|^2 +\right)$$
$$F_{23} = \mathrm{Re}\left\{S_2 S_3^* - S_1 S_4^*\right\}$$
$$F_{24} = \mathrm{Im}\left\{S_2 S_3^* + S_1 S_4^*\right\}$$
$$F_{31} = \mathrm{Re}\left\{S_2 S_4^* + S_1 S_3^*\right\}$$
$$F_{32} = \mathrm{Re}\left\{S_2 S_4^* - S_1 S_3^*\right\}$$
$$F_{33} = \mathrm{Re}\left\{S_1 S_2^* + S_3 S_4^*\right\}$$
$$F_{34} = \mathrm{Im}\left\{S_2 S_1^* + S_4 S_3^*\right\}$$
$$F_{41} = \mathrm{Im}\left\{S_2 S_4^* + S_3 S_1^*\right\}$$
$$F_{42} = \mathrm{Im}\left\{S_2 S_4^* - S_3 S_1^*\right\}$$
$$F_{43} = \mathrm{Im}\left\{S_1 S_2^* - S_3 S_4^*\right\}$$
$$F_{44} = \mathrm{Re}\left\{S_1 S_2^* - S_3 S_4^*\right\}$$

Bohren and Huffman (1983). The primed vector represents the incoming radiation and the unprimed vector represents the scattered radiation in Equation 2.8.

The functions S_1, S_2, S_3, S_4 are the electric field amplitude scattering functions. They are complex valued functions which describe the scattering of the parallel and perpendicular electric fields. For a cloud of randomly oriented particles with a plane of symmetry, $S_3 = S_4 = 0$. The resulting scattering matrix will have off diagonal blocks of zeros. In contrast, the elements of the scattering matrix, F are real valued functions which describe the scattering of the real valued Stokes vector. For spherical particles $F_{11} = F_{22}$ and $F_{33} = F_{44}$. Spherical particles were used in this research. The assumption of sphericity immediately satisfies the further assumption of random orientation. Therefore, the scattering matrix used in this research is composed of only four independent parameters.

2.4 Atmospheric Scattering

The scattering of solar radiation in the atmosphere consists of two parts, molecular scattering and scattering by clouds and aerosols. Molecular scattering is scattering by atmospheric gases and to an extremely good approximation follows Rayleigh's Law. For the purposes of this study, scattering by aerosols is assumed to follow Mie theory, which assumes spherical aerosol particles. The methods for calculating the polarized scattering properties for these two distinct types of scattering are outlined below.

2.4.1 Rayleigh Scattering

Rayleigh scattering is an approximate solution to the electromagnetic scattering problem. It is valid when the size parameter

$$\chi = \frac{2\pi r}{\lambda} \tag{2.9}$$

is much less than unity. This approximation is valid in the visible and near infrared wavelengths for molecular scattering. The scattering matrix for Rayleigh scattering is given by Van DeHulst (1981)

$$F = \begin{bmatrix} \frac{3}{4}\left(1+\cos^2\Theta\right) & \frac{3}{4}\left(\cos^2\Theta-1\right) & 0 & 0 \\ \frac{3}{4}\left(\cos^2\Theta-1\right) & \frac{3}{4}\left(1+\cos^2\Theta\right) & 0 & 0 \\ 0 & 0 & \cos\Theta & 0 \\ 0 & 0 & 0 & \cos\Theta \end{bmatrix} \tag{2.10}$$

Stephens (1994) suggests the following parameterization for the Rayleigh scattering optical depth

$$\tau = 0.0088\lambda^{0.2\lambda-4.15}e^{-0.00116z^2-0.1188z} \tag{2.11}$$

Note that the optical depth has both a wavelength dependence as well as height dependence. This parameterization describes the optical depth for a cloud free, standard molecular atmosphere.

2.4.2 Mie Scattering

Mie theory is a rigorous solution to the scattering of radiation by spherical particles. It follows from a direct yet tedious application of Maxwell's equations. The electric field amplitude scattering functions for Mie theory are given by Bohren and Huffman (1983)

$$\begin{aligned} S_1(\Theta) &= \sum_{n=1}^{\infty} \frac{2n+1}{n(n+1)} \left\{ a_n \pi_n(\Theta) + b_n \tau_n(\Theta) \right\} \\ S_2(\Theta) &= \sum_{n=1}^{\infty} \frac{2n+1}{n(n+1)} \left\{ b_n \pi_n(\Theta) + a_n \tau_n(\Theta) \right\} \end{aligned} \tag{2.12}$$

The functions π_n and τ_n are related to the Legendre polynomials and contain the angular scattering information. The functions a_n and b_n are complex valued functions of the index of refraction and the size parameter. The functions given by Equation 2.12 were evaluated using the Bohren and Huffman (1983) Mie scattering routine. Evaluating Equations 2.12 for the Mie amplitude scattering functions results in a scattering matrix of the form

$$F(\Theta) = \begin{bmatrix} F_{11} & F_{12} & 0 & 0 \\ F_{21} & F_{11} & 0 & 0 \\ 0 & 0 & F_{33} & F_{34} \\ 0 & 0 & -F_{34} & F_{33} \end{bmatrix} \tag{2.13}$$

The resulting extinction and scattering efficiency factors are given by

$$\begin{aligned} Q_{ext} &= \frac{2}{\chi^2} \mathrm{Re} \left\{ \sum_{n=1}^{\infty} (2n+1)(a_n + b_n) \right\} \\ Q_{sca} &= \frac{2}{\chi^2} \sum_{n=1}^{\infty} (2n+1) \left\{ |a_n|^2 + |b_n|^2 \right\} \end{aligned} \tag{2.14}$$

The efficiency factors are the ratio of the effective scattering and extinction cross sections to the cross section of the actual particle and are therefore unitless. The effective scattering and extinction cross sections, with units of area, then follow in a straight forward manner as

$$C_{ext} = \pi r^2 Q_{ext}$$
$$C_{sca} = \pi r^2 Q_{sca} \tag{2.15}$$

In realistic atmospheric clouds, the number concentration of droplets or particles follow some size distribution, $n(r)$. For this research a bimodal log normal size distribution is assumed. The form of this size distribution is described in Equation 4.2. The extinction and scattering coefficients, with units of inverse distance, are found by integrating the cross sections over the size distribution

$$\beta_{ext} = \int_{r_{\min}}^{r_{\max}} C_{ext} n(r) dr$$
$$\beta_{sca} = \int_{r_{\min}}^{r_{\max}} C_{sca} n(r) dr \tag{2.16}$$

This integration is performed using the trapezoidal integration rule. Similar to the scattering and extinction coefficients, the scattering matrix elements for a cloud of particles are found by integrating over the size distribution. Imposing the phase function normalization condition results in an additional normalization factor. Hansen and Travis (1974) give the resulting formula for the scattering matrix of a cloud of particles

$$P(\Theta) = \frac{\lambda^2}{\pi \beta_{sca}} \int_{r_{\min}}^{r_{\max}} F(\Theta) n(r) dr \tag{2.17}$$

The quantities given by equations 2.16 and 2.17 are fundamental inputs to the radiative transfer model described in the following chapter.

Evaluating the scattering matrix at many angles can become cumbersome due to the recurrence formulas that must be used. Because of this it is convenient to expand the scattering matrix in a basis of generalized spherical functions.

$$P(\Theta) = \sum_{l=\max(|m|,|n|)}^{\infty} \chi_{m,n}^{l} \Psi_{m,n}^{l}(\Theta) \tag{2.18}$$

The expansion is performed using the procedure outlined in de Rooij and Van der Stapp (1984). Using the orthogonality properties of the generalized spherical functions allows the expansion coefficient matrix to be found as

$$\chi_{m,n}^{l} = \frac{2l+1}{2} \int_{-1}^{1} \Psi_{m,n}^{l}(\Theta) P(\Theta) d\mu \tag{2.19}$$

This integration is performed numerically using Gaussian quadrature. Inputting the expansion coefficients of the scattering matrix as opposed to calculating the full scattering matrix at many angles in the radiative transfer model, described in the following chapter, results in a significant computational savings when the size parameter becomes large and when the physics of the problem require that a large number of angles be used in the calculation.

2.5 Definitions

As described by the equations given in 2.16, the extinction and scattering coefficients have units of inverse distance. Similarly, for molecular absorption, an absorption coefficient with units of inverse distance may be calculated given a density profile. The total extinction may then be calculated as the sum of the scattering and the absorption

$$\beta_{ext} = \beta_{sca} + \beta_{abs} \tag{2.20}$$

The single scatter albedo is the ratio of the scattering to the total extinction

$$\omega_o = \beta_{sca} / \beta_{ext} \tag{2.21}$$

Given the extinction coefficient, the unitless optical depth is defined

$$\tau = -\int \beta_{ext} dz \tag{2.22}$$

where z is measured normal to the Earth's surface and τ increases downward. An optical path length, which is measured in any direction follows as (τ/μ) where $\mu = \cos\theta$ and θ is measured relative to the normal.

CHAPTER 3

RADIATIVE TRANSFER MODEL

3.1 Introduction

The radiative transfer model developed for this research solves the vector, monochromatic, plane parallel equation of transfer with an incident solar source. The solution method used is the doubling method for an arbitrary number of streams. A multi-stream solution is necessary to adequately sample the scattering phase function and thus accurately resolve the radiance field. Full angular resolution of the radiance field is critical to model multi-angular measurements such as those of the POLDER instrument. The model can be solved for a Stokes vector of arbitrary length. For a Stokes vector of length one, the problem collapses down to the scalar radiative transfer problem. The adding method is used to allow for the solution of an atmosphere with an arbitrary number of layers. Two surface boundary conditions are currently allowed. The first is a Lambertian surface, which reflects an equal intensity in all directions. The second is a semi-empirically derived, reflecting rough ocean surface, which is a function of wind speed. This chapter outlines the solution method used to develop the radiative transfer model.

3.2 Fundamentals

3.2.1 The Phase Matrix

As discussed in Section 2.4.3, the scattering matrix is expanded in a series of generalized spherical functions. The number of terms in the expansion necessary to accurately reproduce the scattering matrix has been given by Wiscombe (1980) as

$$N_t \approx \chi + 4\chi^{1/3} + 2 \tag{3.1}$$

for size parameters greater than eight. For the Rayleigh phase matrix $N_t = 3$. Equation 2.13 gives the form of the Mie scattering matrix, which is composed of four independent parameters. Recall that for spherical particles $F_{22} = F_{11}$ and $F_{33} = F_{44}$. More generally, the scattering matrix for any randomly oriented particles with a plane of symmetry is given by six independent parameters, Van DeHulst (1981). The general form of the matrix will be used in the following development.

The scattering matrix describes a single scattering event within the scattering plane. Unlike the total intensity, however, the polarization state of the radiation field is dependent on the reference frame. This introduces the necessity of rotations of the Stokes vector from one reference frame to another. Therefore, the rotation matrix L must be introduced to describe a rotation through an arbitrary angle i, Liou (2002)

$$L(i) = \begin{bmatrix} 1 & 0 & 0 & 0 \\ 0 & \cos 2i & \sin 2i & 0 \\ 0 & -\sin 2i & \cos 2i & 0 \\ 0 & 0 & 0 & 1 \end{bmatrix} \tag{3.2}$$

In order to describe any arbitrary scattering event from one reference frame into another, two rotations are necessary. First, the incident Stokes vector must be rotated into the scattering

plane. Now the scattering matrix may be applied to describe the scattering event within the scattering plane. Finally, the scattered stokes vector must be rotated into the solar reference plane to perform the radiative transfer calculations. Mathematically these rotations define a new rotated scattering matrix called the phase matrix

$$\tilde{P}(\Theta) = L(\pi - i_2)P(\Theta)L(-i_1) \tag{3.3}$$

The explicit form of this matrix follows as

$$\tilde{P}(\theta) = \begin{bmatrix} P_{11} & P_{12}\cos(2i_1) & -P_{12}\sin(2i_1) & 0 \\ P_{21}\cos(2i_2) & \begin{pmatrix} P_{22}\cos(2i_1)\cos(2i_2) \\ -P_{33}\sin(2i_1)\sin(2i_2) \end{pmatrix} & \begin{pmatrix} -P_{22}\sin(2i_1)\cos(2i_2) \\ -P_{33}\cos(2i_1)\sin(2i_2) \end{pmatrix} & -P_{34}\sin(2i_2) \\ -P_{21}\sin(2i_2) & \begin{pmatrix} P_{22}\cos(2i_1)\sin(2i_2) \\ +P_{33}\sin(2i_1)\cos(2i_2) \end{pmatrix} & \begin{pmatrix} -P_{22}\sin(2i_1)\sin(2i_2) \\ P_{33}\cos(2i_1)\cos(2i_2) \end{pmatrix} & P_{34}\cos(2i_2) \\ 0 & P_{43}\sin(2i_1) & P_{43}\cos(2i_1) & P_{44} \end{bmatrix} \tag{3.4}$$

Note that in the scalar radiative transfer problem these rotations are unnecessary as the phase matrix collapses to the P_{11} element, which is the phase function.

3.2.2 The Vector Radiative Transfer Equation

Following Liou (2002), the plane-parallel, steady state radiative transfer equation for the scattering of solar radiation is given by

$$\mu\frac{d\tilde{I}(\tau,\mu,\phi)}{d\tau} = \tilde{I}(\tau,\mu,\phi) - \frac{\omega_o}{4\pi}\int_0^{2\pi}\int_{-1}^{1}\tilde{P}(\tau,\mu,\phi,\mu',\phi')\tilde{I}(\tau,\mu',\phi')d\mu' d\phi' - \frac{\omega_o}{4\pi}\tilde{P}(\tau,\mu,\phi,\mu_o,\phi_o)F_o e^{-\tau/\mu_o} \tag{3.5}$$

where,

$\tilde{I}$ is the Stokes vector

$\tilde{P}$ is the phase matrix

τ is the optical depth defined increasing downward

μ is the cosine of the zenith angle defined positive upward

μ_o is the cosine of the solar zenith angle

ϕ is the azimuth angle

ω_o is the single scatter albedo

F_o is a vector of length four in which the first element is the incident solar flux in the μ_o direction and the other elements are zero

3.3 Discretization of the Radiative Transfer Equation

3.3.1 Fourier Series in Azimuth

The integrals over angle in Equation 3.5 make the search for analytical solutions difficult. It is, therefore, common to discretize the integrals in order to find numerical solutions. The azimuthal dependence in the Stokes vector is expanded in a Fourier series as

$$\tilde{I}(\tau,\mu,\phi) = \sum_{m=0}^{M} \tilde{I}_c^m(\tau,\mu)\cos(m\phi) + \tilde{I}_s^m \sin(m\phi) \tag{3.6}$$

where the Fourier coefficients are given by

$$\begin{aligned} \tilde{I}_c^m &= \frac{1}{(1+\delta_{m,0})\pi}\int_0^{2\pi} \tilde{I}\cos(m\phi)d\phi \\ \tilde{I}_s^m &= \frac{1}{\pi}\int_0^{2\pi} \tilde{I}\sin(m\phi)d\phi \end{aligned} \tag{3.7}$$

Similarly, the phase matrix is expanded in a Fourier series

$$\tilde{P}(\tau,\mu,\phi) = \sum_{m=0}^{M} \tilde{P}_c^m(\tau,\mu)\cos[m(\phi-\phi_o)] + \tilde{P}_s^m \sin[m(\phi-\phi_o)] \tag{3.8}$$

where $\phi_o = \pi$ by definition. The following Fourier integral transforms are applied to every term in equation 3.5 for the sine and cosine modes separately

$$\frac{1}{(1+\delta_{m,0})\pi}\int_0^{2\pi}[.....]\cos(m\phi)d\phi$$
$$\frac{1}{\pi}\int_0^{2\pi}[.....]\sin(m\phi)d\phi \tag{3.9}$$

Then the right hand side of equation 3.8 is substituted into 3.5 for the phase matrix. Utilizing the angle subtraction identities

$$\cos(x-y)=\cos x\cos y+\sin x\sin y$$
$$\sin(x-y)=\sin x\cos y-\cos x\sin y \tag{3.10}$$

as well as the trigonometric integral identities

$$\int_0^{2\pi}\cos(mx)\cos(nx)dx=[(1+\delta_{0,m})\delta_{m,n}]\pi$$
$$\int_0^{2\pi}\sin(mx)\sin(nx)dx=\delta_{m,n}(1-\delta_{0,m})\pi \tag{3.11}$$
$$\int_0^{2\pi}\cos(mx)\sin(mx)dx=0$$

two coupled transfer equations are found for the Fourier coefficients.

$$\mu\frac{d\tilde{I}_c^m}{d\tau}=\tilde{I}_c^m-\frac{\omega_o}{4}\int_{-1}^{1}[(1+\delta_{0,m})\tilde{P}_c^m\tilde{I}_c^m-(1-\delta_{0,m})\tilde{P}_s^m\tilde{I}_s^m]d\mu'-\frac{\omega_o}{4\pi}\tilde{P}_c^m F_o e^{-\tau/\mu_o}$$
$$\mu\frac{d\tilde{I}_s^m}{d\tau}=\tilde{I}_s^m-\frac{\omega_o}{4}\int_{-1}^{1}[(1-\delta_{0,m})\tilde{P}_c^m\tilde{I}_s^m-(1+\delta_{0,m})\tilde{P}_s^m\tilde{I}_c^m]d\mu'+(1-\delta_{0,m})\frac{\omega_o}{4\pi}\tilde{P}_s^m F_o e^{-\tau/\mu_o} \tag{3.12}$$

The equations given by 3.12 no longer have any azimuthal dependence. Once they are solved for the Fourier coefficients of a number of modes, the azimuthal dependence is reintroduced by summing the Fourier series to find the Stokes parameters at any given azimuth angle.

In the scalar case the addition theorem of spherical harmonics is used to find the Fourier cosine coefficients of the phase function. The reference frame rotations required for vector radiative transfer prohibit this technique. The method used here is that of Evans and Stephens

(1991). The phase matrix is sampled at a number of evenly spaced azimuth angles and Fourier transformed using an FFT routine.

3.3.2 Decoupling of the Cosine and Sine Modes

In Equation 3.4 it can be seen that the diagonal blocks of the phase matrix are even function of ϕ - ϕ_o, while the off diagonal blocks are odd functions in ϕ - ϕ_o. As a result, the cosine coefficients of the off diagonal blocks are zero as are the sine coefficients of the diagonal blocks. Subsequently, for each azimuth mode the two equations given in 3.12 can be combined into a single equation for both the cosine and sine coefficients. Doing so introduces a new 8x8 phase matrix of the form

$$\begin{bmatrix} \begin{pmatrix} I_c^m \\ Q_c^m \\ U_c^m \\ V_c^m \end{pmatrix} \\ \begin{pmatrix} I_s^m \\ Q_s^m \\ U_s^m \\ V_s^m \end{pmatrix} \end{bmatrix} = \begin{bmatrix} (1+\delta_{0,m}) \begin{pmatrix} \tilde{P}_{c,11}^m & \tilde{P}_{c,12}^m & 0 & 0 \\ \tilde{P}_{c,21}^m & \tilde{P}_{c,22}^m & 0 & 0 \\ 0 & 0 & \tilde{P}_{c,33}^m & \tilde{P}_{c,34}^m \\ 0 & 0 & \tilde{P}_{c,43}^m & \tilde{P}_{c,44}^m \end{pmatrix} & -(1-\delta_{0,m}) \begin{pmatrix} 0 & 0 & \tilde{P}_{s,13}^m & \tilde{P}_{s,14}^m \\ 0 & 0 & \tilde{P}_{s,23}^m & \tilde{P}_{s,24}^m \\ \tilde{P}_{s,31}^m & \tilde{P}_{s,32}^m & 0 & 0 \\ \tilde{P}_{s,41}^m & \tilde{P}_{s,42}^m & 0 & 0 \end{pmatrix} \\ (1-\delta_{0,m}) \begin{pmatrix} 0 & 0 & \tilde{P}_{s,13}^m & \tilde{P}_{s,14}^m \\ 0 & 0 & \tilde{P}_{s,23}^m & \tilde{P}_{s,24}^m \\ \tilde{P}_{s,31}^m & \tilde{P}_{s,32}^m & 0 & 0 \\ \tilde{P}_{s,41}^m & \tilde{P}_{s,42}^m & 0 & 0 \end{pmatrix} & (1-\delta_{0,m}) \begin{pmatrix} \tilde{P}_{c,11}^m & \tilde{P}_{c,12}^m & 0 & 0 \\ \tilde{P}_{c,21}^m & \tilde{P}_{c,22}^m & 0 & 0 \\ 0 & 0 & \tilde{P}_{c,33}^m & \tilde{P}_{c,34}^m \\ 0 & 0 & \tilde{P}_{c,43}^m & \tilde{P}_{c,44}^m \end{pmatrix} \end{bmatrix} \begin{bmatrix} \begin{pmatrix} I_c^m \\ Q_c^m \\ U_c^m \\ V_c^m \end{pmatrix} \\ \begin{pmatrix} I_s^m \\ Q_s^m \\ U_s^m \\ V_s^m \end{pmatrix} \end{bmatrix}' \tag{3.13}$$

It can clearly be seen that the scattering of the mixed stokes vectors,

$$\begin{aligned} \hat{I}^m &= \left[I_c^m, Q_c^m, U_s^m, V_s^m \right]^T \\ \hat{I}^m &= \left[I_s^m, Q_s^m, U_c^m, V_c^m \right]^T \end{aligned} \tag{3.14}$$

decouple in the Fourier basis. Because the incident solar source is an even function in ϕ - ϕ_o and is unpolarized, the second vector in 3.14 is initially zero. Because the scattering of the two vectors is uncoupled the second will remain zero and does not need to be considered in the

solution of the radiative transfer equation. This leaves only the first mixed Stokes vector to be solved for. The mixed phase matrix for this new vector has the form

$$\hat{P}^m = \begin{bmatrix} (1+\delta_{0,m})\begin{pmatrix} \tilde{P}^m_{c,11} & \tilde{P}^m_{c,12} \\ \tilde{P}^m_{c,21} & \tilde{P}^m_{c,22} \end{pmatrix} & -(1-\delta_{0,m})\begin{pmatrix} \tilde{P}^m_{s,13} & \tilde{P}^m_{s,14} \\ \tilde{P}^m_{s,23} & \tilde{P}^m_{s,24} \end{pmatrix} \\ (1-\delta_{0,m})\begin{pmatrix} \tilde{P}^m_{s,31} & \tilde{P}^m_{s,32} \\ \tilde{P}^m_{s,41} & \tilde{P}^m_{s,42} \end{pmatrix} & (1-\delta_{0,m})\begin{pmatrix} \tilde{P}^m_{c,33} & \tilde{P}^m_{c,34} \\ \tilde{P}^m_{c,43} & \tilde{P}^m_{c,44} \end{pmatrix} \end{bmatrix} \tag{3.15}$$

Utilizing the above symmetries, the equations given by 3.12 can now be rewritten as a single equation for a mixed Stokes vector

$$\mu \frac{d\hat{I}^m(\tau,\mu)}{d\tau} = \hat{I}^m(\tau,\mu) - \frac{\omega_o}{4}\int_{-1}^{1} \hat{P}^m(\tau,\mu,\mu')\hat{I}^m(\tau,\mu')d\mu' - \frac{\omega_o}{4\pi}\hat{P}^m(\tau,\mu,\mu_o)F_o e^{-\tau/\mu_o} \tag{3.16}$$

3.3.3 Numerical Quadrature in Zenith Angle

Equation 3.16 still contains a complicated angular integral over the product of the phase matrix and the Stokes vector. Traditionally, this integral is discretized using a numerical quadrature scheme of the form

$$\int_{-1}^{1} f(\mu)d\mu = \sum_{\substack{j=-n \\ j\neq 0}}^{n} w_j f(\mu_j) \tag{3.17}$$

where w_j is a weighting factor associated with the $2n$ discrete abscissa. The sum of the quadrature weights, for the above integration, is equal to two.

For Gaussian quadrature the integration is exact if the integrand is a polynomial of degree $N_t \leq 2n-1$. The corresponding rule for Lobatto quadrature is $N_t \leq 2n-3$. Following these rules, the expansion of the phase matrix in generalized spherical functions is performed to a maximum of N_t terms.

Introducing quadrature into the radiative transfer equation results in the following equation for the Stokes vector at $2n$ discrete quadrature points

$$\mu_i \frac{d\hat{I}^m(\tau,\mu_i)}{d\tau} = \hat{I}^m(\tau,\mu_i) - \frac{\omega_o}{4}\sum_{\substack{j=-n \\ j\neq 0}}^{j=n} w_j \hat{P}^m(\tau,\mu_i,\mu_j)\hat{I}(\tau,\mu_j) - \frac{\omega_o}{4\pi}\hat{P}^m(\tau,\mu_i,-\mu_o)F_o e^{-\tau/\mu_o} \quad (3.18)$$

The quadrature weights and abscissa are formulated in such a way that the abscissa in the upper hemisphere are opposite those in the lower hemisphere with equal weighting. Therefore, it is logical to break 3.17 into upward and downward components explicitly

$$\pm\mu_i \frac{d}{d\tau}\begin{bmatrix}\hat{I}^{m+}\\ \hat{I}^{m-}\end{bmatrix} = \begin{bmatrix}\hat{I}^{m+}\\ \hat{I}^{m-}\end{bmatrix} - \frac{\omega_o}{4}\sum_{j=1}^{n} w_j \begin{bmatrix}\hat{P}^m(\mu_i,\mu_j) & \hat{P}^m(\mu_i,\mu_j)\\ \hat{P}^m(-\mu_i,\mu_j) & \hat{P}^m(-\mu_i,-\mu_j\end{bmatrix}\begin{bmatrix}\hat{I}^{m+}\\ \hat{I}^{m-}\end{bmatrix} - \frac{\omega_o}{4\pi}\begin{bmatrix}\hat{P}^m(\mu_i,-\mu_o)\\ \hat{P}^m(-\mu_i,-\mu_o)\end{bmatrix}\begin{bmatrix}F_o\\ F_o\end{bmatrix}e^{-\tau/\mu_o} \quad (3.19)$$

3.4 The Matrix Equation of Transfer

Equation 3.19 represents $2n$ coupled equations for each azimuth mode. This may be written in a matricial form as follows

$$\frac{d}{d\tau}\begin{bmatrix}I^{m+}\\ I^{m-}\end{bmatrix} = \begin{bmatrix}M^{-1} & 0\\ 0 & M^{-1}\end{bmatrix}\begin{bmatrix}I^{m+}\\ I^{m-}\end{bmatrix} - \left(\frac{\omega_o}{4}\right)\begin{bmatrix}M^{-1} & 0\\ 0 & M^{-1}\end{bmatrix}\begin{bmatrix}P^m(\mu_i,\mu_j) & P^m(\mu_i,-\mu_j)\\ P^m(-\mu_i,\mu_j) & P^m(-\mu_i,-\mu_j)\end{bmatrix}\begin{bmatrix}W & 0\\ 0 & W\end{bmatrix}\begin{bmatrix}I^{m+}\\ I^{m-}\end{bmatrix} - \left(\frac{\omega_o}{4\pi}\right)\begin{bmatrix}M^{-1} & 0\\ 0 & M^{-1}\end{bmatrix}\begin{bmatrix}P^m(\mu_i,-\mu_o)\\ P^m(-\mu_i,-\mu_o)\end{bmatrix}F_o e^{-\tau/\mu_o} \quad (3.20)$$

where M^{-1} and W are diagonal $4n$ by $4n$ matrices with the first four diagonal elements corresponding to $i = 1$ and so on to $i = n$. P^m is also a $4n$ by $4n$ matrix composed of the $\hat{P}^m$ sub-matrices. Equation (3.20) can be further compacted as

$$\frac{d}{d\tau}\begin{bmatrix}I^{m+}\\ I^{m-}\end{bmatrix} = \begin{bmatrix}\alpha_1 & \beta_1\\ \beta_2 & \alpha_2\end{bmatrix}\begin{bmatrix}I^{m+}\\ I^{m-}\end{bmatrix} + \begin{bmatrix}\Sigma^{+}\\ \Sigma^{-}\end{bmatrix} \quad (3.21)$$

where

$$\alpha_1 = M^{-1} - \left(\frac{\omega_o}{4}\right) M^{-1} P^m(\mu_i, \mu_j) W$$

$$\beta_1 = -\left(\frac{\omega_o}{4}\right) M^{-1} P^m(-\mu_i, -\mu_j) W$$

$$\beta_2 = \left(\frac{\omega_o}{4}\right) M^{-1} P^m(-\mu_i, -\mu_j) W$$

$$\alpha_2 = -M^{-1} - \left(\frac{\omega_o}{4}\right) M^{-1} P^m(-\mu_i, -\mu_j) W$$

$$\Sigma^+ = \left(\frac{\omega_o}{4\pi}\right) M^{-1} P^m(\mu_i, -\mu_o) F_o e^{-\tau/\mu_o}$$

$$\Sigma^- = \left(\frac{\omega_o}{4\pi}\right) M^{-1} P^m(-\mu_i, -\mu_o) F_o e^{-\tau/\mu_o}$$

In its most compact matricial form the radiative transfer equation is

$$\frac{dI}{d\tau} = AI + \Sigma \tag{3.22}$$

where

$$I = \begin{bmatrix} I^{m+} \\ I^{m-} \end{bmatrix}$$

$$A = \begin{bmatrix} \alpha_1 & \beta_1 \\ \alpha_2 & \beta_2 \end{bmatrix}$$

$$\Sigma = \begin{bmatrix} \Sigma^+ \\ \Sigma^- \end{bmatrix}$$

This is a matricial first order ordinary differential equation to be solved for the Stokes vector as a function of the optical depth.

3.5 Integration of the Radiative Transfer Equation

3.5.1 The Interaction Principle

The interaction principle is a simple physical principle, which relates the exitant radiances at the layer boundaries with the incoming radiances at the boundaries plus any source of radiation within the layer. It can be stated mathematically as

$$\begin{aligned} I^+(t) &= T^+ I^+(b) + R^+ I^-(t) + \Sigma^+ \\ I^-(b) &= T^- I^-(t) + R^- I^+(b) + \Sigma^- \end{aligned} \tag{3.23}$$

Where T, R and Σ are the global transmission, reflection and source functions of the layer. In general, these functions may have a complicated angular dependence. Here, t represents the top of the layer and b represents the layer bottom.

3.5.2 The Finite Difference Method

Equation (3.22) is a first order ordinary differential equation. A myriad of solution methods have been developed to solve this equation. The method used here is a simple physically based finite difference scheme. Equation (3.22) is rewritten as

$$\frac{I(\tau+\Delta\tau) - I(\tau)}{\Delta\tau} = AI(\Delta\tau/2) + \Sigma(\Delta\tau/2) \tag{3.24}$$

Separating the upward and downward radiances into two equations and rearranging terms gives

$$\begin{aligned} I^+(\tau) &= I^+(\tau+\Delta\tau) - \Delta\tau\left(\alpha_1 I^+(\Delta\tau/2) + \beta_1 I^+(\Delta\tau/2) + \Sigma^+(\Delta\tau/2)\right) \\ I^-(\tau+\Delta\tau) &= I^-(\tau) + \Delta\tau\left(\beta_2 I^+(\Delta\tau/2) + \alpha_2 I^+(\Delta\tau/2) + \Sigma^-(\Delta\tau/2)\right) \end{aligned} \tag{3.25}$$

If the approximation $I(\tau+\Delta\tau) \approx I(\Delta\tau/2) \approx I(\tau)$ is used then 3.25 can be rewritten in the form of the interaction principle

$$\begin{aligned} I^+(\tau) &= -\left(E - \Delta\tau\alpha_1\right) I^+(\tau+\Delta\tau) - \Delta\tau\beta_1 I^-(\tau) - \Sigma^+(\Delta\tau/2) \\ I^-(\tau+\Delta\tau) &= \Delta\tau\beta_2 I^+(\tau+\Delta\tau) + \left(E - \Delta\tau\alpha_2\right) I^-(\tau) + \Sigma^-(\Delta\tau/2) \end{aligned} \tag{3.26}$$

The global transmission and reflection matrices follow from the approximate form of the radiative transfer equation given by 3.26

$$\begin{aligned} T^{+} &= E - \Delta\tau\alpha_1 \\ T^{-} &= E + \Delta\tau\alpha_2 \\ R^{+} &= -\Delta\tau\beta_1 \\ R^{-} &= \Delta\tau\beta_2 \end{aligned} \tag{3.27}$$

The exitant radiance field may now be found by using the global reflection and transmission functions given by 3.27 in the interaction principle, 3.23. This approximate solution method can be made as accurate as desired by making $\Delta\tau$ as small as needed. It is exact for an infinitesimally thin layer.

3.5.3 Adding Equations

The interaction principle as stated in Section 3.5.1 applies to a single layer. In general the atmosphere may consist of any number of layers with differing optical properties. The approach in this section will be to generalize the concept of the interaction principle to a multi-layer medium. The multi-layer interaction principle will be used to derive the formulas needed to combine the optical properties of adjacent layers into a single layer. This process is relatively straight forward and consists of solving a linear system of equations.

The interaction principle for two adjacent layers is given by

$$\begin{aligned} I^{+}(t) &= T_1^{+} I^{+}(m) + R_1^{+} I^{-}(t) + \Sigma_1^{+} \\ I^{-}(m) &= R_1^{-} I^{+}(m) + T_1^{-} I^{-}(t) + \Sigma_1^{-} \\ I^{+}(m) &= T_2^{+} I^{+}(b) + R_2^{+} I^{-}(m) + \Sigma_2^{+} \\ I^{-}(b) &= R_2^{-} I^{+}(b) + T_2^{-} I^{-}(m) + \Sigma_2^{-} \end{aligned} \tag{3.28}$$

Here, m represents the middle level and layer 1 lies on top of layer 2. Solving for the internal radiances in terms of the incoming radiances at the top and bottom boundary by using the middle two equations in 3.28 gives

$$\begin{aligned} I^+(m) &= \left(E - R_2^+ R_1^-\right)^{-1}\left(T_2^+ I^+(b) + R_2^+ T_1^- I^-(t) + R_2^+ \Sigma_1^- + \Sigma_2^+\right) \\ I^-(m) &= \left(E - R_1^- R_2^+\right)^{-1}\left(R_1^- T_2^+ I^+(b) + T_1^- I^-(t) + R_1^- \Sigma_2^+ + \Sigma_1^-\right) \end{aligned} \tag{3.29}$$

Equations 3.29 can be used to solve for the internal radiance field between two atmospheric layers. Plugging the equations given by 3.29 back into the first and last equations of 3.28 results in

$$\begin{aligned} I^+(t) &= T_1^+ \Gamma^+ T_2^+ I^+(b) + T_1^+ \Gamma^+ R_2^+ T_1^- I^-(t) + R_1^+ I^-(t) + T_1^+ \Gamma^+ R_2^+ \Sigma_1^- + T_1^+ \Gamma^+ \Sigma_2^+ + \Sigma_1^+ \\ I^-(b) &= T_2^- \Gamma^- T_1^- I^-(t) + T_2^- \Gamma^- R_1^- T_2^+ I^+(b) + R_2^- I^+(b) + T_2^- \Gamma^- R_1^- \Sigma_2^+ + T_2^- \Gamma^- \Sigma_1^- + \Sigma_2^- \end{aligned} \tag{3.30}$$

where

$$\begin{aligned} \Gamma^+ &= \left(E - R_2^+ R_1^-\right)^{-1} \\ \Gamma^- &= \left(E - R_1^- R_2^+\right)^{-1} \end{aligned}$$

are known as the propagator terms. Physically the propagator terms represent an infinite number of multiple reflections at the layer interface. The equations given by 3.30 do not involve the internal radiances. They describe the exitant radiances from the two-layer medium in terms of the incident radiances and the internal sources. This is of the same form as the interaction principle for a single layer. Global transmission, reflection and source functions for the two-layer system follow as

$$
\begin{aligned}
T^{+} &= T_1^{+}\Gamma^{+}T_2^{+} \\
T^{-} &= T_2^{-}\Gamma^{-}T_1^{-} \\
R^{+} &= T_1^{+}\Gamma^{+}R_2^{+}T_1^{-} + R_1^{+} \\
R^{-} &= T_2^{-}\Gamma^{-}R_1^{-}T_2^{+} + R_2^{-} \\
\Sigma^{+} &= T_1^{+}\Gamma^{+}\left(R_2^{+}\Sigma_1^{-} + \Sigma_2^{+}\right) + \Sigma_1^{+} \\
\Sigma^{-} &= T_2^{-}\Gamma^{-}\left(R_1^{-}\Sigma_2^{+} + \Sigma_1^{-}\right) + \Sigma_2^{-}
\end{aligned}
\tag{3.31}
$$

In practice the global transmission, reflection and source functions of each homogenous atmospheric layer are found. Layers are then added one at a time forming combined layers, until the entire atmosphere has been added forming a super layer describing the reflection and transmission of the entire Earth-Atmosphere system. This super layer may then be used to find the exitant radiances at the top and bottom of the atmosphere. Equations 3.19 may be used to solve for the internal radiances at any layer interface.

3.5.4 Doubling Equations

The doubling equations are a simple extension of the adding equations. They are used in order to add homogenous layers in a much more efficient manner than simple adding allows. The idea is to begin with an infinitesimal layer of optical depth $\Delta\tau$, generated by the finite differencing equations. This layer is then doubled by using the adding equations creating a layer which is $2\Delta\tau$ thick. The new layer is then doubled to create a layer of optical depth $4\Delta\tau$ and so on until the desired optical depth is achieved in N steps as $\tau = 2^{N}\Delta\tau$. Although the doubling equations are used for homogenous layers there is still an exponential dependence with optical depth on the solar pseudo source. Wiscombe (1976) extended the method of doubling to the case with an exponentially varying solar source as follows.

$$
\begin{aligned}
T_{2n}^{+} &= T_n^{+}\Gamma_n^{+}T_n^{+} \\
T_{2n}^{-} &= T_n^{-}\Gamma_n^{-}T_n^{-} \\
R_{2n}^{+} &= T_n^{+}\Gamma_n^{+}R_n^{+}T_n^{-} + R_n^{+} \\
R_{2n}^{-} &= T_n^{-}\Gamma_n^{-}R_n^{-}T_n^{+} + R_n^{-} \\
\Sigma_{2n}^{+} &= T_n^{+}\Gamma_n^{+}\left(R_n^{+}\Sigma_n^{-} + \gamma^n\Sigma_n^{+}\right) + \Sigma_n^{+} \\
\Sigma_{2n}^{-} &= T_n^{-}\Gamma_n^{-}\left(\gamma^n R_n^{-}\Sigma_n^{+} + \Sigma_n^{-}\right) + \gamma^n\Sigma_n^{-} \\
\gamma &= e^{-\Delta\tau/\mu_o}
\end{aligned}
\tag{3.32}
$$

3.6 Surface Reflection

3.6.1 The Surface Boundary Condition

In general the surface will reflect, absorb and emit radiation. Thermal emission is negligible at the solar wavelengths used in this research. Therefore, only the scattering properties of the surface will be considered here. Two types of surfaces are allowed in the model, a Lambertian surface and a rough ocean surface.

Following Stamnes et al. (1988), the general surface boundary condition is given by

$$
\tilde{I}^{+}(s) = \frac{1}{\pi}\int_0^{2\pi}\int_0^{1}\tilde{\rho}(\mu,\phi,\mu',\phi')\tilde{I}^{-}(s)\mu' d\mu' d\phi' + \tilde{\rho}(\mu,\phi,\mu_o,\phi_o)F_o\frac{\mu_o e^{-\tau/\mu_0}}{\pi} \tag{3.33}
$$

where $\tilde{\rho}$ is the bidirectional surface reflection function (BRDF), which describes the angular dependent surface reflection. In the case of vector radiative transfer the BRDF is a matrix describing the fully polarized surface reflection in an analogous manner to the phase matrix. This surface phase matrix must have the same angular rotations applied to it as an atmospheric phase matrix. The surface phase matrix used to perform radiative transfer calculations must then be given by

$$
\tilde{\rho}(\Theta) = L(\pi - i_2)\rho(\Theta)L(-i_1) \tag{3.34}
$$

The structure of Equation 3.34 is analogous to 3.4.

The surface boundary condition is in physical space. As with the RTE it contains complicated angular integrals. In order to solve for the Fourier modes of the radiance field at the surface the Fourier transforms, 3.9, are applied to the boundary condition and the BRDF is written as a Fourier series as in equation 3.8. After applying the Fourier transforms and applying numerical quadrature to the integral over zenith angle the boundary condition becomes

$$I_m^+(s;\mu_i) = \sum_{j=1}^{n} \mu_j w_j \rho_m(\mu_i,\mu_j) I_m^-(s;\mu_j) + \rho_m(\mu_i,\mu_o) F_o \frac{\mu_o e^{-\tau/\mu_0}}{\pi} \tag{3.35}$$

Here ρ_m has an analogous form as equation 3.15. The Fourier coefficients of the BRDF are found by evaluating the BRDF at a number of evenly spaced azimuth points for each pair of quadrature angles and then using an FFT routine to transform each series in azimuth angle.

3.6.2 The Surface Adding Equations

Treating the surface as an infinitesimal layer, the spectrally decomposed surface boundary condition can be written in the matricial framework of the interaction principle as a surface reflection matrix and a surface source vector

$$I_m^+(s) = R_s I_m^- + \Sigma_{m,s} \tag{3.36}$$

Following similar steps to Equations 3.28 - 3.31, the equations for adding a surface layer to an atmospheric layer are derived as

$$\begin{aligned}
R^+ &= R_1^+ + T_1^+ \Gamma^+ R_s T_1^- \\
R^- &= R_1^- \\
T^+ &= T_1^+ \\
T^- &= \Gamma^- T_1^- \\
\Sigma^+ &= \Sigma_1^+ + T_1^+ \Gamma^+ \left[R_s \Sigma_1^- + \Sigma_s^+ \right] \\
\Sigma^- &= \Gamma^- \left[\Sigma_1^- + R_1^- \Sigma_s^+ \right]
\end{aligned} \tag{3.37}$$

where

$$\Gamma^{+} = \left[E - R_s R_1^{-}\right]^{-1}$$
$$\Gamma^{-} = \left[E - R_1^{-} R_s\right]^{-1}$$

3.6.3 Lambertian Reflection

Lambertian, or isotropic, reflection implies equal reflection in all directions. The reflection is assumed to be unpolarized. The BRDF for this type of reflection is simply a constant value between 0 and 1 in the ρ_{11} element of the matrix and zero for all other elements. As a result only the $m = 0$, or azimuthally averaged, mode is non-zero and the Fourier transform of the BRDF is simply the surface albedo.

3.6.4 The Rough Ocean Model

A realistic, rough ocean model was employed for this research. The model follows the empirical studies of Koepke (1984) and Cox and Munk (1954). The rough ocean BRDF follows a kernel model as the sum of distinct scattering functions.

$$\rho(\Theta) = a_o + \sum_k a_k f(\Theta; b) \tag{3.38}$$

where a_o is an isotropic term, a_k are weights and b is a set of non-angular parameters.

In the model of Koepke (1984) the BRDF is given by

$$\rho = A r_f + (1 - A) r_s + (1 - A r_f) r_u \tag{3.39}$$

r_f, r_s and r_u are the reflection due to foam patches and streaks, the specular reflection and the water leaving radiance respectively. A is the area of the ocean surface which is covered with foam. This area is primarily a function of the wind speed. In this work the water leaving

radiance will be neglected, leaving the reflection due to foam and the specular reflection of the ocean surface. This assumption can lead to significant errors at wavelengths below about 600 nm, Morel (1983). The area of the ocean surface covered by foam is calculated using the empirical relationship

$$A = 2.95\text{x}10^{-6}v^{3.52} \tag{3.40}$$

Here v is the surface wind speed.

The reflection of the foam patches is assumed to be isotropic. Therefore r_f is simply a constant albedo, which may be found empirically. However, there are several complications. It has been found that the albedo of foam patches differs from that of foam streaks. Also, the albedo of sea foam has been observed to decrease with time while it's area increases. To account for these effects Koepke (1984) introduces the concept of effective reflectance defined

$$r_f = f_{ef} r_{o\lambda} \tag{3.41}$$

where f_{ef} is an empirically derived efficiency factor and $r_{o\lambda}$ is constant measured value of the spectral reflectivity of foam bubbles. The efficiency factor is given as

$$f_{ef}(v) = \frac{f_{ef,p} + f_{ef,s} SP(v)}{1 + xSP(v)} \tag{3.42}$$

where

$$\begin{aligned} x &= 0.5 \\ f_{ef,p} &= 0.4 \\ f_{ef,s} &= 0.18 \\ SP &= 0, \qquad v \le 8.5\, m/s \\ SP &= -2.1 + 0.24v, \qquad v > 8.5\, m/s \end{aligned} \tag{3.43}$$

Here x is a factor which corrects for the estimated under-detection of sea foam. The subscripts p and s on the efficiency factor refer to patches and streaks respectively. SP is the ratio of foam streaks to patches.

The specular reflection of the ocean surface from one angle into another is given as the specular reflection of a flat surface weighted by a probability distribution describing the likelihood of that slope.

$$r_s = PDF(\mu_i, \mu_r, \phi; v) P_s(\Theta, m) \tag{3.44}$$

Here, $P_s(\Theta, m)$ is the Fresnel phase matrix described in the next section. The PDF is a function of the incoming and outgoing scattering angles as well as the wind speed. The probability the sea surface slope distribution is modeled using the Cox and Munk (1954) formulation. In their seminal work, they found that the distribution of slopes is nearly Gaussian with a slight dependence on the wind direction, which will be ignored here. Spurr (2004) gives the PDF of the slope distribution as

$$P = \frac{1}{4|\mu_i||\mu_r|\pi\sigma^2\chi^4} \exp\left(\frac{-\tan(\pi/2) - \sin^{-1}\chi}{\sigma^2}\right) \tag{3.45}$$

where

$$\chi = \frac{|\mu_i| + |\mu_r|}{2\xi}$$
$$\xi = \cos(\Theta/2)$$

Here, σ^2 is the mean square slope variance, which was measured as a function of wind speed by Cox and Munk (1954) as

$$\sigma^2 = 0.003 + 0.00512v \tag{3.46}$$

3.6.5 Fresnelian Reflection

Fresnel's equations describe the specular reflection of radiation from a flat surface. The equations of reflection for both horizontally and vertically polarized radiation may be written as

$$S_2 = \frac{m^2\zeta - \sqrt{m^2 - \zeta^2 - 1}}{m^2\zeta + \sqrt{m^2 - \zeta^2 - 1}}$$
$$S_1 = \frac{\zeta - \sqrt{m^2 - \zeta^2 - 1}}{\zeta + \sqrt{m^2 - \zeta^2 - 1}} \tag{3.47}$$

where ζ is again given by the cosine of the incidence angle and m is the ratio of the complex indices of refraction of the surface medium to the atmospheric medium, Spurr (2004). The value of m is taken to be a constant 1.344 for ocean water in this work, although in general it may vary due to the oceanic constituents, particularly chlorophyll concentration. It is also, in general, wavelength dependent. The usual transformation of these equations into a phase matrix for the scattering of the Stokes vector must be performed using the relations of Equation 2.8. The rotated phase matrix is then formed from the scattering matrix by applying the rotations given by 3.3. This results in a surface phase matrix of the same form as equation 3.4. This phase matrix may then be employed in the rough ocean surface model described in the previous section.

CHAPTER 4

FORWARD MODEL OPTICAL DEPTH SENSITIVITY ANALYSIS

4.1 Introduction

This chapter introduces an atmospheric aerosol model. This model is used to perform a sensitivity analysis for aerosol optical depth (AOD) at the two POLDER aerosol channels. These channels have band centers in the visible and NIR spectrum at 670.2 and 860.8 nm. This sensitivity analysis is an initial exploration into the development of a two-channel AOD retrieval. A two-channel AOD retrieval will provide an estimate of the columnar aerosol load. It also allows an estimate of the size of the aerosol particles through the Angstrom exponent defined

$$\alpha = \frac{\ln\left(\tau_{670.2}/\tau_{860.8}\right)}{\ln\left(670.2/860.8\right)} \tag{4.1}$$

Large Angstrom exponents generally correspond to small aerosol particles, Stephens (1994).

The sensitivity study includes a thorough scene dependent error analysis which accounts for the various scattering geometries and aerosol loads. The error analysis is a necessary step in determining the level of non-uniqueness in the retrieval problem. This non-uniqueness is introduced by assuming an atmospheric aerosol model. The problem boils down to this. An atmospheric aerosol model imposes artificial constraints on the radiative transfer calculations. In

nature there are fluctuations in the assumed parameters about this artificially imposed model and these fluctuations produce variations in the TOA radiance field.

For a retrieval to be feasible, variations in the radiance field must also result from changes in the retrieval parameter, in this case the wavelength dependent optical depth. An ideal retrieval will have a large signal, or large radiance variation due to the retrieval parameter, and low noise, or variations in the radiation due to fluctuations about the assumed model parameters. The ratio of these two quantities, the signal to noise ratio (SNR), will be calculated and discussed in this chapter as the fundamental parameter defining the uniqueness of the retrieval.

4.2 Atmospheric Aerosol Model

4.2.1 Aerosol Size Distribution

It has been shown that aerosols follow a multi-modal lognormal number size distribution, d'Almeida et al. (1991)

$$N(r) = \sum_{i=1} \frac{N_{o,i}}{\sqrt{2\pi}\sigma_i r} \exp\left[\frac{-\left(\ln r - \ln r_{g,i}\right)^2}{2\sigma_i^2}\right] \tag{4.2}$$

where $N_{o,i}$, σ_i, $\ln r_{g,i}$ are the number concentration, standard deviation of the distribution of the natural logs of the r's, and the mean of the distribution of the natural logs of the r's, respectively. Each mode represents a single independent source and in principle several modes may coexist at any given time in any given place. The total size distribution consists of the superposition of all the modes.

It is convenient to restrict ourselves to a bimodal aerosol size distribution. The small mode is referred to as the accumulation mode while the larger mode is called the coarse mode.

Direct measurements of aerosol size distributions have demonstrated that the number concentration of the small mode is roughly three orders of magnitude larger than that of the large mode, d'Almeida et al. (1991).

4.2.2 Aerosol Model Parameters

For the purposes of this research the analysis has been restricted to one particular aerosol model. A model representative of a clean maritime environment has been chosen for in depth analysis. The parameters defining this model are derived from the climatology of d'Almeida and the MODIS aerosol ocean retrieval algorithm and are given in Table 4.1, [d'Almeida et al. (1991), Kaufman and Tanre (1998)]. These parameters correspond to a highly scattering, primarily sulfate type aerosol. The size distribution here is described in terms of the effective radius and effective variance of the two modes defined following Asano (1995)

$$\begin{aligned} r_e &= r_g \exp\left[\frac{5}{2}\sigma^2\right] \\ v_e &= \exp\left[\sigma^2\right] - 1 \end{aligned} \tag{4.3}$$

The Mie scattering matrix, single scatter albedo (SSA) and AOD for any given wavelength are derived entirely from the ten parameters given in Table 4.1. In fact, there are only nine free parameters which determine the scattering matrix and SSA, as only the ratio $\gamma = N_{o,a}/N_{o,c}$ matters for the calculation of these parameters, and not the individual values of the N_o's. The value of γ given in Table 4.1 is 1000. The scattering matrix elements for the aerosol model are shown in Figure 4.1.

Unlike the scattering matrix and single scatter albedo, the determination of the extinction and scattering coefficients is dependent on the individual values of the N_o's. However, for the purposes of the analysis which follows, the scattering matrix elements and SSA will be

calculated using the aerosol model. The ratio of the two AOD's, $\Gamma = (\tau_{670.2}/\tau_{860.8})$, is also held constant as that determined by the model. Doing so assumes that variations in optical depth are the result of variations of the two N_o's which maintain the ratio between the two at $\gamma = 1000$.

	Accumulation Mode	Coarse Mode
N_o (m^{-3})	$1x10^9$	$1x10^6$
r_e (μm)	0.11	1.9
v_e (μm)	0.6	0.6
m_r	1.45	1.45
m_i	0.0035	0.0035

Table 4.1: The parameters defining the size distribution and optical properties of the clean maritime aerosol model.

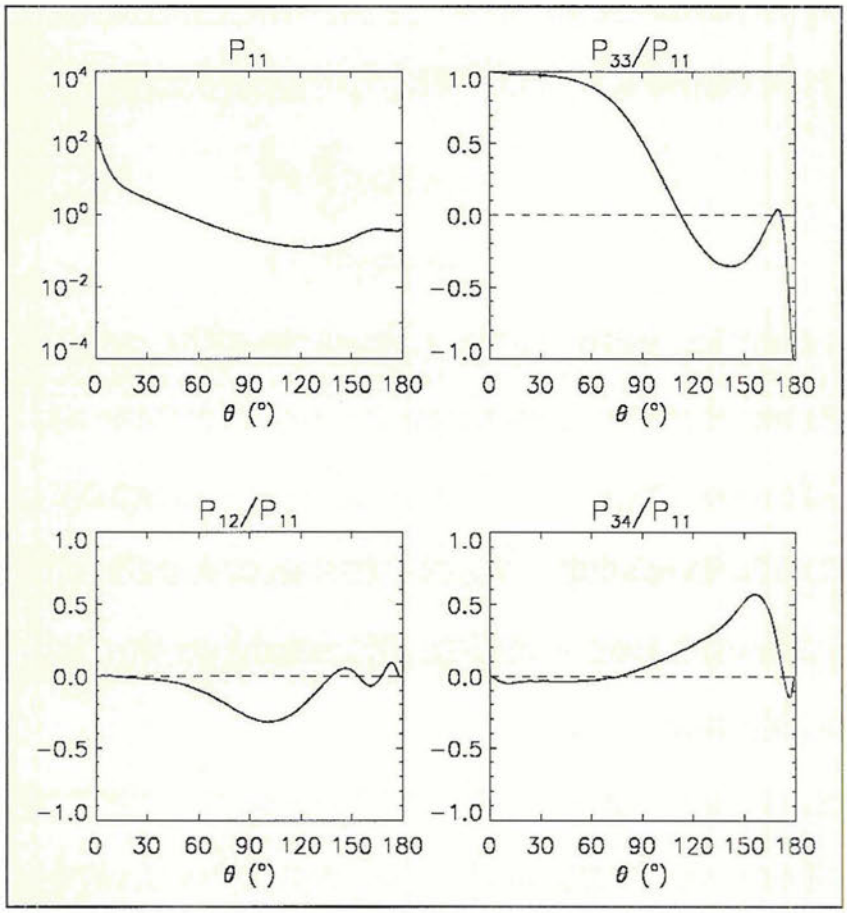

Figure 4.1: The Scattering matrix elements as a function of scattering angle at 670.2 nm for the Clean Maritime Model given by Table 4.1

4.2.3 Atmospheric Model

The forward model described in Chapter 3 has been used to perform the sensitivity analysis which follows. Top of the Atmosphere (TOA), polarized angular radiance fields have been produced at two wavelengths; 670.2 and 860.8 nm. The model has been operated with N = 24 streams, $\Delta\phi$ = 256, and with 3 Stokes parameters [I, Q, U]. The number of streams and sampled azimuth points were chosen to ensure radiance convergence and in order to fully capture the variations in the angular radiance field. The truncated Stokes parameter was used because this is the vector measured by the POLDER instrument. For small solar zenith angles less than about 30 degrees, 10 azimuth modes were solved in order to reconstruct the radiance fields. It was found that 30 modes were needed to ensure radiance convergence when the solar zenith angle was much larger than 30 degrees. More modes were needed at the large solar zenith angles due to the large surface reflection at these angles. The surface reflection function is essentially a sharp spike in the glint direction, which requires a large number of Fourier modes in order to accurately reconstruct it.

A two-layer atmosphere was considered. The upper layer consisted of a Rayleigh scattering molecular atmosphere. The optical depth of this layer was calculated using Equation 2.11. The lower layer consisted of all of the aerosol scattering and absorption. The Koepke surface model was used assuming a wind speed of 7 m/s. For the purposes of this first look at the retrieval problem, molecular absorption has been ignored. In order to justify this assumption the molecular optical depth, in the POLDER spectrum, has been calculated from the HITRAN database for the McClatchey mid-latitude summer atmosphere using the method outlined in Chapter 2. Figure 4.2 shows the absorption optical depth of water vapor and oxygen in the visible and near infrared spectrum. Superimposed on this plot are the POLDER instrument

response functions. The two channels used in this work are relatively free from absorption. There is slightly more contamination in the 860.8 channel, due to water vapor absorption, than at 670.2 nm. The channels with wavelengths less than 670 nm have not been considered due to the significant water leaving radiances at these wavelengths. Water leaving radiances have not been modeled in this research, which could lead to small errors at 670.2 and negligible errors at 860.8 nm, Morel (1983).

Two of the POLDER radiance products consist of the normalized total and polarized radiances. These quantities are defined as

$$I_n = \frac{\pi I}{F}$$

$$P_n = \frac{\pi}{F}\sqrt{Q^2 + U^2}$$

Here F is the incident TOA solar irradiance. In the analysis which follows, the subscript n notation will be dropped for convenience and all radiances will refer to the normalized radiance unless otherwise indicated.

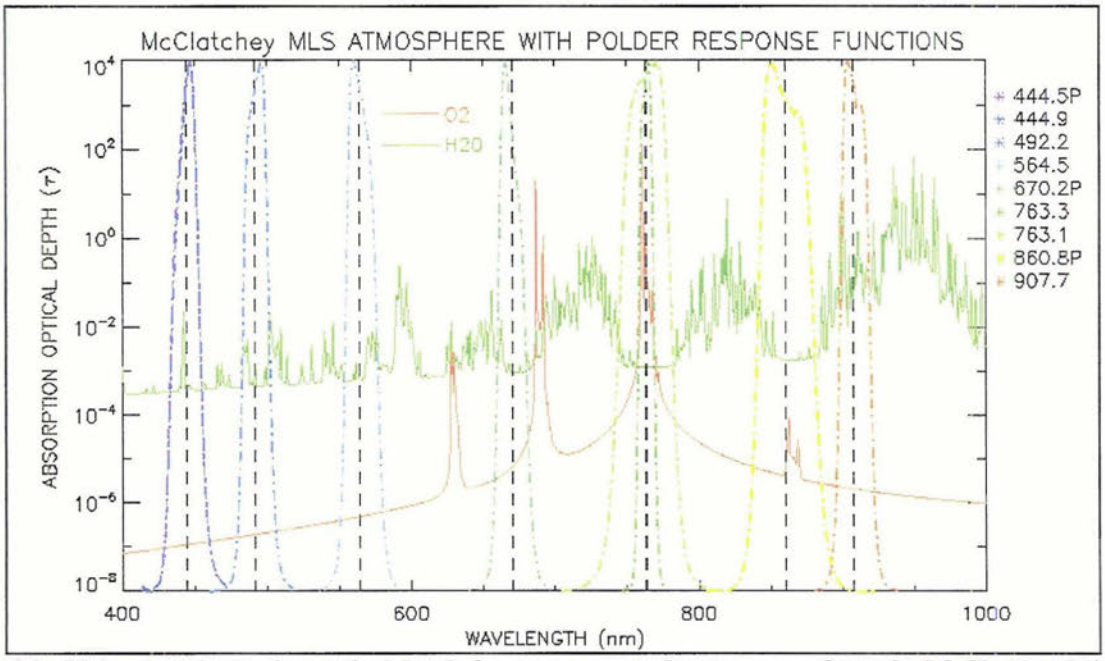

Figure 4.2: Molecular absorption optical depth due to oxygen and water vapor from the McClatchey Mid-Latitude Summer Atmosphere in the POLDER spectral region (Solid Lines). Superimposed are the POLDER instrument response functions (Dashed Lines).

4.3 Sensitivity Analysis

4.3.1 Example Cases

As a first step towards developing an aerosol optical depth retrieval, we have restricted ourselves to a thorough analysis of the model described in Table 4.1. Fifteen distinct scenes have been analyzed in order to develop an understanding of the multi-angular polarized AOD retrieval problem. All combinations of three solar zenith angles [0°, 30°, 60°] and five optical depths [0.1, 0.2, 0.5, 1.0, 1.5] have been analyzed.

4.3.2 Scene Dependence

Examining the mean values of the exitant TOA radiances for each scene is helpful in developing an understanding of how aerosols affect the reflection from the Earth-atmosphere system. Figure 4.3 shows plots of the mean total and polarized intensities, weighted by the angular area, for all fifteen cases. The top row contains the average total intensities at both wavelengths while the bottom row contains the averaged polarized intensities at each wavelength. It is immediately evident that the total and polarized radiances are brighter at 670.2 than they are 860.8 nm. This is primarily a function of the greater Rayleigh optical depth at shorter wavelengths. However, it is also a function of the larger AOD and backscatter at the shorter wavelength for this aerosol model. Note that the scale for the plots of total intensity is five times as large as the scale for the plots of polarized intensity.

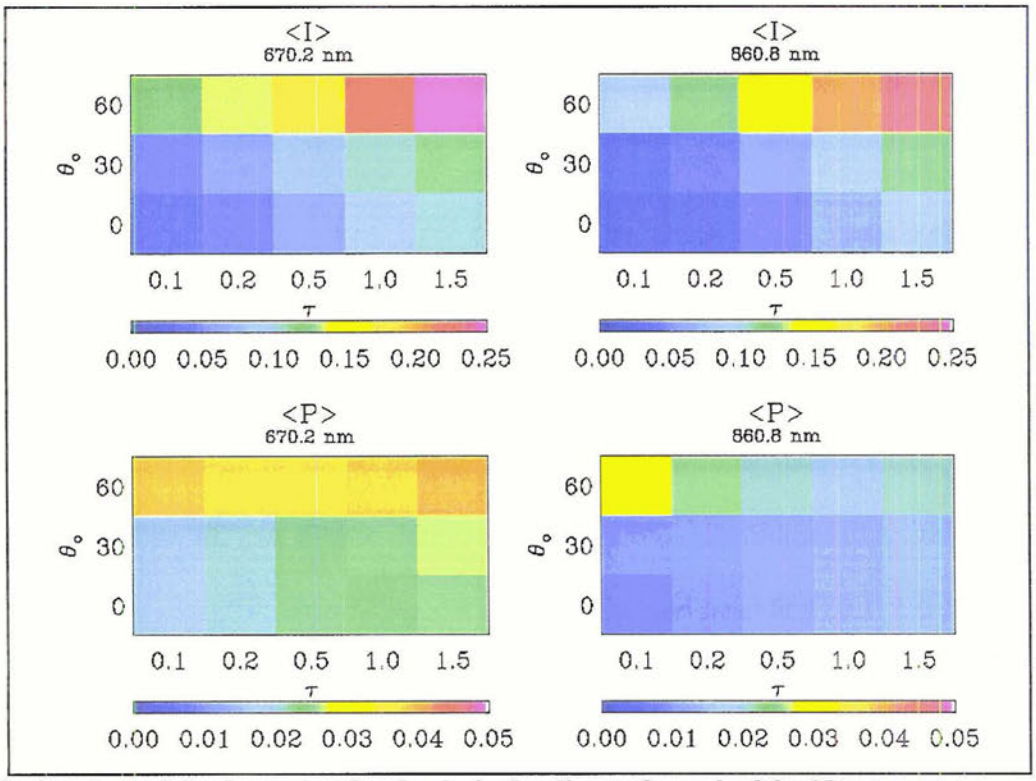

Figure 4.3: Angular weighted mean total and polarized radiances for each of the 15 test cases.

There is a clear pattern of increasing average TOA total intensity with increasing optical depth and with increasing solar zenith angle. These results are not surprising. Both an increasing optical depth and zenith angle increase the aerosol optical path length of the direct solar beam. This causes an increase in the extinction of the direct solar beam according to Beer's law. Due to the high single scatter albedo of the aerosol model, scattering dominates this extinction and subsequently an increase in the reflection to space is observed.

The polarized intensities show a similar pattern as the total intensities. There is a general increase in the polarized radiance with increasing optical depth and solar zenith angle. The same arguments made for total intensities explain this behavior. The exception to this rule occurs at the large solar zenith angle of 60°. At 670.2 nm there is a relative minimum at $\tau = 0.2$ and at 860.8 nm there is a minimum at $\tau = 1.0$. These relative minima are the result of two competing effects. The large surface reflection at this large solar zenith angle contribute to a large

Fresnelian surface reflection polarizing effect. This results in the local maxima at low optical depths. As the aerosol optical depth increases, the polarizing effect of the surface reflection is masked by the scattering of upwelling photons from the surface. The result is a decrease in the mean polarized intensity with increasing aerosol optical depth at low AOD values. As the surface reflection is increasingly masked the polarized radiance begins to increase along with the total radiances. This is the result of increasing scatter of the down-welling radiance off of the aerosol layer. The reason that the relative minimum occurs at a lower optical depth at 670.2 than at 860.8 nm is that the scattering phase matrix at 670.2 has a greater polarizing effect than that at 860.8 whereas the polarizing effect of the surface has no wavelength dependence.

The fact that the average total polarized radiance tends to increase with increasing optical depth does not imply that aerosols have a polarizing effect. In order to determine the polarizing effect of aerosols a more relevant quantity is the degree of linear polarization, (P/I). This quantity can vary between 0 and 1, corresponding to states of natural light and fully polarized light, respectively. Plots of the angular weighted averages of this quantity are shown in Figure 4.4. It is observed that the degree of polarization decreases monotonically with increasing optical depth at all solar zenith angles and at both wavelengths. It should also be noted that the average modeled degree of polarization is relatively low, near 0.1 - 0.2. Also of note, is the greater degree of polarization at 670.2 than at 860.8 nm. This is again an effect of the greater depolarizing effect of aerosols at 860.8 than at 670.2 nm.

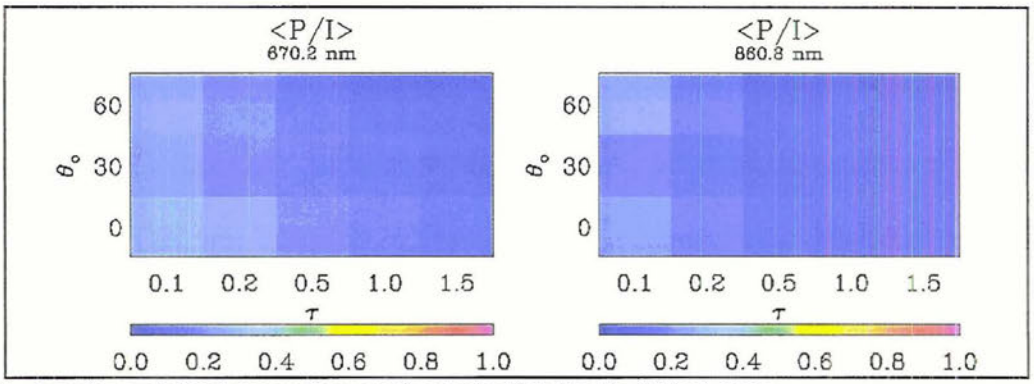

Figure 4.4: Angular weighted mean degree of polarization for the 15 test cases.

The mean values of total and polarized intensity are diagnostic tools which help to examine the physics of the radiative transfer. It must be kept in mind that each mean value corresponds to a field with angular structure. Understanding this angular structure is critical in characterizing the problem. As such, the total and polarized radiance fields are shown in Figures 4.5 - 4.14. The first five figures correspond to the five optical depth cases at 670.2 nm while the second five correspond to 860.8 nm. Both wavelengths have similar angular structures suggesting a large correlation between the channels. It is immediately evident that the exitant TOA fields demonstrate significant scene dependence.

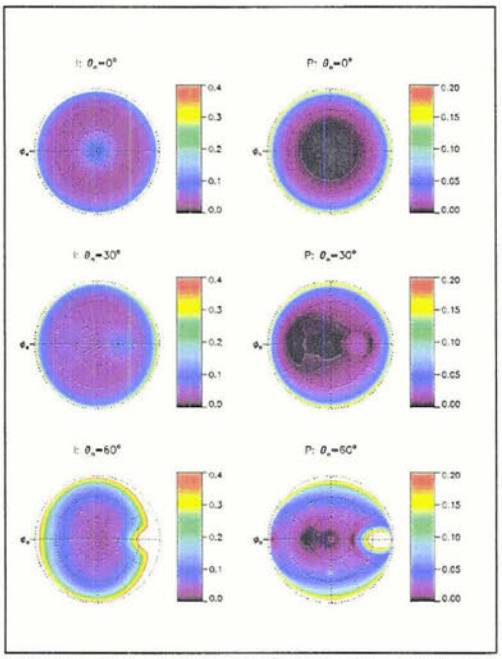

Figure 4.5: Angular TOA Radiance Field For $\tau = 0.1$, $\lambda = 670.2$ nm

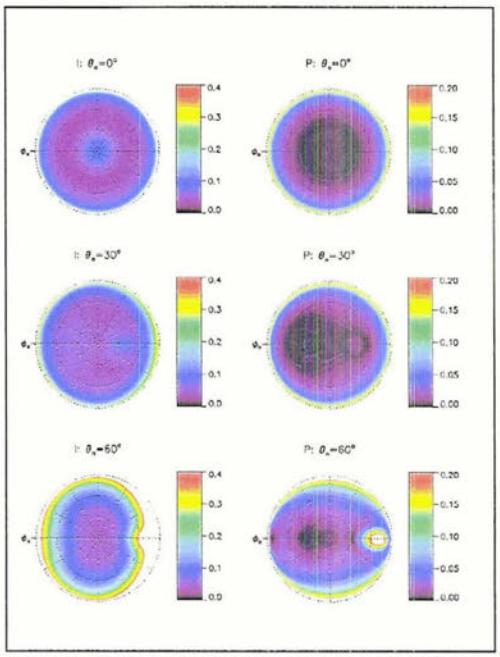

Figure 4.6: Angular TOA Radiance Field For $\tau = 0.2$, $\lambda = 670.2$ nm

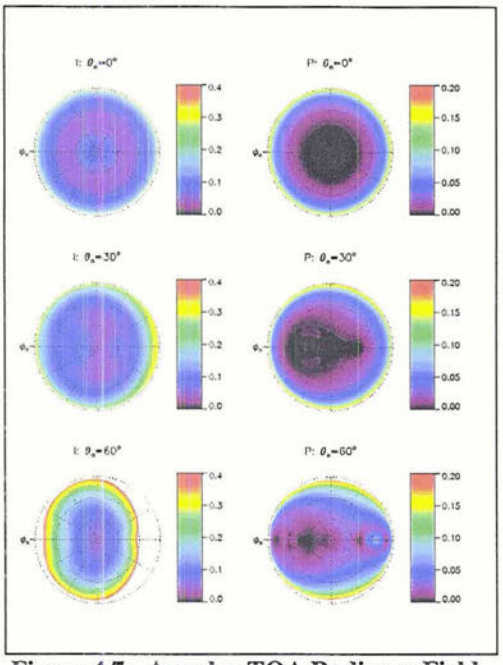

Figure 4.7: Angular TOA Radiance Field For $\tau = 0.5$, $\lambda = 670.2$ nm

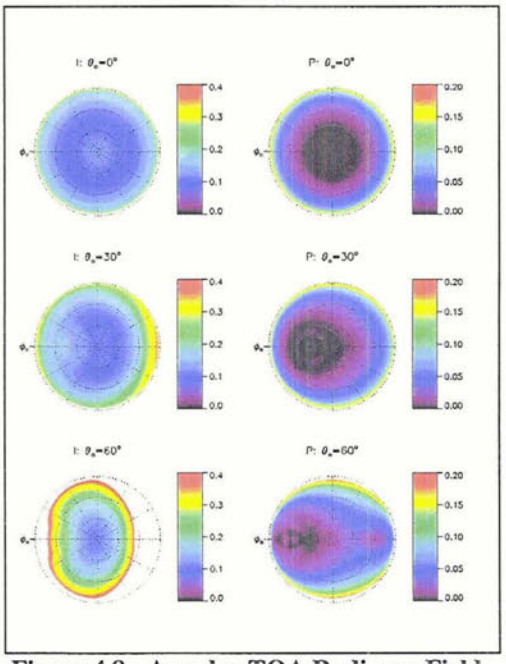

Figure 4.8: Angular TOA Radiance Field For $\tau = 1.0$, $\lambda = 670.2$ n

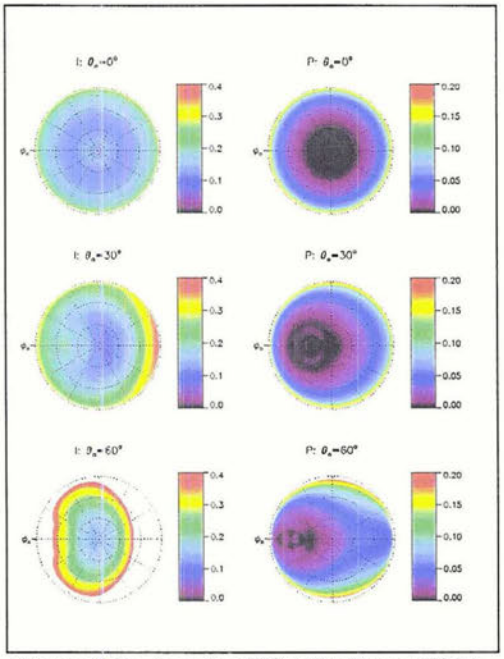

Figure 4.9: Angular TOA Radiance Field For $\tau = 1.5$, $\lambda = 670.2$ nm

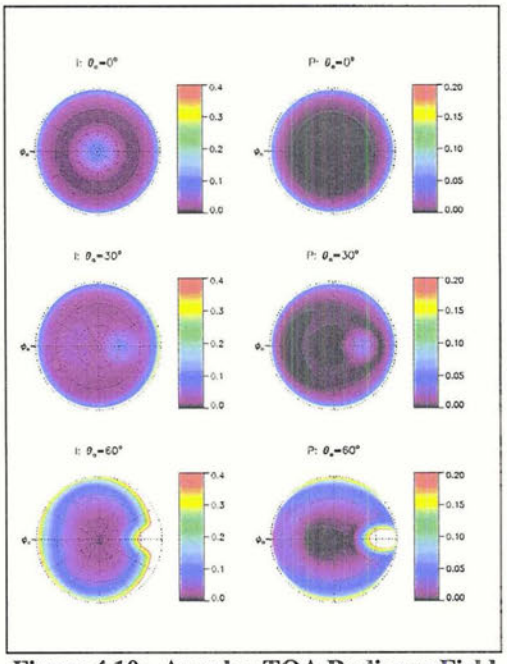

Figure 4.10: Angular TOA Radiance Field For $\tau = 0.1$, $\lambda = 870.8$ nm

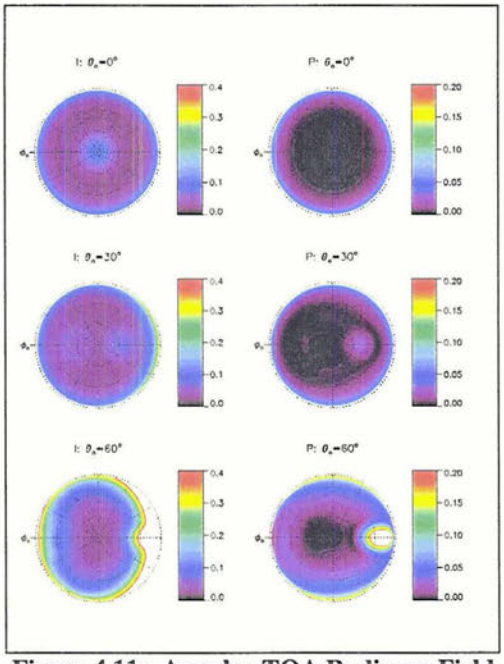

Figure 4.11: Angular TOA Radiance Field For $\tau = 0.2$, $\lambda = 870.8$ nm

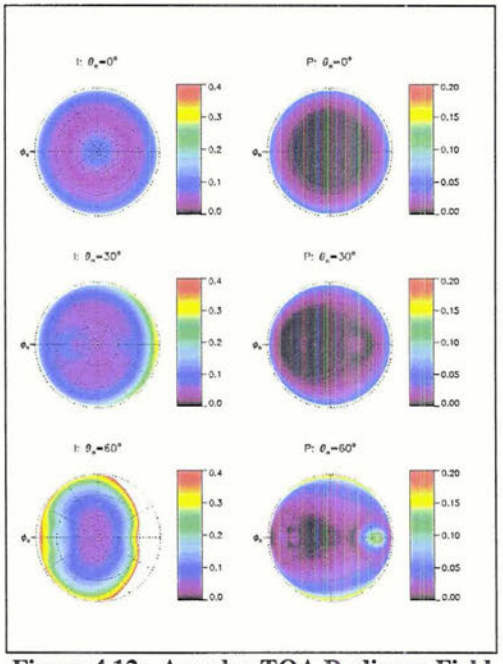

Figure 4.12: Angular TOA Radiance Field For $\tau = 0.5$, $\lambda = 870.8$ nm

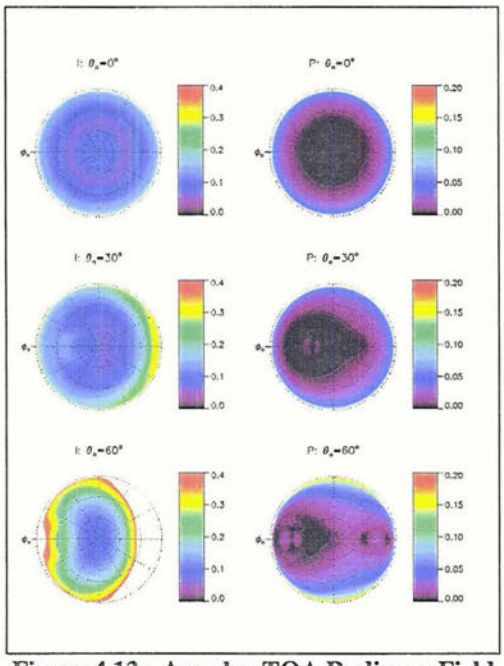

Figure 4.13: Angular TOA Radiance Field For $\tau = 1.0$, $\lambda = 870.8$ nm

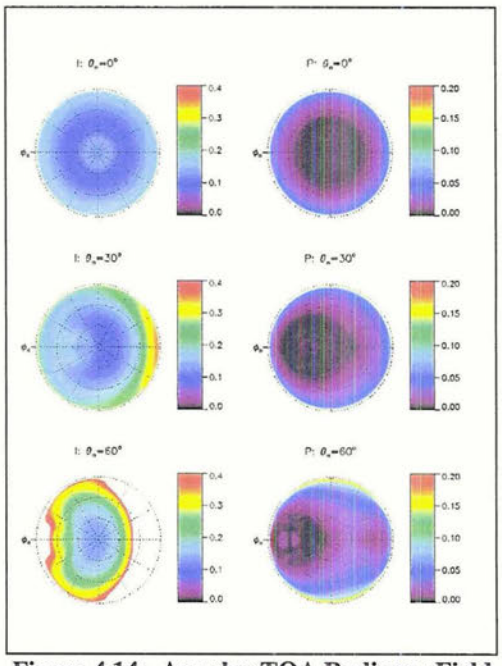

Figure 4.14: Angular TOA Radiance Field For $\tau = 1.5$, $\lambda = 870.8$ nm

The angular distribution of the total radiance is most strongly a function of the solar zenith angle. The most prominent angular features are the sun glint, the solar backscatter and limb brightening. The sun glint is the result of the direct surface reflection into the direction opposite the sun. This component of the reflection is present for all solar geometries, but increases strongly with increasing solar zenith angles. The component of the reflection due to the sun glint can be seen to decrease with increasing aerosol optical depth. This is the result of increasing scatter of the downwelling solar radiation by the aerosol layer in concert with an increasing scatter out of the glint direction of the upwelling radiation by the same layer. The solar backscatter feature becomes more prominent with increasing optical depth. This is a direct effect of the relative peak in scatter near 160° of the aerosol scattering phase function in combination with an increase in single scatter events.

The polarized radiances show much of the same angular structure as the total radiances, including sun glint, backscatter and limb brightening. However, the angular patterns associated with the polarized intensity are more complicated than those of the total radiance, particularly at large solar zenith angles where there is a high degree of asymmetry. This is a function of the interaction of the phase matrix elements shown in Figure 4.1. The oscillations in sign in the scattering matrix elements in the near backscattering directions are the primary mechanism for the oscillating lobes of high and low polarization in the backscattering directions.

4.3.3 Model Sensitivity to Aerosol Optical Depth

In order to assess the feasibility of an AOD retrieval, the sensitivity of the model to aerosol optical depth has been calculated about each test case. The sensitivity is defined as the derivative of the total and polarized radiance with respect to aerosol optical depth

$$S = \frac{\partial(I,P)}{\partial\tau} \tag{4.3}$$

The derivatives have been calculated numerically using a 5% perturbation in optical depth.

Figure 4.15 shows the angular area weighted average absolute value of the signal for all 15 test cases. Note that this plot has the same format and color scale as Figure 4.4, which showed the example case average radiances. It is evident that at both wavelengths and for both the total and polarized radiances the signal increases with both decreasing optical depth and with increasing solar zenith angle. The decrease in signal with optical depth follows from the asymptotic behavior of the reflection off a reflecting cloud, which tends to increase greatly at low optical depths and then level off rapidly. The larger signal at greater solar zenith angles is a function of the longer optical path length, which must be traversed by the direct solar beam. Similarly, the result is a larger change in optical path length at large solar zenith angles than at low solar zenith angles given the same change in optical depth. The sensitivity values tend to be slightly large at 860.8 than at 670.2 for both the total and the polarized radiances. This is a somewhat artificial artifact of the lower optical depth at 860.8 nm imposed by the aerosol model in combination with decreased molecular optical depth at longer wavelengths.

The angular fields of the absolute value of the sensitivity are shown in Figures 4.16 - 4.25. Note that the scale for the total intensity is five times that for the polarized intensity. The angular patterns at both wavelengths are extremely similar.

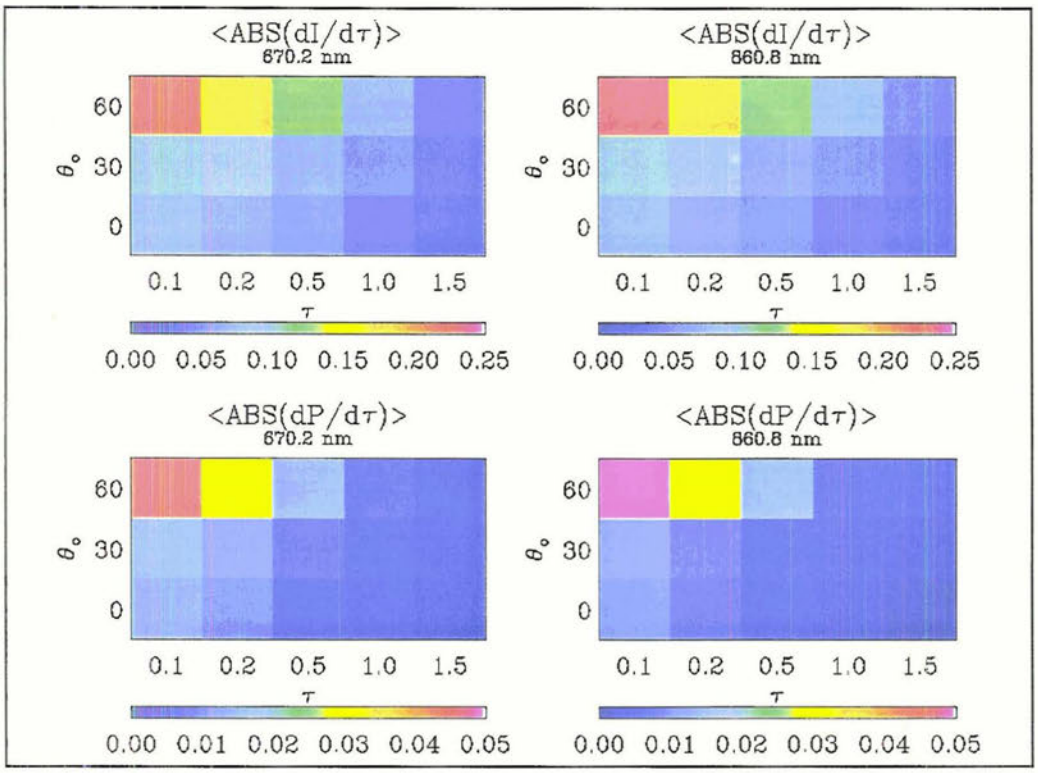

Figure 4.15: Angular weighted mean of the absolute value of the total and polarized signals for each of the 15 test cases.

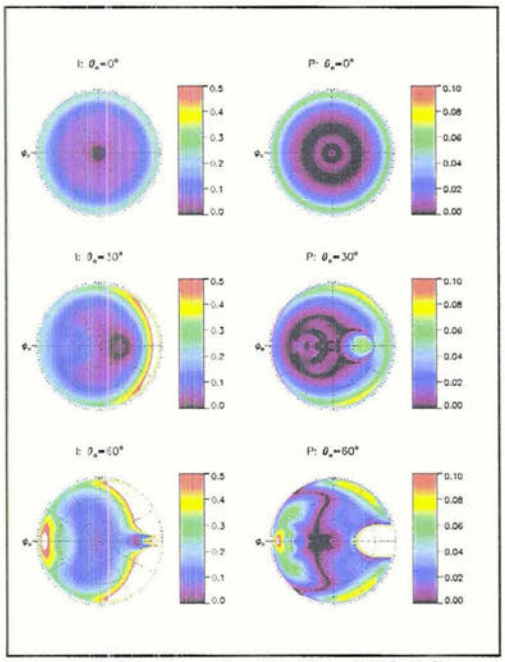

Figure 4.16: Angular Fields of TOA Signal For $\tau = 0.1$, $\lambda = 670.2$ nm

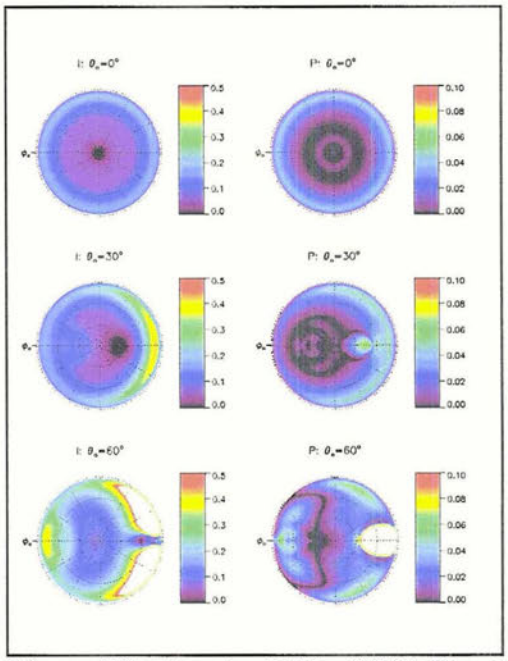

Figure 4.17: Angular Fields of TOA Signal For $\tau = 0.2$, $\lambda = 670.2$ nm

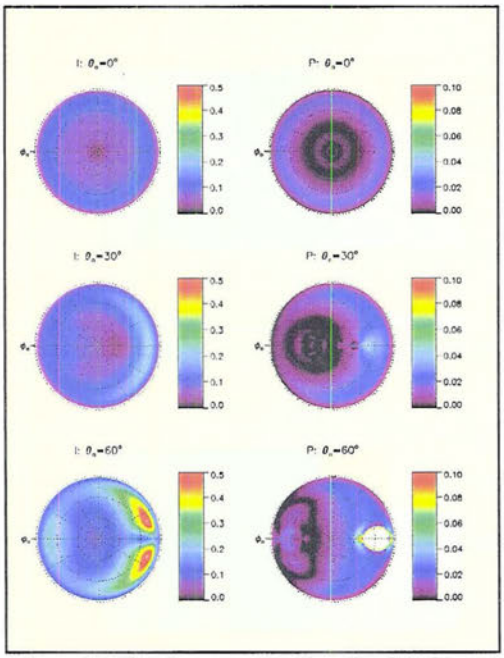

Figure 4.18: Angular Fields of TOA Signal For $\tau = 0.5$, $\lambda = 670.2$ nm

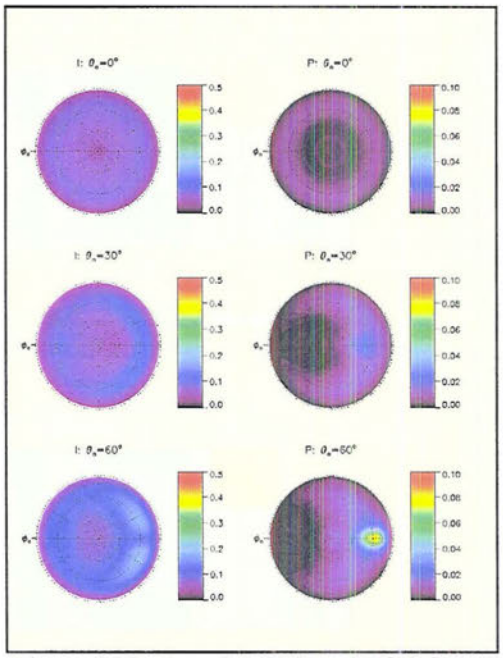

Figure 4.19: Angular Fields of TOA Signal For $\tau = 01.0$, $\lambda = 670.2$ nm

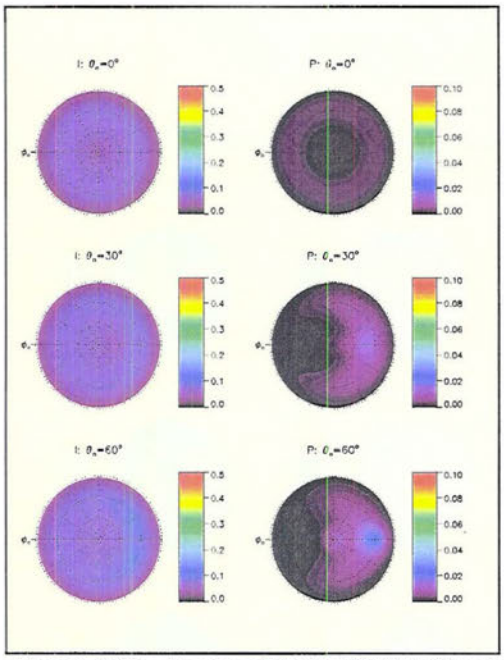

Figure 4.20: Angular Fields of TOA Signal For $\tau = 1.5$, $\lambda = 670.2$ nm

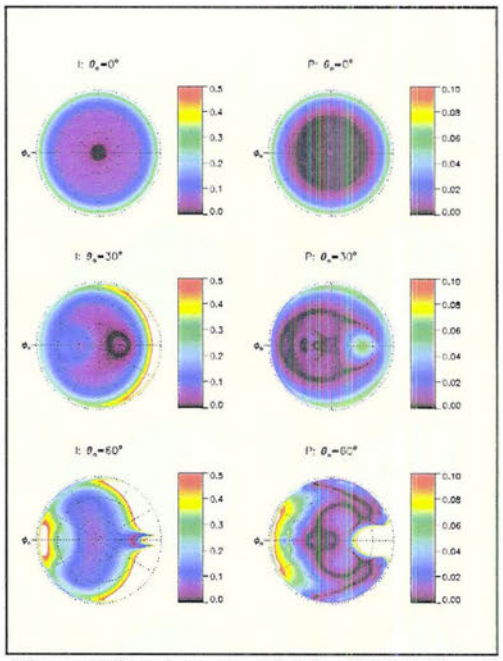

Figure 4.21: Angular Fields of TOA Signal For $\tau = 0.1$, $\lambda = 860.8$ nm

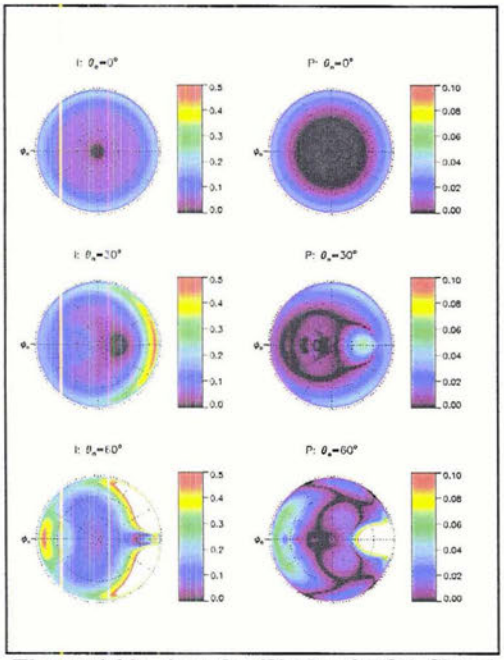

Figure 4.22: Angular Fields of TOA Signal For $\tau = 0.2$, $\lambda = 860.8$ nm

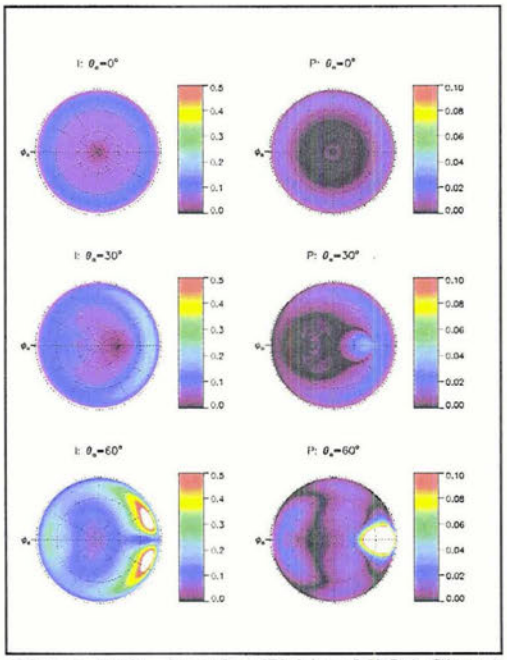

Figure 4.23: Angular Fields of TOA Signal For $\tau = 0.5$, $\lambda = 860.8$ nm

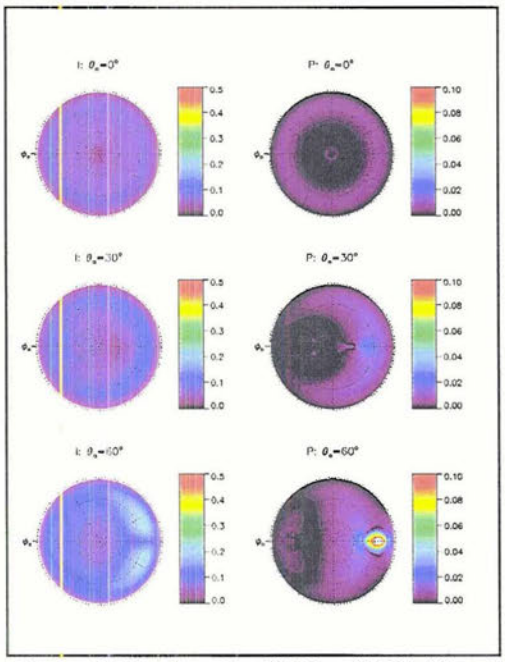

Figure 4.24: Angular Fields of TOA Signal For $\tau = 1.0$, $\lambda = 860.8$ nm

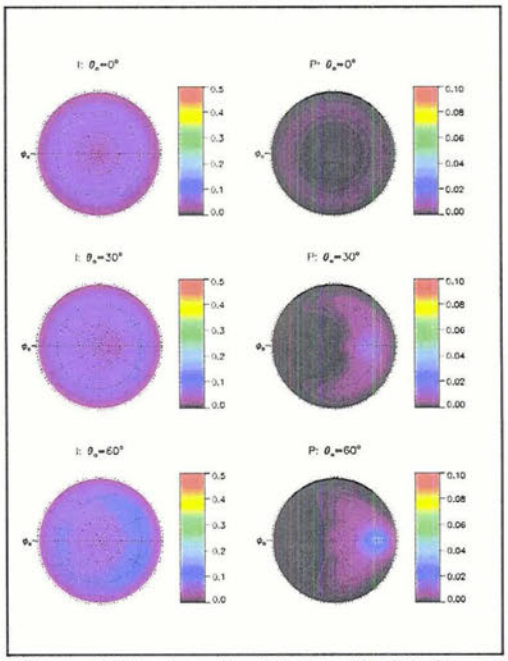

Figure 4.25: Angular Fields of TOA Signal For $\tau = 1.5$, $\lambda = 860.8$ nm

The general pattern for the total radiance sensitivity is an area of low sensitivity in the glint direction and an area of larger sensitivity in the backscatter direction. To a first approximation the TOA radiance can be estimated by a single scatter process. Under this assumption, the component of the radiance due to aerosol scattering is given by, Liou (2002)

$$I_a = \frac{I_o P \omega_o \tau_a}{4\pi\mu} \tag{4.4}$$

It should be noted that under this approximation the functional dependence of the radiance is the same for AOD and SSA. In light of the peak in the phase function at large scattering angles, it would be expected that there would be a peak in sensitivity in the backscatter direction, which is what is observed. For a directly overhead sun at low optical depths, the backscatter sensitivity is focused in a lobe around the sun with a minimum in the near backscatter direction. This is due to the contribution of the sun glint dominating the radiance in the near direct backscatter directions. The figures also show significant areas of high sensitivity at scattering angles near the horizon. This is a result of the larger changes in optical path length near the horizon than the zenith. Mathematically, this is seen as the $(1/\mu)$ factor in Equation 4.4, which is the single scatter approximation.

The polarized radiance field shows rather complicated angular structure of the sensitivity. At low optical depths there is large sensitivity in the sun glint region. This sensitivity will tend to be error prone as it is the result of the interactions between the aerosol layer and the surface reflection function, which contains many assumptions. This will lead to an unwanted propagation of errors associated with these assumptions. There tends to be sensitivity to the polarization in the area surrounding the backscatter direction, which is a direct result of the scattering matrix features at these angles. As with the total radiances, there is sensitivity near the horizon due to the increased optical path length. The sensitivity to the polarized radiance in the

backscatter direction demonstrates a lobe like structure which, as has previously been discussed, is a function of the oscillations in the single scatter phase matrix elements at large scattering angles.

4.3.4 Modeled Errors

The modeled TOA radiances, for any given geometry, are a function of both the optical depth as well as the many assumptions which have been made in defining both the aerosol and atmospheric models. In general, this is expressed mathematically as

$$y = F(x,b) + \delta \tag{4.5}$$

where y is the measurement vector, F is the forward model, x is a vector of the parameters of interest, b is a vector of forward model assumptions and δ is a measurement uncertainty (Rodgers, 2000). In this case x is a vector of length two consisting of the optical depth at 670.2 and 860.8. We would like to be able to infer the value of optical depth based on the measurement vector y. Here y is the vector of polarized and total radiances for both wavelengths and at a number of different viewing geometries.

Equation 4.5 demonstrates that our ability to map between the state space (x) and the measurement space (y) is a function of both measurement uncertainty as well as any assumptions, which are made in order to perform the radiative transfer calculations. Therefore, a realistic error estimate must take into account both the natural variability in the parameters in the vector b and the measurement uncertainty, δ.

An attempt has been made to quantify the errors associated with an AOD retrieval for each of the 15 scenes. Twelve different sources of error have been considered in calculating the angular dependent errors. Nine of these sources of error are associated with the aerosol model

assumptions described in section 4.2.2. The remaining three sources of error are associated with the surface reflection function, the vertical distribution of the aerosol and the measurement uncertainty. It should be noted that several sources of error have been ignored including gaseous absorption, non-sphericity of aerosols, water leaving radiances, thin cirrus, and three dimensional effects.

In order to define the errors associated with the nine assumed values of the parameters which define the aerosol optical properties, estimates of their dynamic range have been made. These estimates are again based upon the climatology of d'Almeida and the MODIS aerosol ocean retrieval algorithm and are given in Table 4.2, [d'Almeida et al. (1991), Kaufman and Tanre (1998)].

	Accumulation Mode	Coarse Mode
γ	+/- 1 order of magnitude	
r_e (μm)	+/- 0.02	+/- 0.15
v_e (μm)	+/- 0.1	+/- 0.1
m_r	+/- 0.07	+/- 0.07
m_i	+/- 0.0015	+/- 0.0015

Table 4.2: Estimates of the dynamic ranges of the parameters defining the clean maritme model.

Each of the parameters in Table 4.2 have been perturbed to the extremes given by their dynamic range. Radiative transfer calculations were then performed at these extremes. The error associated with each parameter is calculated as the difference in radiances at the two extremes.

As described in Chapter 3, the surface reflection is a function of wind speed only. In this study, a constant wind speed of 7 m/s has been assumed. To estimate the error associated with this assumption radiative transfer calculations have been performed at 2 and 20 m/s. In practice, the surface wind speed could be input from a number of sources. If this was done, the error in the surface reflection function should be calculated by perturbing all of the several assumed

empirical parameters which affect the reflection. The simple perturbation of the wind speed will, however, provide a first order estimate of how surface reflection function errors behave.

The error associated with the two layer atmospheric model described in section 4.2.3 have been estimated by performing multi-layer radiative transfer calculations which conserve the aerosol optical depth. These calculations are performed for an 8 layer atmosphere. The top layer begins at 7 km and continues to the TOA. This layer contains only molecular Rayleigh scattering. The bottom 7 layers consist of Rayleigh scattering mixed with an aerosol with a scale height of 1.5 km, d'Almeida et al. (1991).

Finally, measurement error is calculated as 2% of the modeled radiances, Hagolle et al. (1999). Assuming uncorrelated errors, the total error in each measurement is calculated as the square root of the sum of the square errors

$$\varepsilon_i = \sqrt{\sum_j \Delta_j^{\,2}} \tag{4.6}$$

where ε_i is the total error of each measurement. The i includes all measurement angles, both wavelengths and both the total and polarized radiances. Here Δ_j is the individual error due to the j'th error source.

Figure 4.26 shows plots of the averages of the angular weighted total errors for the fifteen test cases. Note the consistency of the format and color scales with Figures 4.3 and 4.15 which show respectively the average scene dependent radiances and the average absolute value of the sensitivities. At both wavelengths for both the total and polarized radiances, there is a clear pattern of increasing error with increasing optical depth and increasing solar zenith angle. This is a result of the fact that the primary sources of error are those which affect the aerosol optical properties. Both larger optical depths and large solar zenith angles imply a longer aerosol optical path length. A longer aerosol optical path implies a greater contribution of the total reflected

radiance from the aerosol layer and hence a greater contribution to the total error from those errors sources associated with the assumptions of the aerosol model.

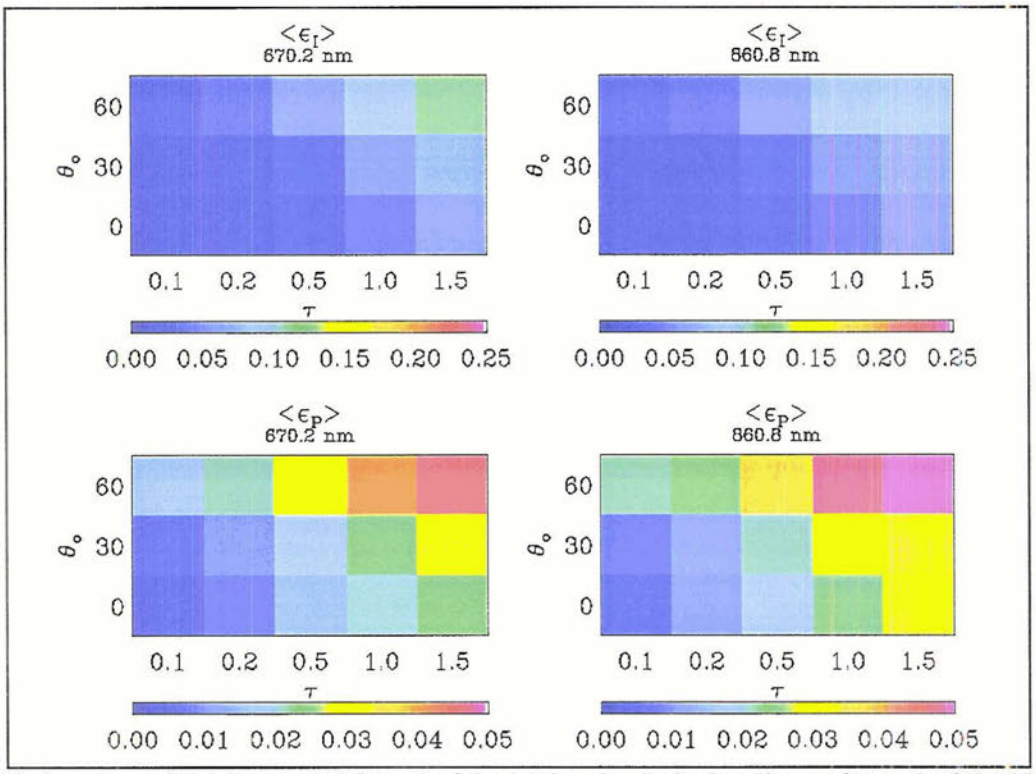

Figure 4.26: Angular weighted mean total error of the total and polarized radiances for each of the 15 test cases.

Figures 4.27 – 4.29 show the angular weighted averages of the individual sources of error. The three figures are in an order corresponding to solar zenith angles of 0° through 60°. The vertical axis corresponds to the twelve individual sources of error while the horizontal axis corresponds to the five optical depths. All of the plots show similar patterns. In general the errors of the modeled polarized intensities are slightly small than the total intensities. Note, however, that the total radiances tend to be about five times as large as the polarized radiance while the errors much less than five times as large. All of the individual error sources increase with the solar zenith angle. This follows from the increased aerosol optical path length and the increased surface reflection at larger solar zenith angles. The one source of error which

decreases with optical depth is the error associated with surface reflection. All of the other errors increase with increasing aerosol optical depth. This of course makes sense because the surface is masked at higher optical depths whereas all of the other sources of error are magnified as the AOD increases. The single largest source of error is that due to the ratio of the number concentrations γ. This is due to the large dynamic range of this value compared with the other assumed values. The measurement error is consistently one of the smallest sources of error. This highlights the importance of including the forward model assumptions in a thorough error estimate, as these are the primary sources of error.

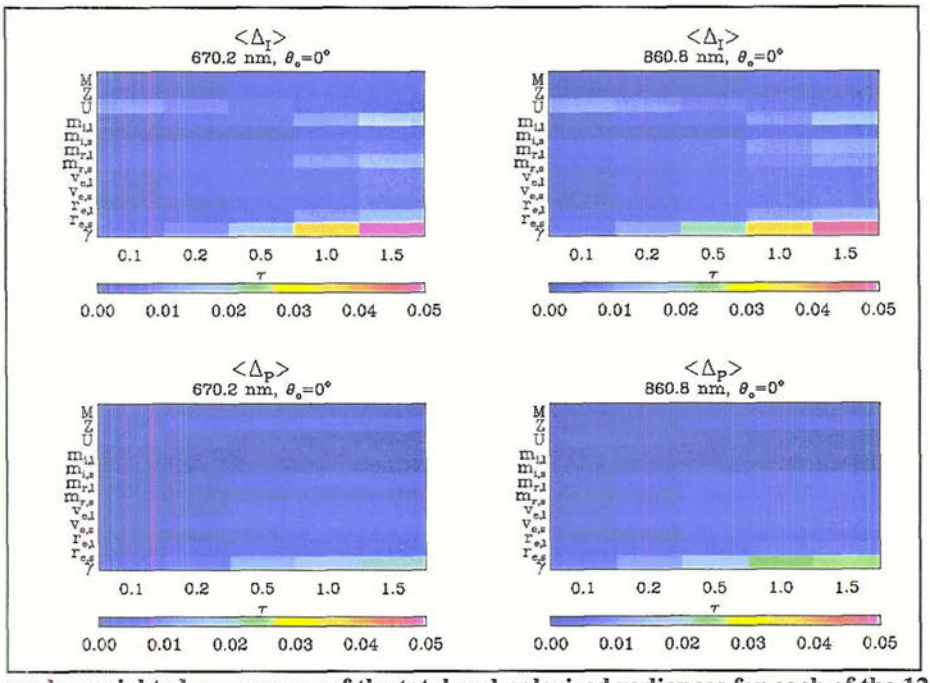

Figure 4.27: Angular weighted mean error of the total and polarized radiances for each of the 12 error sources. The solar zenith angle is 0°. The labels M, Z and U correspond to measurement, vertical distribution, and surface reflection error, respectively.

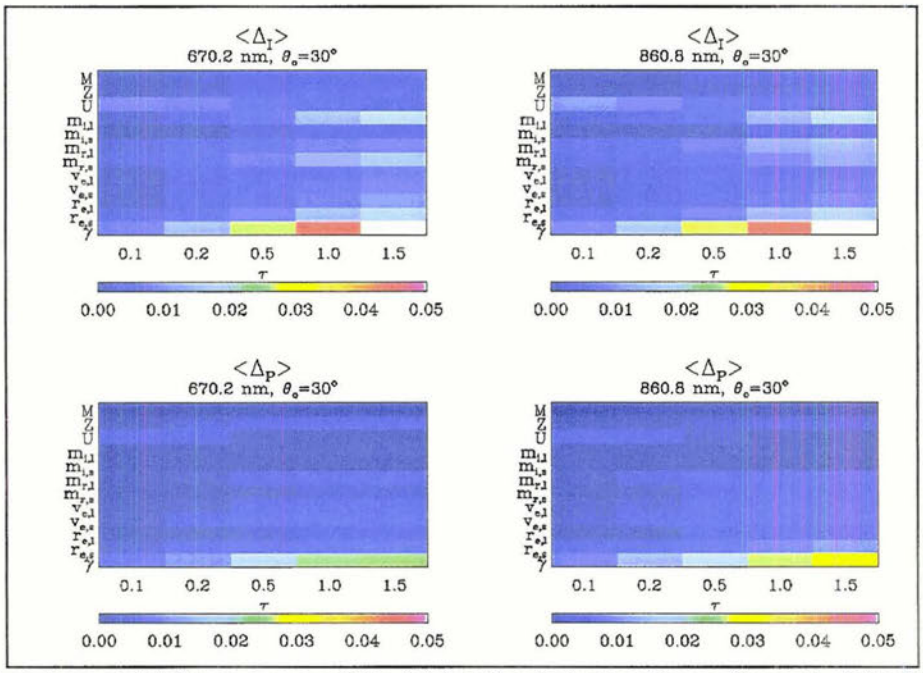

Figure 4.28: Angular weighted mean error of the total and polarized radiances for each of the 12 error sources. The solar zenith angle is 30°. The labels M, Z and U correspond to measurement, vertical distribution, and surface reflection error, respectively.

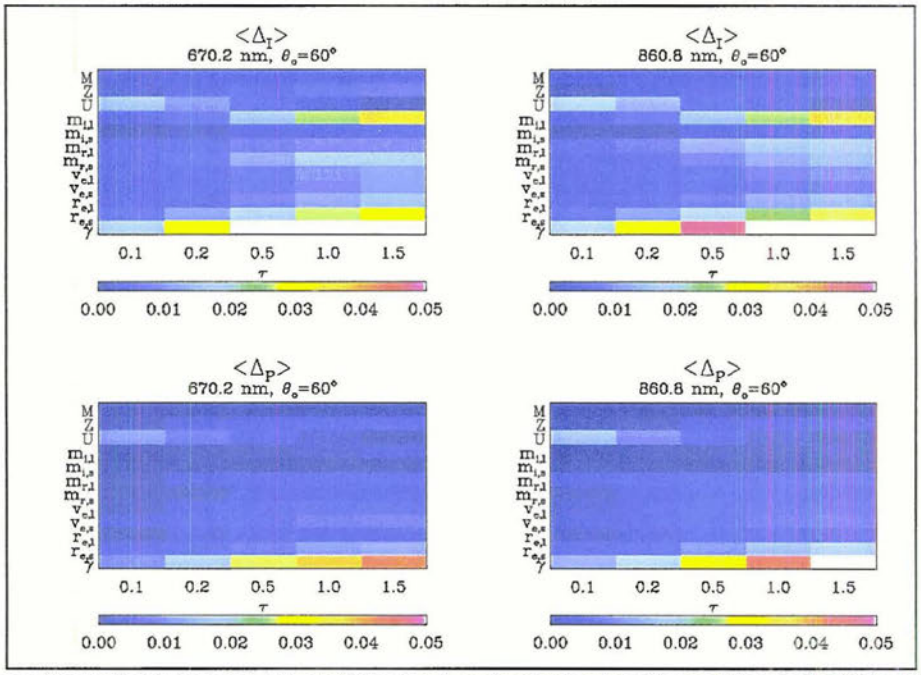

Figure 4.29: Angular weighted mean error of the total and polarized radiances for each of the 12 error sources. The solar zenith angle is 0°. The labels M, Z and U correspond to measurement, vertical distribution, and surface reflection error, respectively.

Figures 4.30 – 4.39 show the angular fields of the total errors for the 15 test cases. The layout and color scale remain the same as previous plots of this format in order to facilitate direct comparison. At low optical depths it can be seen that the largest errors occur in the sunglint region for both the total and polarized radiances. It has already been shown that outside of the sunglint region, the primary sources of error are the aerosol model assumptions. It has also been discussed that these errors will tend to be magnified at increasing optical depths and at increased solar zenith angles.

The total intensities show the smallest error in the near backscatter direction, with the exception being for the case of an overhead sun where there is a non-negligible contribution to the errors from the sun glint. Recall that an area of strong signal was seen here as well. In general, the errors for the total intensities tend to be larger near the horizon where the optical path length is longer than near the zenith angle. These errors, along with modeling problems near the horizon mitigate the strong signal previously seen near the horizon.

The polarized intensity errors show a similar angular distribution to the total intensities. In the backscatter direction, however, they show complicated lobes of error around the solar direction. These are the consequence of the oscillations of the scattering matrix elements in the backscatter directions. There appears to be a numerical issue for the polarized radiance error at low optical depths associated with the sun glint. For example, at $\Theta_o = 60°$ and $\tau = 0.1$ there is a ring of error at all azimuth angles at the solar zenith elevation. This is a result of not using enough Fourier modes to recreate the surface reflection function accurately.

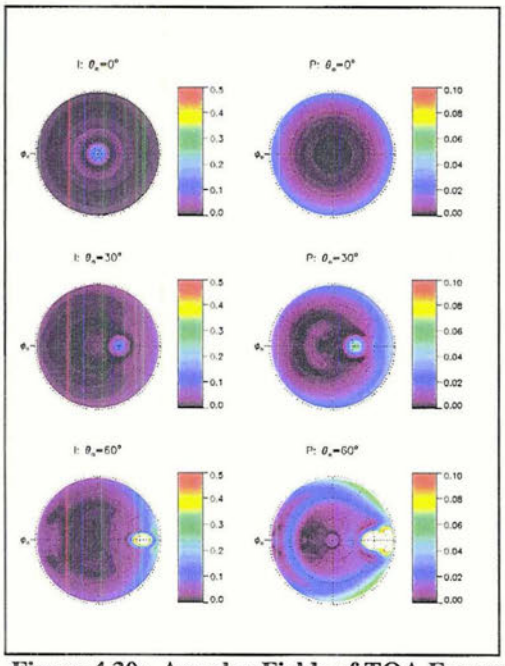

Figure 4.30: Angular Fields of TOA Errors For $\tau = 0.1$, $\lambda = 670.2$ nm

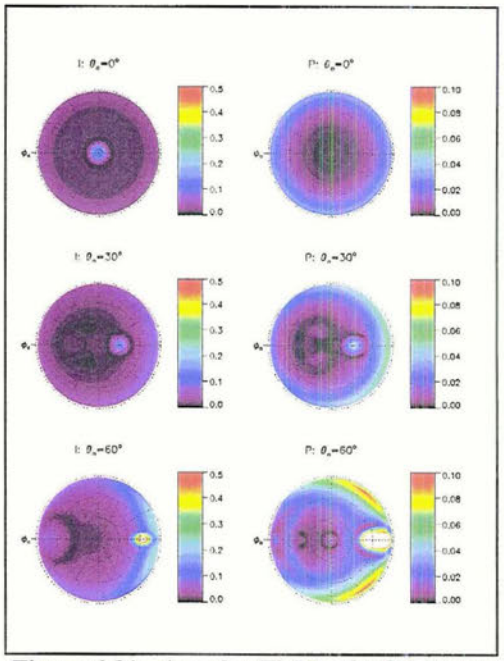

Figure 4.31: Angular Fields of TOA Errors For $\tau = 0.2$, $\lambda = 670.2$ nm

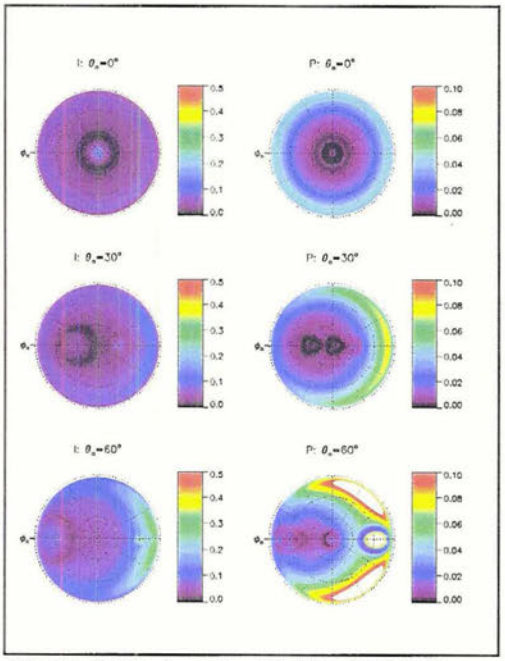

Figure 4.32: Angular Fields of TOA Errors For $\tau = 0.5$, $\lambda = 670.2$ nm

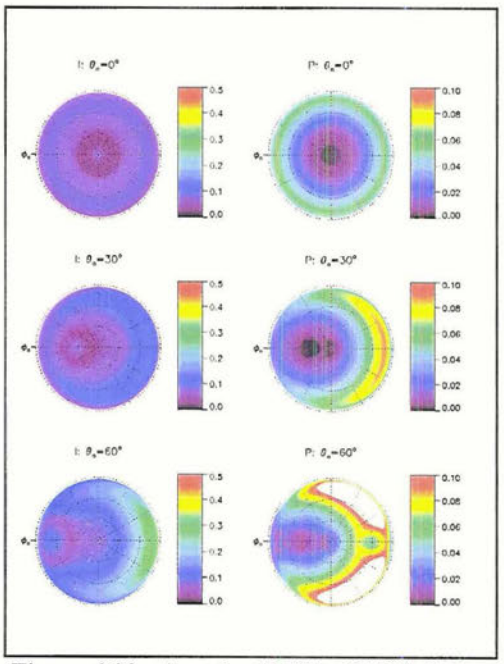

Figure 4.33: Angular Fields of TOA Errors For $\tau = 1.0$, $\lambda = 670.2$ nm

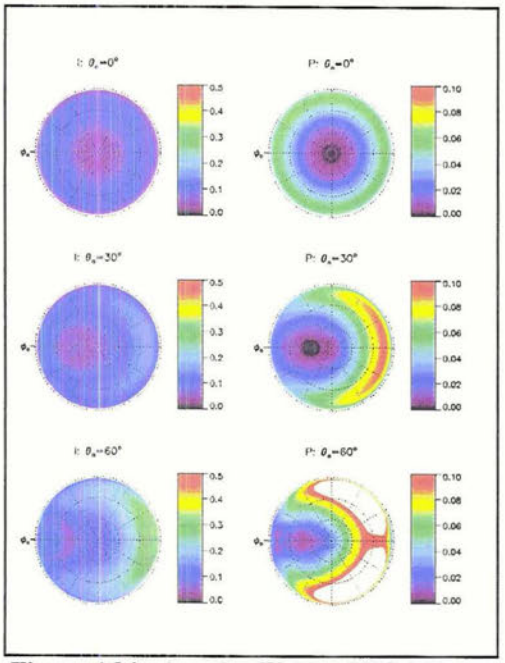

Figure 4.34: Angular Fields of TOA Errors For $\tau = 1.5$, $\lambda = 670.2$ nm

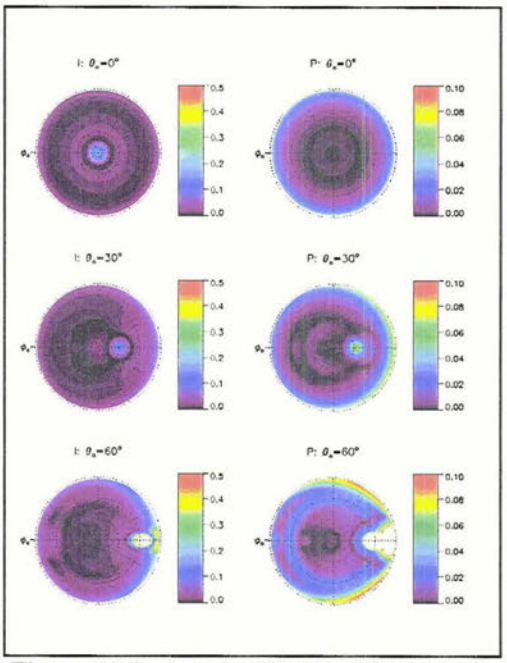

Figure 4.35: Angular Fields of TOA Errors For $\tau = 0.1$, $\lambda = 860.8$ nm

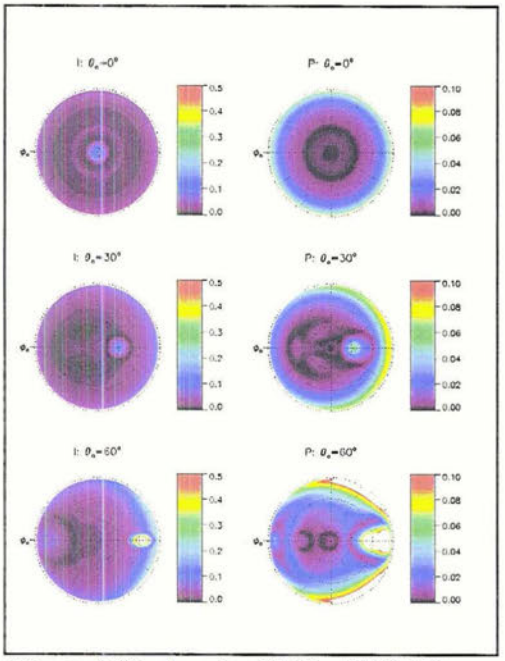

Figure 4.36: Angular Fields of TOA Errors For $\tau = 0.2$, $\lambda = 860.8$ nm

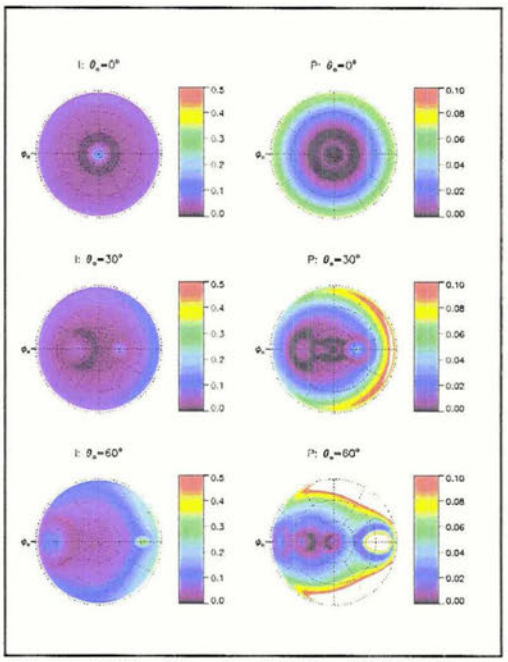

Figure 4.37: Angular Fields of TOA Errors For $\tau = 0.5$, $\lambda = 860.8$ nm

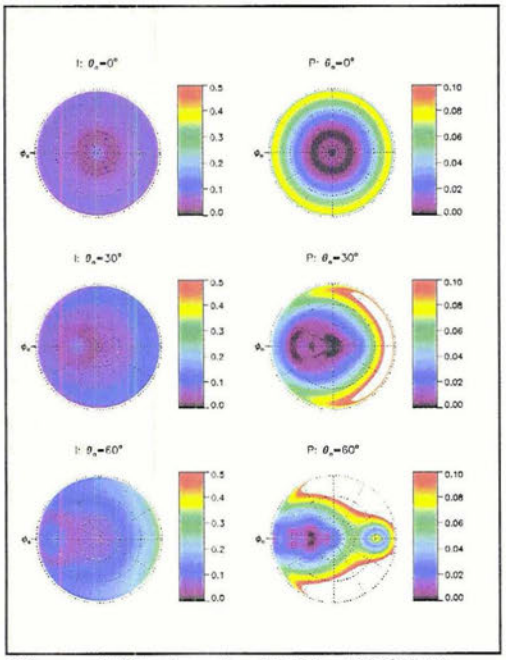

Figure 4.38: Angular Fields of TOA Errors For $\tau = 1.0$, $\lambda = 860.8$ nm

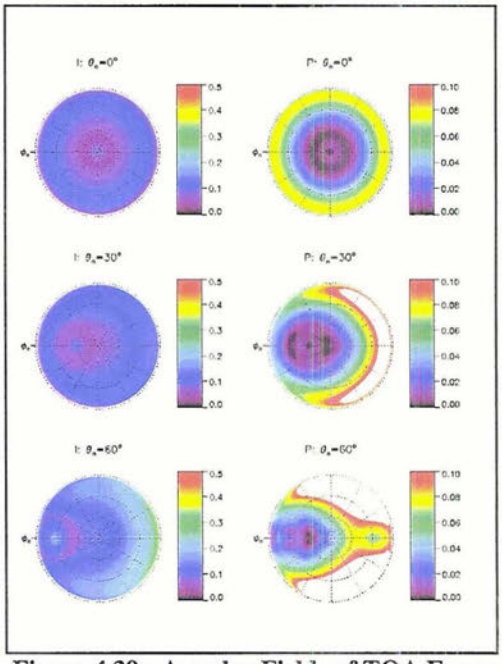

Figure 4.39: Angular Fields of TOA Errors For $\tau = 1.5$, $\lambda = 860.8$ nm

4.3.5 Signal to Noise Ratio

The fundamental quantity that defines the physics of any retrieval problem is the Signal to Noise Ratio (SNR), L'Ecuyer (2005). The SNR is the ratio of the Sensitivity of the measurements to the retrieval parameter to the noise in that measurement. The SNR is defined

$$SNR_{I,P} = \frac{d(I,P)/d\tau}{\varepsilon_{I,P}} \tag{4.7}$$

An SNR less than unity implies that the retrieval could be determined entirely by noise whereas an SNR greater than unity implies that a measurement can see through the noise and will thus improve our knowledge of the state.

The angular averages of the SNR are shown in Figure 4.40. The total radiances are on the top row and the polarized radiances are on the bottom row. Note that the Color scale for the total radiances is three times that for the polarized radiances. The average SNR decreases with optical depth. The greater SNR's at low optical depth follow straightforwardly from the fact that

signal increases while noise decreases at low optical depth for all solar zenith angles. The dependence on solar zenith angle is more complex. At low AOD's the increased signal with increasing solar zenith angle dominates the increase in the noise. As AOD increases, this pattern reverses as the single scatter approximation becomes less valid. Multiple scattering at large AOD and solar zenith angle will tend to diminish signal and amplify noise.

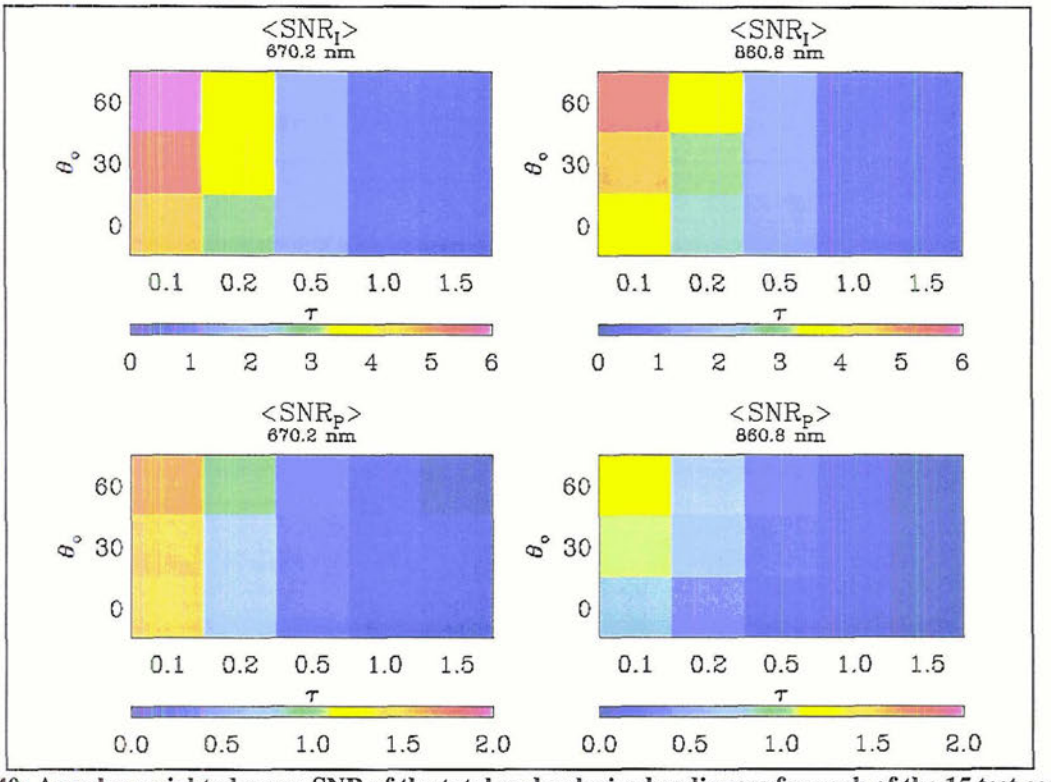

Figure 4.40: Angular weighted mean SNR of the total and polarized radiances for each of the 15 test cases.

It is evident that the average SNR is consistently greater in the total intensities than it is for the polarized intensities. In fact the averaged SNR for the total intensities is greater than or near one for all but the highest optical depths. Meanwhile the averaged SNR for the polarized intensities only exceeds unity for the lowest optical depth. This suggests that the majority of the information in an AOD retrieval utilizing both total and polarized radiances would come from the total intensities.

Angular fields of the SNR are shown in Figures 4.41 – 4.50. As it should now be expected, the angular structure is similar at both wavelengths. As SNR is the ratio of two quantities with complicated angular patterns, the fields shown in these figures often have very complex angular structure. Geometries in which the SNR is large are those in which measurements contain the most information and a retrieval will perform best.

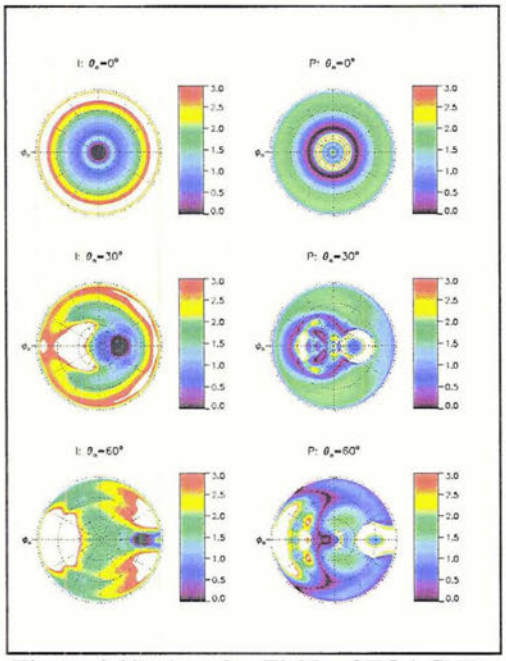

Figure 4.41: Angular Fields of TOA SNR For $\tau = 0.1$, $\lambda = 670.2$ nm

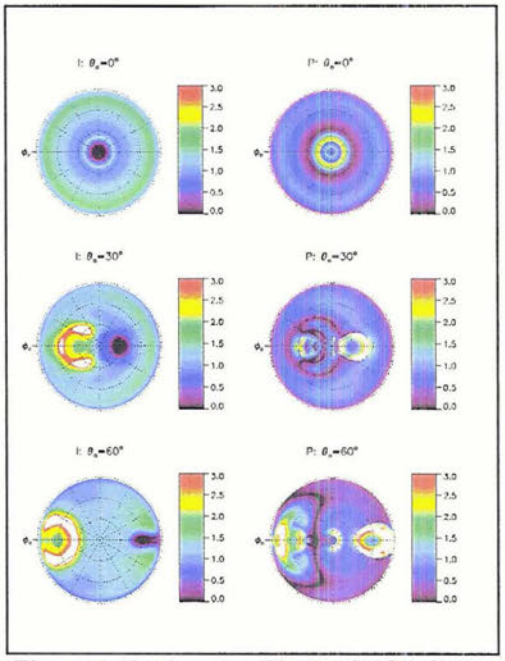

Figure 4.42: Angular Fields of TOA SNR For $\tau = 0.2$, $\lambda = 670.2$ nm

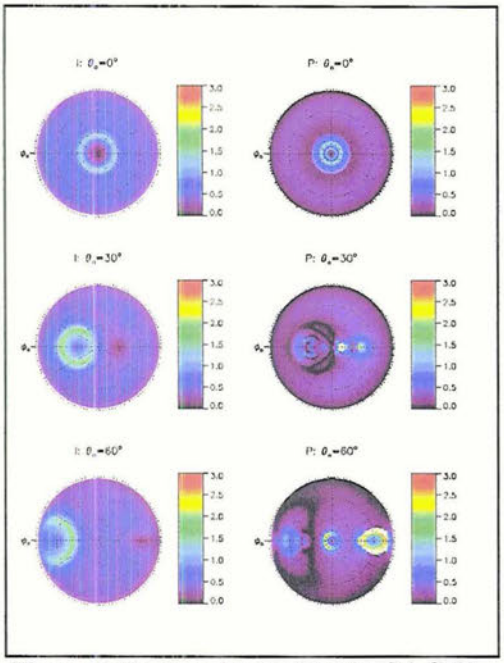

Figure 4.43: Angular Fields of TOA SNR
For $\tau = 0.5$, $\lambda = 670.2$ nm

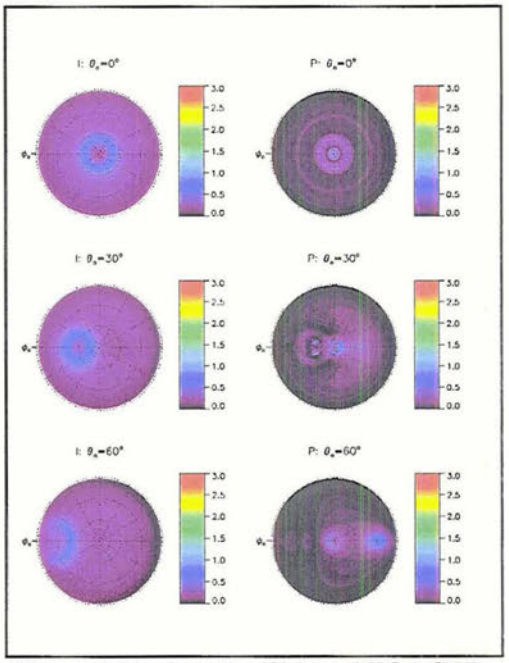

Figure 4.44: Angular Fields of TOA SNR
For $\tau = 1.0$, $\lambda = 670.2$ nm

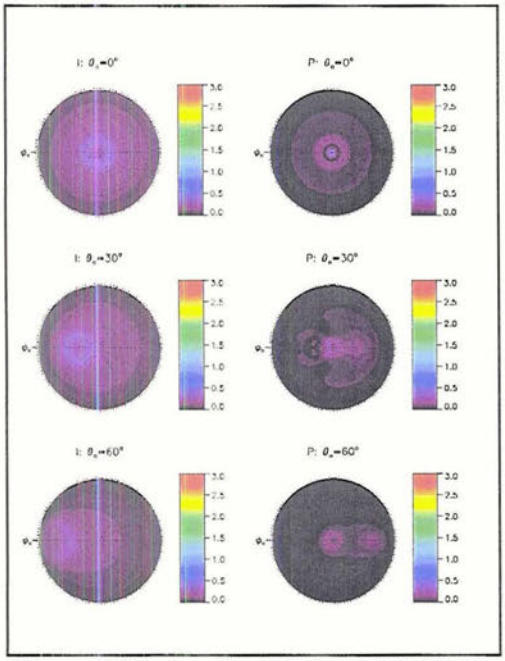

Figure 4.45: Angular Fields of TOA SNR
For $\tau = 1.5$, $\lambda = 670.2$ nm

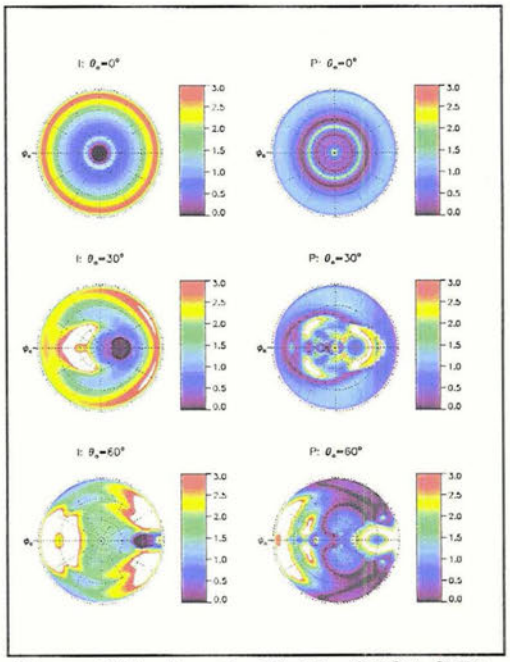

Figure 4.46: Angular Fields of TOA SNR
For $\tau = 0.1$, $\lambda = 860.8$ nm

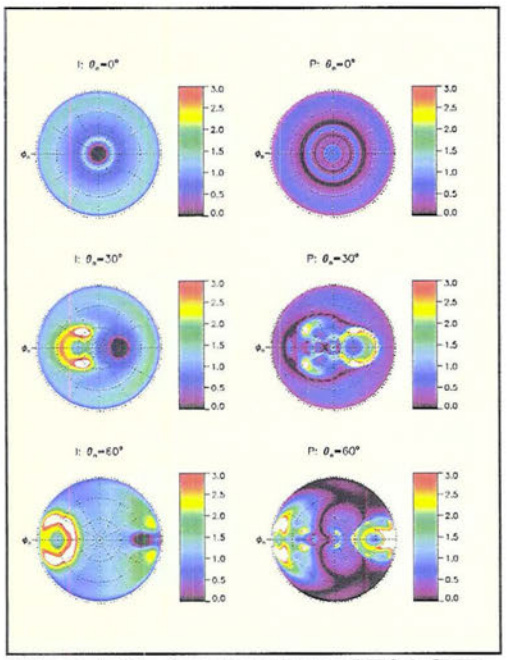

Figure 4.47: Angular Fields of TOA SNR
For $\tau = 0.2$, $\lambda = 860.8$ nm

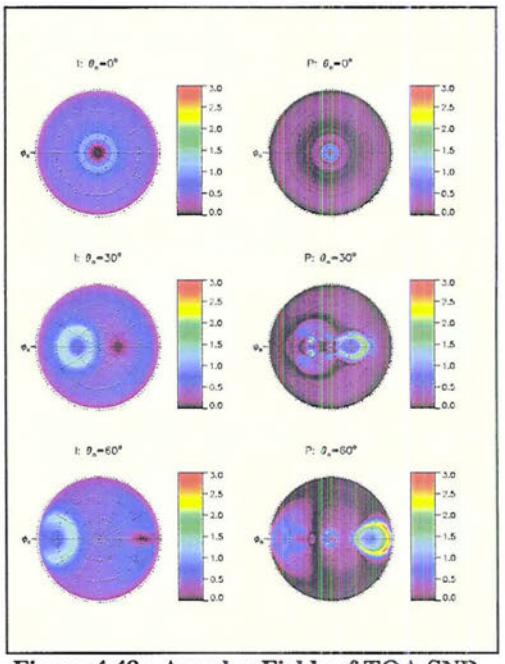

Figure 4.48: Angular Fields of TOA SNR
For $\tau = 0.5$, $\lambda = 860.8$ nm

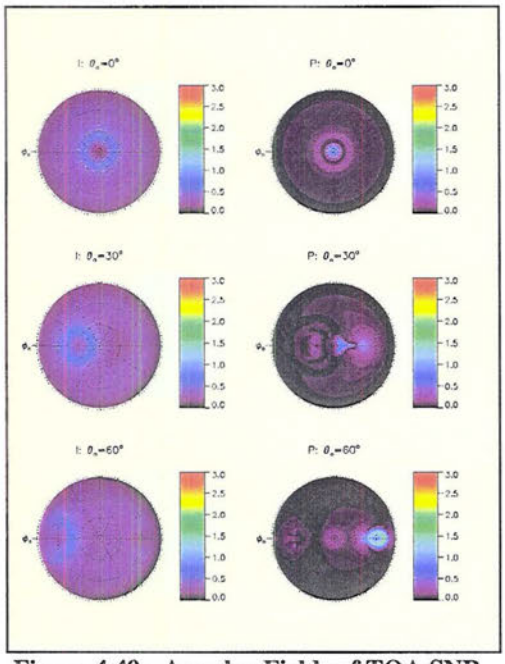

Figure 4.49: Angular Fields of TOA SNR
For $\tau = 1.0$, $\lambda = 860.8$ nm

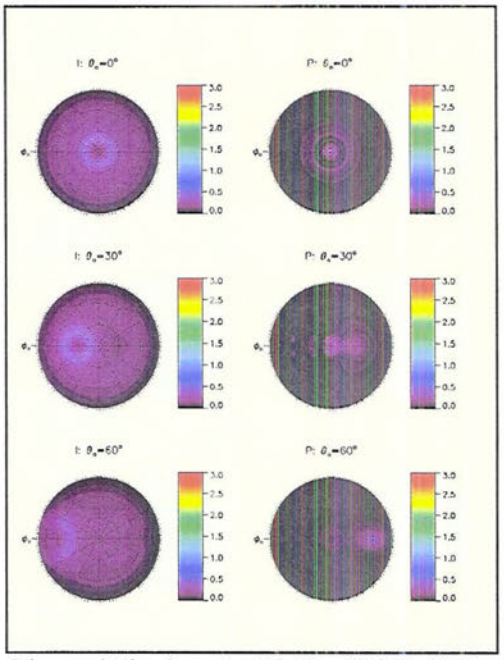

Figure 4.50: Angular Fields of TOA SNR
For $\tau = 1.5$, $\lambda = 860.8$ nm

The angular patterns for the total intensities are much simpler than those of the polarized intensities. These fields show what we would expect based on the maps of sensitivity and noise already discussed. There exists an SNR minimum in the sun glint at low optical depths resulting from the large noise at these angles for all plots. It is seen that for low optical depths there are large areas in which the SNR is significantly above unity. The region of largest SNR tends to exist in an annulus around the backscatter angle. There also exists large areas of high SNR near the horizon where the increase in signal outpaces the increased noise. Unfortunately, these areas are of little practical utility as POLDER makes no measurements beyond 75° zenith angle. Also, these angles are most susceptible to errors due to 3D effects, which have not been considered here.

For all of the test cases the SNR appears larger for the total radiance as opposed to the polarized radiance, with the exception of isolated pockets near the backscatter and glint angles. As with all of the maps previously discussed the angular patterns of the polarized intensities are less smooth than those of the total intensities. The patterns are similar to what has been seen previously. A low SNR exist in the sun glint at low optical depths. As with the total intensity, there exist areas of high SNR near the backscatter direction. Unlike the total intensity, there is an area of high SNR surrounding the sun glint. In this region the angular area of the signal in the sun glint region is larger than the angular area associated with the errors.

4.3.6 Sensitivity Study Conclusions

The previous four sub-sections have outlined the full results of the sensitivity study. The results of this study can be condensed into several main conclusions. The SNR is generally larger for the total intensities than it is for the polarized intensities. This SNR tends to decrease

with optical depth. This is primarily a result of the large sensitivities at low aerosol optical depths. It is concluded then that consideration of the scene dependence of the problem is critical in the development of an AOD retrieval.

A multi-angular retrieval is really subject to the specific viewing geometries of the measurements. Therefore, considering the same atmospheric state, two retrievals with different viewing geometries will be subject to different sensitivities and errors and will subsequently behave differently. Identifying favorable viewing geometries is key in the development of an observing system. The SNR maps shown in Figures 4.41 – 4.50 offer a method of analyzing a multi-angular AOD retrieval algorithm.

Based on the significantly larger SNR for the total intensities than for the polarized intensities, it is suggested that a multi-angular aerosol optical depth retrieval could utilize only the angular total intensity measurements. The benefits of neglecting the polarized information are a significant savings in computational expense. The two-channel AOD retrieval could be used to develop an improved aerosol model. A retrieval of a vector of some of the more fundamental quantities in the aerosol model could then be performed in a second step of the retrieval. This second step retrieval could then utilize the angular polarization information. A benefit of attempting to retrieve the more fundamental quantities is that a parameter in the retrieval vector no longer needs to be considered as a source of error. This acts to beat down the sources of error. It is suggested that an attempt is made to retrieve information about the ratio of the number concentrations, γ, as this is the largest single source of error for both the total and polarized intensities. It is also suggest that an attempt is made to avoid the sun glint angles, as the sun glint is a major source of error.

CHAPTER 5

A TWO CHANNEL AEROSOL OPTICAL DEPTH RETRIEVAL

5.1 Introduction

The optimal estimation framework has been used to develop a two-channel aerosol optical depth retrieval. The method is applicable to multi-angular intensity measurements such as those of POLDER. Based on the results of the sensitivity analysis of Chapter 4, it was decided to use only the total intensity and not the polarization information in order to retrieve AOD. Ignoring the polarization information results in a significant computational savings by limiting the size of the radiative transfer problem which must be solved. This is not unprecedented, as the POLDER operational retrieval algorithm, in its first step, uses intensity measurements only to retrieve the AOD's and calculate an Angstrom coefficient, Deuze et al. (2000). The retrieval performance is analyzed using synthetic data. Several different sources of bias are considered and discussed. Finally, the retrieval is applied to a small sample of POLDER II data.

5.2 Retrieval Theory

The retrieval theory begins with a statement of our understanding of the physics

which connects the measurements to the atmospheric quantity of interest. Equation 4.5 expresses this relationship and will be repeated here for clarity

$$y = F(x,b) + \delta \tag{5.1}$$

Here y is a vector of measurements, F is the forward model, x is a vector of length two consisting of the optical depths at the two channels, b is a vector of forward model assumptions and δ is a measurement uncertainty. In this case, the vector b is composed of all of the size distribution and optical parameters in the aerosol model. The task of the retrieval is to invert equation 5.1 in order to estimate x from y. Due to the complicated nature of the physics connecting the measurement space to the state space this is not generally possible in a straightforward mathematical manner. The method of optimal estimation is to invoke Bayes' theorem and solve the problem under a statistical framework. The idea is, that given our a priori knowledge of the statistics of the state parameters along with the statistics of the measurement errors, we find an optimal solution, which represents the best estimate of the statistics of the current state. Assuming Gaussian statistics, Rodgers (2000) has shown that the maximum likely hood solution is the one which minimizes the cost function

$$\Phi = \left[F(x) - y\right]^T S_y \left[F(x) - y\right] + \left[x - x_a\right]^T S_a \left[x - x_a\right] \tag{5.2}$$

Here S_y is the measurement error covariance matrix, S_a is the a priori error covariance matrix and x_a is the a priori estimate of the state. The cost function given in Equation 5.2 has a straightforward interpretation. It is simply the error weighted square difference between the measurements and the forward model plus the error weighted square difference between our estimate of the state and our a priori knowledge of the state. Rodgers has shown further that the maximum likelihood solution found by minimizing equation 5.2 is also the minimum variance a

posteriori solution. Therefore, the a posteriori solution found through this method is the most probable and has the least scatter.

Linearizing the forward model about the current state, the cost function can be minimized using Newton's method. This leads to the following iterative solution for the state vector

$$x_{i+1} = x_i + \left(S_a^{-1} + K_i^T S_y^{-1} K_i\right)^{-1}\left[K_i^T S_y^{-1}\left(y - F(x_i)\right) - S_a^{-1}\left(x_i - x_a\right)\right] \tag{5.3}$$

Here K is the matrix of derivatives of the linearized forward model with respect to the state parameters

$$K = \frac{\partial F}{\partial x} \tag{5.4}$$

Under the Bayesian optimal estimation framework, the retrieval product is not one answer but rather a PDF of the a posteriori knowledge of the state. The convergent value of the state vector is simply the most likely estimate of the state of the atmosphere. The envelope which describes the distribution of other possible solutions is given by the a posterior error covariance matrix

$$S_x = \left(K^T S_y^{-1} K + S_a^{-1}\right)^{-1} \tag{5.5}$$

The diagonal elements of this matrix represent the variance in the solution and complete the Gaussian description of the retrieval. The convergence criterion for Equation 5.3 is given by

$$\left[x_{i+1} - x_i\right]^T S_x \left[x_{i+1} - x_i\right] << m \tag{5.6}$$

where m is the number of degrees of freedom in the state space, in this case 2, corresponding to the two optical depths.

5.3 Information Theory

An important element of the optimal estimation framework is that it provides a convenient framework for estimating the information that the measurements have contributed to

the knowledge of the state. Defining the averaging kernel matrix as

$$A = S_x K^T S_y^{-1} K \tag{5.7}$$

the iterative solution given by equation 5.3 may be written as

$$x_{i+1} = x_i + AK^{-1}\left[F(x) - y\right] + \left(I - A\right)\left[x_i - x_a\right] \tag{5.8}$$

In this way it can be seen that the solution is derived as a linear combination of the measurements and the a priori knowledge of the state. For an ideal retrieval, the A-matrix would be the identity matrix. This would imply that the answer was derived entirely from the measurements. Examining the structure of the A-matrix allows for a straightforward analysis of how much of the answer is being derived from the measurements as opposed to the a priori constraint.

A further diagnostic defined in Rodgers (2000), is the Shannon information content, *H*. The Shannon information, *s*, is defined as the entropy of the PDF of the system

$$s = \sum_i P_i \log_2 P_i \tag{5.9}$$

Here P_i is the probability of the system occupying the i'th state. The Shannon information content follows as the difference in the entropy in the system before and after the measurements.

$$H = s_1 - s_2 \tag{5.10}$$

Defined in this manner, the Shannon information content provides a measure of the amount of information about the state of the system added by the measurements to the a priori knowledge of the state. Rodgers (2000) further defines this quantity in terms of the a priori and a posteriori error covariance matrices as follows

$$H = \frac{1}{2}\log_2|S_a| - \frac{1}{2}\log_2|S_x|$$
$$H = -\frac{1}{2}\log_2\left|S_a S_x^{-1}\right| \tag{5.11}$$
$$H = -\frac{1}{2}\log_2|I - A|$$

The Shannon information content can be interpreted as a measuring stick. For any given retrieval with a value of H, 2^H states can be distinguished by the measurements relative to the a priori value.

In addition to the above diagnostics a chi squared test may be performed. Following Engelen and Stephens (1997), chi squared is calculated as

$$\chi^2 = \left[F(x) - y\right]^T S_y \left[F(x) - y\right] + \left[x - x_a\right]^T S_x \left[x - x_a\right] \tag{5.12}$$

Over many retrievals the distribution of chi squared should approximately follow a chi squared distribution with 2 degrees of freedom. On an individual retrieval level, it will differ significantly from 2 when either the retrieved value is a statistical outlier or when the retrieval is not well able to match the measurements. A reasonable chi squared will therefore be a function of the area of state space occupied by the retrieval value. For example, large chi squared values near the a priori value indicate that the measurements and forward model are not in agreement. This points to a poor a priori aerosol model assumption. At extreme values of optical depth, large chi squared values will be expected due to the nature of the measurement as a statistical outlier.

Two other diagnostics discussed by Rodgers (2000) are the degrees of freedom for signal and the degrees of freedom for noise. These diagnostics evaluate the number of degrees of freedom of a retrieval problem which are associated with signal as opposed to noise. They are, therefore, closely related to the signal to noise ratio defined in Chapter 4. It would be expected

that measurements with a high SNR would have a large number of degrees of freedom for signal while those with a low SNR would have a large number of degrees of freedom for noise. The degrees of freedom for signal and degrees of freedom for noise are defined as

$$\begin{aligned} d_s &= \mathrm{tr}(A) \\ d_n &= \mathrm{tr}(I - A) \end{aligned} \tag{5.13}$$

5.4 A Priori and Measurement Error Statistics

The first step in developing an optimal estimation retrieval is to define the error covariance matrices S_a and S_y. Defining S_a is generally simpler than defining S_y as the measurement errors are a function of the forward model assumptions. It has been found that AOD tends to follow a log normal distribution. Therefore, the log of optical depth will be normally distributed. A natural choice for the state parameter follows as $\ln\tau$. Roughly following Ignatov and Stowe's (2001) AVHRR AOD climatology, the a priori value of AOD at 670.2 nm is taken to be 0.15 with a standard deviation in both optical channels of 0.25. The square of this value fills the diagonal elements of the S_a matrix. Assuming a correlation of 0.8 between the two channels fills the off diagonal elements of the matrix. The error analysis of Chapter 4 is used to determine the diagonal elements of the S_y measurement error covariance matrix. The total errors, ε, from Chapter 4 are assumed to describe two standard deviations of normally distributed error. Therefore, the diagonal elements are found as $S_y = (\varepsilon/2)^2$. An assumption of uncorrelated errors leaves the off diagonal elements as zero. This is certainly a dubious assumption. Correlations should be expected both between the two wavelengths and at different viewing angles within each wavelength. Properly defining these error covariances remains a significant challenge.

5.5 Sensitivity in Logarithmic Space

In the previous section it was mentioned that the retrieved state parameter is $\ln\tau$ as opposed to τ. This was done in order to better fit the assumption of a priori Gaussian statistics. Performing the retrieval in log space changes the nature of the retrieval by altering the model sensitivity. The sensitivity in log space is given by

$$S = \frac{\partial I}{\partial(\ln\tau)} = \tau\frac{\partial I}{\partial\tau} \tag{5.14}$$

Therefore, the sensitivity is decreased for values of AOD below unity and increased above unity, in a linear manner. This has the effect of stretching out the sensitivity discussed in Chapter 4. Shown in Figure 5.1 are the model sensitivities in $\ln\tau$ space. Unlike the sensitivity in linear τ space, which decreases monotonically, the sensitivity in $\ln\tau$ space now has a peak. This can be seen by examining the θ_o = 60° total radiance sensitivities. At both wavelengths the peak sensitivity is now seen at an optical depth of one.

Making the switch from linear to log space has both benefits and weaknesses. A benefit is that the a priori statistical assumption of the optimal estimation framework is more rigorously fit. Another benefit is that large values of optical depth, those above one, will have increased model sensitivity and therefore suffer from less a priori bias. The switch also assures that a non-physical negative AOD cannot be retrieved. Despite these benefits, substantial weaknesses are introduced. The majority of aerosol optical depths are less than one. This means that most retrievals will suffer from a decrease in sensitivity and will subsequently be subject to a larger a priori constraint.

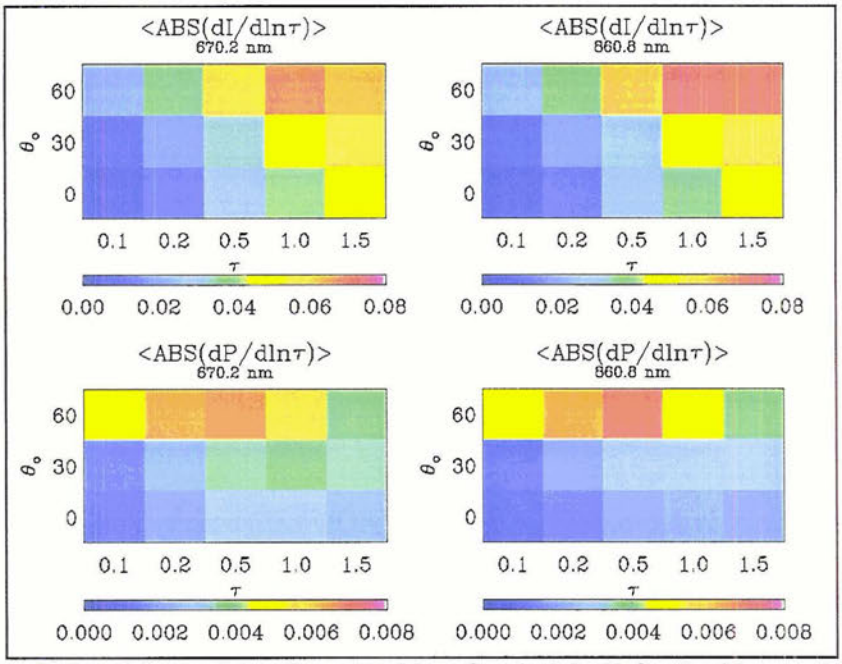

Figure 5.1: The Sensitivity of the model to the natural log of optical depth for the 15 example cases. The top row shows the derivative of the total radiance at both wavelengths while the bottom row shows the derivative of the polarized radiance.

5.6 Synthetic Retrievals

In order to develop an understanding of the retrieval, a handful of synthetic retrievals were performed. Three sets of POLDER-like viewing geometries were used. The geometries are shown in Figure 5.2 plotted over the SNR angular field for the case of $\tau = 0.5$ and $\theta_0 = 30°$ at a wavelength of 670.2 nm. Note that each case consists of 12 measurements. Combined with two wavelengths, this makes for a measurement vector of length 24. The three cases were chosen in order to determine how the angular dependent SNR would affect an AOD retrieval. Case #1 is entirely in the backscattering hemisphere in the high SNR region, Case #2 is in the anti-solar hemisphere in a low SNR region and Case #3 is in both hemispheres spanning an asymmetrical line of high and low SNR measurements.

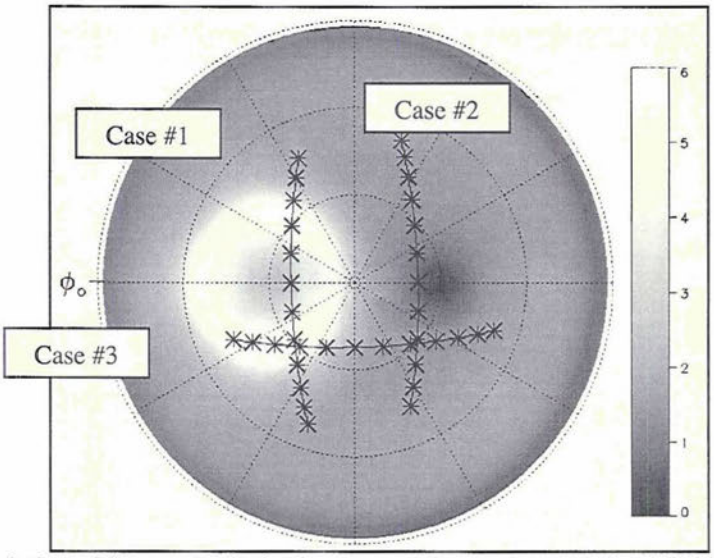

Figure 5.2: Visual depiction of three sets of viewing geometries used to test the AOD retrieval plotted over the SNR field at $\tau = 0.5$ and $\theta_o = 30°$ at 670.2 nm.

In the sections that follow, synthetic measurements will be used to perform several tests of the AOD retrieval. The measurements are created by first developing an aerosol model which describes the size distribution and optical properties of the aerosol. Radiative transfer calculations are then performed using these models to create TOA radiances, which are used as measurements in the AOD retrieval. Three aerosol models are considered. One is noise free meaning that the parameters are the same as those of the a priori aerosol model described in Chapter 4. The two other models perturb the large mode of the a priori aerosol model. One model amplifies the optical influence of this mode and the other damps its influence. The synthetic measurements created using these models will be referred to as noisy. The noise in the measurements manifests itself as changes to the phase function, the wavelength dependent single scatter albedo and the ratio of the two optical depths, $\Gamma = (\tau_{860.8}/(\tau_{670.2})$, relative to the assumed a priori aerosol model. The aerosol model parameters used to create the synthetic measurements are shown in Table 5.1. Synthetic measurements were created at three aerosol optical depths; 0.1, 0.2 and 0.5. The optical depths were modified while conserving Γ and SSA. This method of modifying optical depth assumes that optical depth changes as a result of changes in the total

number concentration of aerosol that do not alter the ratio of the number concentrations of the two individual modes, γ.

	Noise Free (Same As A Priori)		Large Mode Amplified		Large Mode Damped	
	Small Mode	Large Mode	Small Mode	Large Mode	Small Mode	Large Mode
N_o (m^{-3})	$1x10^9$	$1x10^6$	$1x10^9$	$5x10^6$	$1x10^9$	$5x10^5$
r_e (μm)	0.11	1.9	0.11	2.0	0.11	1.8
v_e (μm)	0.6	0.6	0.6	0.6	0.6	0.6
m_r	1.45	1.45	1.45	1.5	1.45	1.4
m_i	0.0035	0.0035	0.0035	0.0045	0.0035	0.0025

Table 5.1: The size distribution and optical parameters of the aerosol models used to create the synthetic measurements.

5.6.1 A Priori Bias

The first test performed uses noise free synthetic radiances created for optical depths of 0.1 and 0.5 at 670.2 nm. The viewing geometry considered is that of measurement set #1. The results of this retrieval are shown in Table 5.3. Because the radiances are created using the same forward model parameters as the a priori aerosol model the retrieval should be able to match the measurements exactly. The a priori constraint, however, prevents the retrieval from reaching the exact optical depths. This is seen in the bias of the retrieved optical depths towards the a priori value. The bias can more easily be seen in Figure 5.3, which shows the PDF's of the a priori state along with the a posteriori states of the two retrievals.

	$\tau = 0.1$		$\tau = 0.5$	
	$\lambda = 670.2$	$\lambda = 860.8$	$\lambda = 670.2$	$\lambda = 860.8$
Retrieved τ_λ	0.1041	0.0909	0.4606	0.3975
S_x	0.0086	0.0088	0.0064	0.0074
Bias	0.0041	0.0039	-0.0394	-0.0376
A-matrix	0.7062	0.6970	0.7734	0.7277
H	2.1706		2.4899	
χ^2	2.6145		23.8653	

Table 5.3: Retrieval results and diagnostics for the a priori bias test. The values for S_x and A are the diagonal elements of the 2x2 matrices.

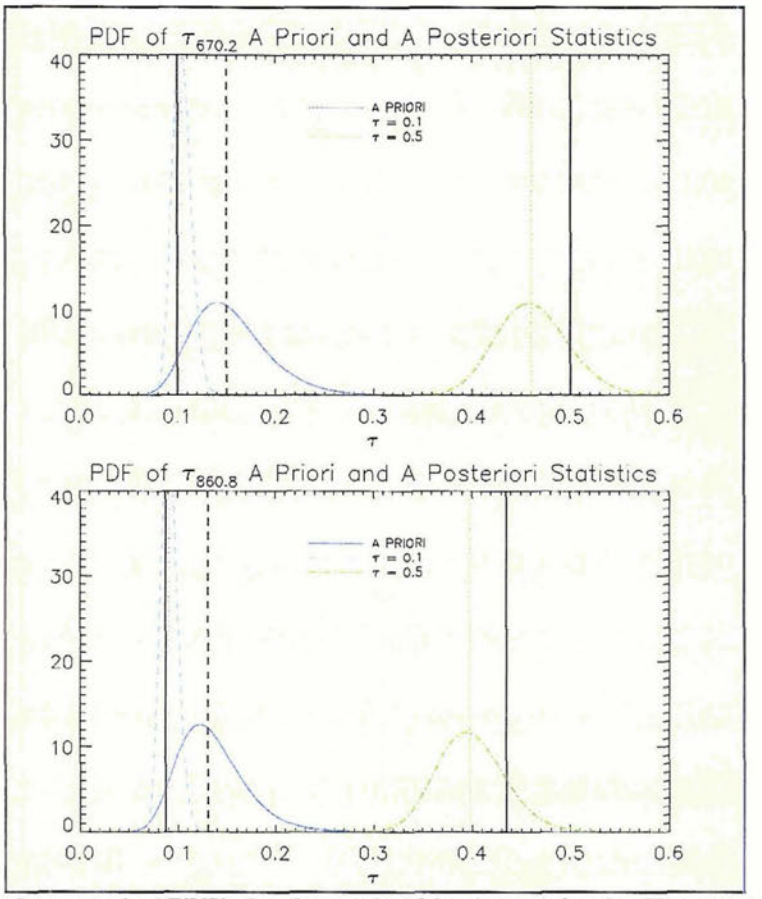

Figure 5.3: A priori and a posteriori PDF's for the a priori bias test retrievals. The top panel shows the 670.2 nm results while the bottom panel shows 860.8 nm. The dashed vertical lines represent the a priori value. The solid vertical lines represent the true atmospheric state used to create the synthetic measurements. The dotted vertical lines represent the retrieved optical depth values.

It is clear that both retrievals are biased towards the a priori value. The $\tau = 0.1$ retrieval is biased substantially less than the $\tau = 0.5$ retrieval because it is closer to the a priori value and subsequently the a priori did not attempt to constrain it as strongly. A priori bias is a quite general feature of an optimal estimation retrieval. For the case of a log normal distribution of optical depths, there will be many retrievals of low optical depths with a small high bias and far fewer retrievals of high optical depths with larger low biases. In a statistical sense these biases should cancel over many retrievals. It should also be mentioned that the retrieval product is a PDF, not an individual answer. Therefore, the correct PDF of the average of many retrievals can be constructed by averaging all of the retrieved PDF's.

Visual inspection of Figure 5.3 immediately points to the greatly increased information as to the state of the system a posteriori. The PDF of the low optical depth retrieval is extremely well peaked near the true AOD value. Meanwhile, the PDF of the high optical depth retrieval shows similar spread to the a priori statistics but it has been shifted very near to the true AOD.

A more quantitative analysis of how well the retrieval performed follows from inspection of the retrieval diagnostics given in Table 5.3. The A-Matrix values are larger for the $\tau = 0.5$ retrieval than for the $\tau = 0.1$ retrieval. This is a function of the larger signal at higher optical depths than at lower optical depths in log space. A further consequence is that the information content of measurements at large optical depth is greater than those at low optical depths. This means that the measurements at large AOD add more knowledge than do the measurements at low optical depths. The result is that the retrieval is better able to reach outliers at high optical depths, in the tail of the distribution, than it would in linear space. The chi squared test provides a further analysis of the retrieval. In this case the chi squared value is near a value of two for the $\tau = 0.1$ retrieval. Two, which is the number of degrees of freedom in this case, is the value which would be expect of a well behaved retrieval. the $\tau = 0.5$ retrieval has very large value of chi squared. Large chi squared values can result from two factors; An inability of the retrieval to match the measurements and retrievals of extreme values in the wings of the a priori PDF. The second mechanism is responsible in the case of this particular retrieval.

Analysis of any individual retrieval should involve all of the above diagnostics. Considering the $\tau = 0.5$ retrieval, large values of the A-matrix diagonals and the information confirm that the measurements added significantly to our knowledge of the system. However, the large chi squared will warn that the retrieval is most likely highly biased either by not matching the measurements well or by a significant a priori constraint. The opposite is true of

the low optical depth retrieval. Here the measurements added less information to our knowledge of the system and yet the low chi squared tells us that the retrieval is most likely not highly biased.

5.6.2 Effect of View Angle on A Priori Bias

The second test performed examines the effect of the viewing geometry on the retrieval. Noise free measurements were used to create the measurements for an AOD of 0.2. The retrieval was performed using the three different viewing geometries given by measurement sets #1, #2 and #3, shown in Figure 5.2. The retrieval results and diagnostics are listed in Table 5.4 while Figure 5.4 shows plots of the a priori PDF along with the PDF's for the three retrievals.

All three retrievals are biased low, which is a result of the a priori bias discussed in the previous section. Examining Figure 5.4, it is immediately clear that our information as to the state of the system is improved by all of the retrievals. All of the retrievals are shifted toward the true optical depth and all show increased peakedness relative to the a priori PDF.

	Case #1		Case #2		Case #3	
	$\lambda = 670.2$	$\lambda = 860.8$	$\lambda = 670.2$	$\lambda = 860.8$	$\lambda = 670.2$	$\lambda = 860.8$
Retrieved τ_λ	0.1957	0.1704	0.1805	0.1566	0.1958	0.1703
S_x	0.0068	0.0075	0.0257	0.0279	0.0066	0.0076
Bias	-0.0043	-0.0036	-0.0195	-0.0174	-0.0042	-0.0037
A-matrix	0.7569	0.7288	0.4321	0.3370	0.7664	0.7204
H	2.4336		0.8144		2.4411	
χ^2	1.2495		0.9974		1.2516	

Table 5.4: Retrieval results and diagnostics for the viewing angle bias test. The values for S_x and A are the diagonal elements of the 2x2 matrices.

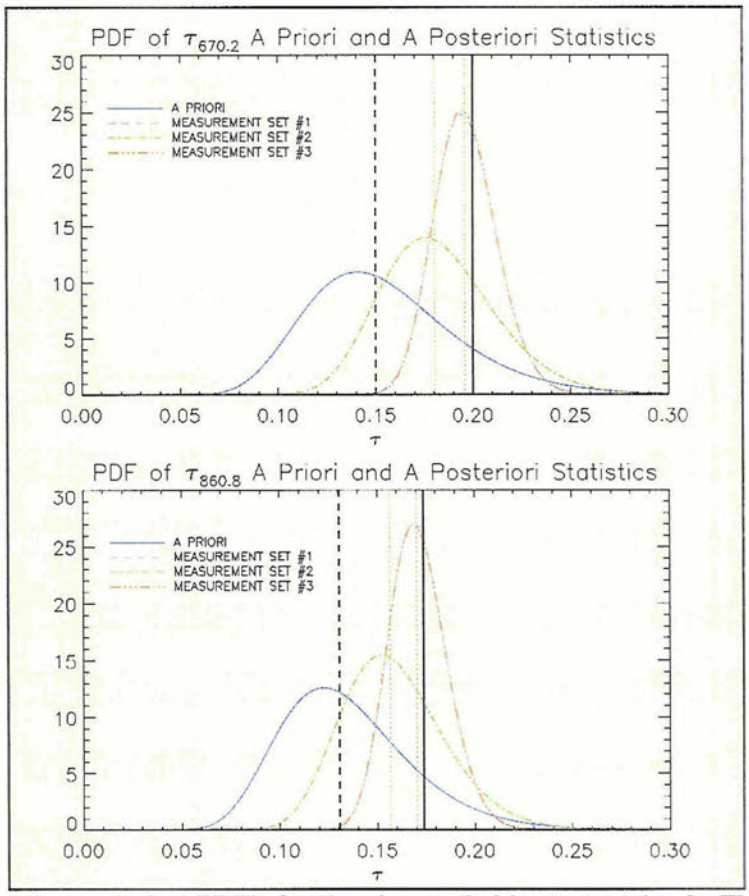

Figure 5.4: A priori and a posteriori PDF's for the view angle bias test retrieval. The top panel shows the 670.2 nm results while the bottom panel shows 860.8 nm. The dashed vertical lines represent the a priori value. The solid vertical lines represent the true atmospheric state used to create the synthetic measurements. The dotted vertical lines represent the retrieved optical depth values.

Despite the improved knowledge of the AOD provided by all of the retrievals, they are clearly not all equal. The bias and variance are much larger for the retrieval using the angles of measurement set #2. This manifests itself in the a posteriori PDF of measurement set #2, which shows larger spread and more bias than the other two retrievals. These are the angles in the anti solar hemisphere that show the lowest signal to noise ratio. The low SNR decreases the influence of the measurements on the retrieval. Subsequently, the measurements are less able to overcome the a priori constraint resulting in larger bias. The retrieval diagnostics confirm and quantify the previous statements. The low A-matrix diagonal values indicate that the majority of the information is coming from the a priori constraint as opposed to the measurements. Also, an

information content of less than one is found. This means that the retrieval cannot reliably distinguish two states relative to the a priori. The relatively low chi squared value for this case hints that the measurement error covariance is beginning to dominate the retrieval sensitivity. All of these poor diagnostics may be related directly back to the low SNR of the measurement angles.

Comparison of the retrievals for measurement sets #1 and #3 are interesting as well. The retrievals perform almost equally well as demonstrated by the retrieval diagnostics and the a posteriori PDF's. Retrieval #1 is comprised of angles with good to moderate SNR's while #3 is comprised of half favorable viewing geometries and half unfavorable. These results hint that most of the information needed for a quality retrieval is found in a few favorable viewing angles and that these favorable viewing angles can overcome any unfavorable viewing geometries in the measurement vector.

In order to test the hypothesis that the majority of the information is contained in a few favorable viewing geometries two additional retrievals were performed. Each of these retrievals uses half of the measurements given by measurement set #3. The first uses the angles with the most favorable SNR's while the latter uses the angles with the least favorable SNR's. These retrievals are compared with each other and with the retrieval that uses all of the measurements. The retrieval results are shown in Table 5.5 and plots of the a posteriori PDF's are shown in Figure 5.5.

The quantitative differences between the retrieval which uses all of the angles and that which uses only the favorable angles are very small. The all angles retrieval performs slightly better according to the diagnostics and the bias. Subsequently, the PDF of the all angles retrieval is slightly more peaked than the favorable angle retrieval. The unfavorable angle retrieval, on

the other hand, performs noticeably less well. The small values of the A-matrix diagonals, information content and chi squared all point to the majority of the answer being derived by the a priori constraint. The retrieval sensitivity, in this case, is simply not large enough to overcome the measurement error and force the answer towards the true optical depth. As a result this retrieval shows large bias relative to the other two retrievals.

The conclusion is that indeed the majority of the information is provided by the high SNR viewing geometries. Nonetheless, adding the low SNR measurements does help the retrieval, albeit slightly, to overcome a priori bias. It is now evident that in order for a retrieval to perform well, in terms of overcoming a priori bias, it needs only a handful of measurements at high SNR angles. In the case of this retrieval, which uses multiple viewing geometries at the same wavelength, there is no reason not to use all of the available viewing geometries, as all angles are provided by a single radiative transfer calculation. Having thoroughly accounted for measurement noise it is not worried that spurious information will be added by low SNR measurement angles. The exception to this statement may lie in the glint angles where accurate modeling is a problem.

	Favorable Angles		**Unfavorable Angles**		**All Angles**	
	$\lambda = 670.2$	**$\lambda = 860.8$**	**$\lambda = 670.2$**	**$\lambda = 860.8$**	**$\lambda = 670.2$**	**$\lambda = 860.8$**
Retrieved τ_λ	0.1953	0.1699	0.1711	0.1485	0.1958	0.1703
S_x	0.0072	0.0083	0.0374	0.0391	0.0066	0.0076
Bias	-0.0047	-0.0041	-0.0289	-0.0255	-0.0042	-0.0037
A-matrix	0.7487	0.7037	0.2865	0.2100	0.7664	0.7204
H	2.3271		0.4521		2.4411	
χ^2	1.2294		0.7411		1.2516	

Table 5.5: Retrieval results and diagnostics for noise free retrievals using different subsets of measurement set #3. Noise free measurements at an optical depth of 0.2 at 670.2 nm were used. The values for S_x and A are the diagonal elements of the 2x2 matrices.

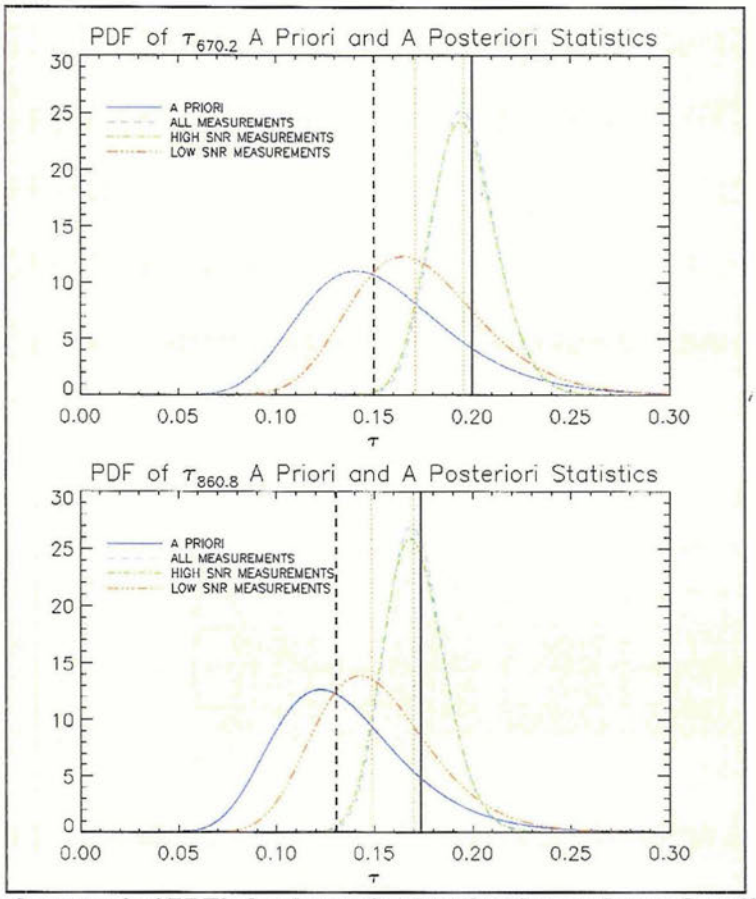

Figure 5.5: A priori and a posteriori PDF's for the retrieval testing the number and quality of the view angles. The top panel shows the 670.2 nm results while the bottom panel shows 860.8 nm. The dashed vertical lines represent the a priori value. The solid vertical lines represent the true atmospheric state used to create the synthetic measurements. The dotted vertical lines represent the retrieved optical depth values.

5.6.3 Measurement Noise Bias

Up to this point all of the measurements used have been noise free. This means that they were created using the same forward model assumptions as the a priori aerosol model. Now that an understanding of how the retrieval functions with noise free measurements has been established, it is tested using noisy measurements to determine the effect of the aerosol model assumptions. Three sets of measurements will be compared. One set of measurements was created by aerosol parameters which amplify the influence of the large mode of the aerosol size distribution relative to the small mode. A second set was created from parameters which damp the influence of the large mode. The third set is noise free. The aerosol model parameters which

are used to create these measurements are given in Table 5.1. Each of the three models listed in the table produces different optical properties. Altering the model changes the scattering phase function as well as both the wavelength dependent single scatter albedo and the ratio between the optical depths of the two channels, Γ. These properties are listed in Table 5.6. Synthetic measurements were created for an AOD of 0.2 while conserving the optical properties given in the Table.

	Γ	$\omega_{670.2}$	$\omega_{860.8}$
Large Mode Amplified	0.9975	0.8849	0.9025
Large Mode Damped	0.7797	0.9541	0.9541
A Priori Aerosol Model	0.8701	0.9285	0.9331

Table 5.6: The optical parameters of three aerosol models considered.

The retrieval results are shown in Table 5.7 for the viewing geometries defined by measurement set #3. The corresponding a posteriori PDF's are displayed in Figure 5.6. All of the retrievals are in a similar area of state space and use the same measurement error estimates. For this reason the SNR's at the final iteration value are similar for all three retrievals and there is little difference in the information content or A-matrix diagonals. In all three cases the answer has been derived mostly from the measurements. However, chi squared, is about three times as large for the two noisy retrievals as for the noise free retrieval. This is because the retrieval was not able to match the measurements as well when noise was added. This result suggests that chi squared can be used as a threshold to determine the quality of the forward model assumptions. This threshold would be a function of the area of state space of the retrieved AOD's as chi squared is also a function of the influence of the a priori constraint.

Note that the a posteriori PDF shows a significant low bias for the large mode amplified retrieval. The large mode damped retrieval, on the other hand, shows less bias than the noise

free retrieval. Remember that all of these retrievals are still subject to an a priori low bias as well. The additional bias encountered here is due to the discrepancies between the a priori aerosol model assumptions and the true aerosol model. In order to obtain a clearer picture of the physics driving this noise related bias two more retrievals were performed. The same retrievals as above were performed using measurement set #2. This set contains the noisiest viewing angles, with the lowest SNR's. As a result, the effects of the noise are amplified. The results of these retrievals are shown in Table 5.8 and the a posteriori PDF's are shown in Figure 5.7.

	Noise Free		Large Mode Amplified		Large Mode Damped	
	$\lambda = 670.2$	$\lambda = 860.8$	$\lambda = 670.2$	$\lambda = 860.8$	$\lambda = 670.2$	$\lambda = 860.8$
Retrieved τ_λ	0.1958	0.1703	0.1784	0.1718	0.1958	0.1578
S_x	0.0066	0.0076	0.0077	0.0077	0.0068	0.0086
Bias	-0.0042	-0.0037	-0.0216	-0.0277	-0.0042	-0.0019
A-matrix	0.7664	0.7204	0.7282	0.7273	0.7682	0.6853
H	2.4411		2.3325		2.3420	
χ^2	1.2516		3.9949		3.7745	

Table 5.7: Retrieval results and diagnostics for both noisy and noise free retrievals using measurement set #3. Measurements for an optical depth of 0.2 at 670.2 nm were used. The values for S_x and A are the diagonal elements of the 2x2 matrices.

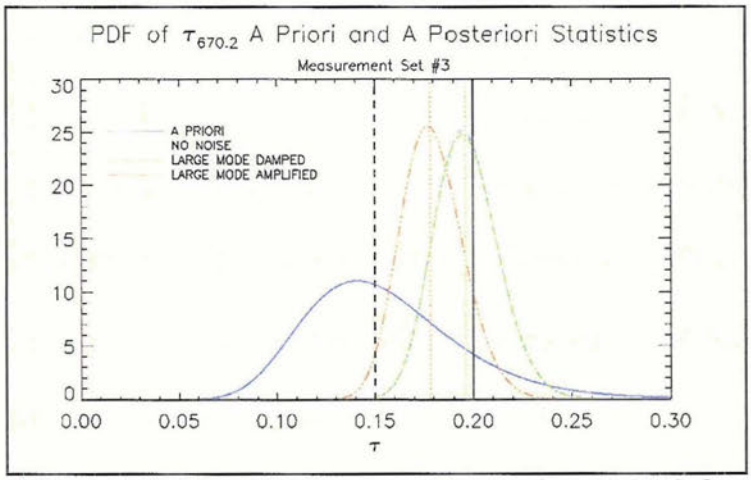

Figure 5.6: A priori and a posteriori PDF's for the noisy versus noise free retrievals for view angle set #3. Only the 670.2 nm results are shown. The dashed vertical lines represent the a priori value. The solid vertical lines represent the true atmospheric state used to create the synthetic measurements. The dotted vertical lines represent the retrieved optical depth values.

	Noise Free		Large Mode Amplified		Large Mode Damped	
	$\lambda = 670.2$	$\lambda = 860.8$	$\lambda = 670.2$	$\lambda = 860.8$	$\lambda = 670.2$	$\lambda = 860.8$
Retrieved τ_λ	0.1805	0.1566	0.1481	0.1325	0.2102	0.1767
S_x	0.0257	0.0279	0.0319	0.0338	0.0212	0.0239
Bias	-0.0195	-0.0174	-0.0519	-0.0670	-0.0102	-0.0208
A-matrix	0.4321	0.3370	0.3514	0.2688	0.4996	0.3834
H	0.8144		0.6035		1.0010	
χ^2	0.9974		0.5234		3.0427	

Table 5.8: Retrieval results and statistics for both noisy and noise free retrievals using measurement set #2. Measurements for an optical depth of 0.2 at 670.2 nm were used. The values for S_x and A are the diagonal elements of the 2x2 matrices.

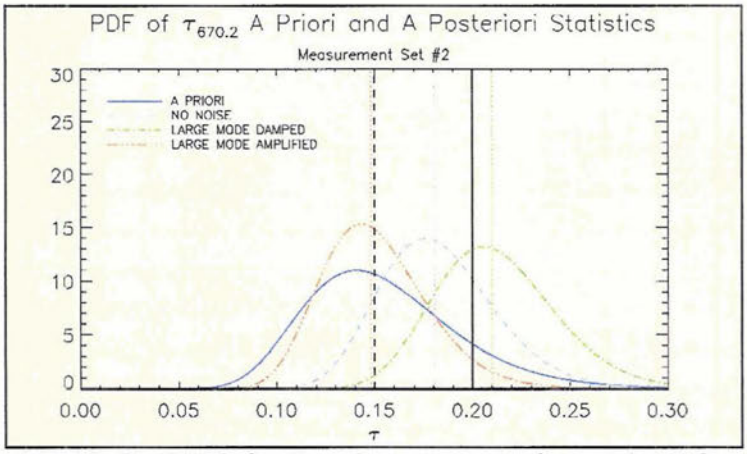

Figure 5.7: A priori and a posteriori PDF's for the noisy versus noise free retrievals for view angle set #2. Only the 670.2 nm results are shown. The dashed vertical lines represent the a priori value. The solid vertical lines represent the true atmospheric state used to create the synthetic measurements. The dotted vertical lines represent the retrieved optical depth values.

The focus here is on the bias created by the aerosol model assumptions. In this case, despite the low bias caused by the a priori constraint, the large mode damped retrieval is biased high relative to the truth. Meanwhile, the large mode amplified retrieval is biased low. This retrieval actually moved in the incorrect direction from the a priori value. The physical explanation for these biases follows from invoking the single scatter approximation. Under this assumption, the TOA radiance component resulting from aerosol scatter is given by Equation 4.4. The main point to notice in this equation is that the radiance is linearly related to both AOD and SSA. It has been shown in Table 5.6 that adding noise to the aerosol model alters the optical

properties. Specifically, it increases the true single scatter albedo in the large mode damped case and lowers it in the large mode amplified case. These single scatter albedo biases will have to be offset in a linear manner by a bias, of opposite sign, in the optical depth. This is exactly what is seen for these two retrievals. When the a priori single scatter albedo is biased low, as in the large mode damped case, the optical depth retrieval is biased high, whereas the opposite is true for the large mode amplified retrieval. It is expected that due to the fairly linear nature of the noise and the single scatter approximation, these biases will largely cancel.

Comparing Figure 5.6 to Figure 5.7, note how the noise related bias is substantially reduced by using measurements with high SNR values. This once again points to the utility of maximizing SNR in the development of an observing system. It has already been demonstrated that high SNR's decrease the a priori and view angle biases. Now, it is evident that large SNR is related to decreased bias related to forward model assumptions.

One final comment related to the retrieval results shown in Table 5.7 and 5.8 is that in all the noisy cases the retrieval is able to improve the estimate of the ratio of the two optical depths, Γ, relative to the a priori ratio. The true values of these parameters along with the retrieved values for both of the noisy retrievals are given in Table 5.9. The noise free retrievals begin the iteration with the correct ratio and they are seen to change only slightly. Both of the large mode damped retrievals push the ratio down towards the true value while the opposite is true of the large mode amplified. The tendency to retrieve an improved optical depth ratio allows for an a posteriori estimate of an improved aerosol model. The idea is to modify the a priori aerosol model parameters in such a way that they produce the retrieved ratio of the optical depths. The best method of doing this is beyond the scope of this thesis. The difficulty in modifying the aerosol model is that there is non-uniqueness in the problem. Any of the aerosol model

parameters could be modified in order to obtain the retrieved AOD ratio. The parameter with the largest dynamic range is the ratio of the number concentration of the two modes of the aerosol size distribution, γ. It would therefore be convenient to modify this parameter to match the ratio of the two optical depths.

	Γ_{TRUE}	$\Gamma_{FAVORABLE}$	$\Gamma_{UNFAVORABLE}$
Large Mode Amplified	0.9975	0.9630	0.8947
Large Mode Damped	0.7797	0.8059	0.8406
Noise Free	0.8701	0.8698	0.8676

Table 5.9: The true ratio of the optical depths for each of the three aerosol models is given in the first column. The second and third columns show the retrieved ratios for the retrievals using measurement sets #3 and #2 respectively.

5.7 Retrievals Using POLDER II data

In order to confirm that the retrieval assumptions and error estimates are reasonable, the retrieval is now applied to a small subset of POLDER II radiance data. Data from the boxed region in Figure 5.8 were used. This orbit corresponds to the first day in July, 2003. The comprehensive error estimates of Chapter 4 are limited to only three discrete solar zenith angles. These error estimates are highly sensitive to the solar zenith angle. Therefore, the data was first filtered to eliminate all measurements in which the solar zenith angle differed from 30^0 by more than one degree. A series of subsequent filters screened for cloud and land contamination. This process left 328 pixels for analysis. The retrieval was then applied to this data.

Retrieval results are shown in Figure 5.9. The bins show the most probable retrieved value of AOD. The continuous function plotted over the binned values show the a priori PDF. The dots represent the A matrix diagonals of the individual retrievals plotted as a function of optical depth.

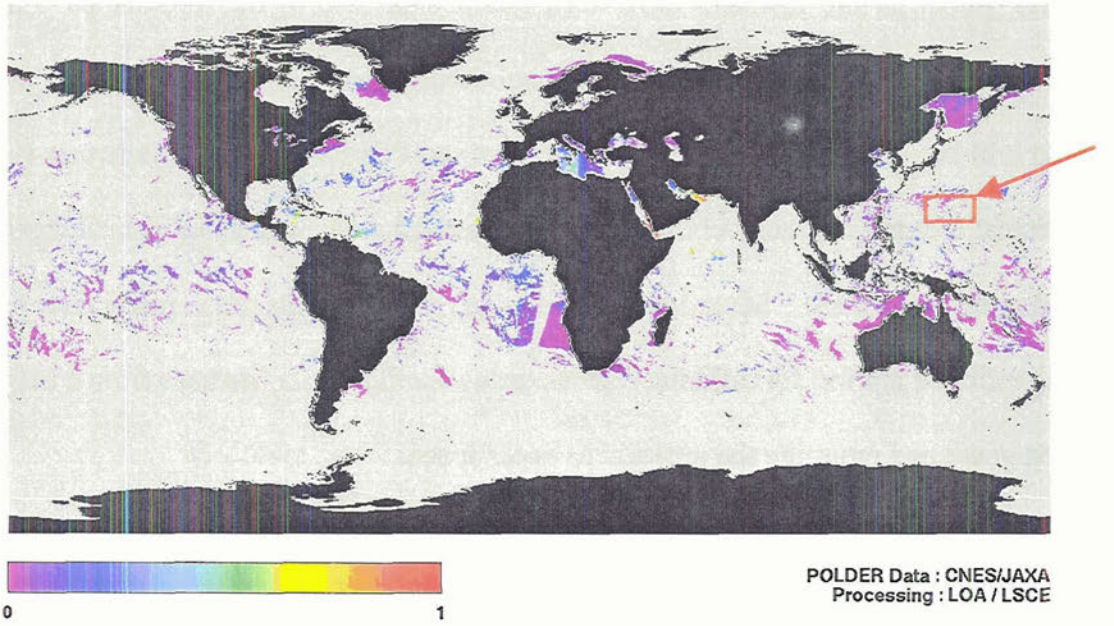

Figure 5.8: daily synthesis of the POLDER aerosol optical depth product at 865 nm for the date of July 1st, 2003. The boxed region corresponds to the radiance data used in the optimal estimation retrieval.

It is immediately evident that this is a relatively clean atmospheric scene. The majority of the optical depths are at the low end of the a priori distribution. Nonetheless there are some larger optical depths up to about 0.6. It is encouraging to see that the distribution of optical depth at both channels, even for this relatively small sample, appears to be log normally distributed. Qualitative comparison with the map of the POLDER optical depths at 865 nm show that the retrieval is generally in good agreement. The A matrix diagonals are however quite low for the retrievals at low optical depth. The nearly monotonic increase in the A-matrix with optical depth is a function of the increasing signal with AOD in this area of $\ln\tau$ space. This indicates that the measurements would like to move the retrieval lower for the lowest optical depth bins.

To test this hypothesis the retrieval was rerun with a doubled a priori error covariance. These results are shown in Figure 5.10. The retrieval results are fairly similar. The notable exception is that at the smallest optical depths a number of retrievals have moved down one bin.

The A matrix values at the low end have been bumped up due to the diminished a priori constraint. It remains to be seen what the proper solution to the problem of low signal at low optical depth will be. Examination of the map of retrieved POLDER AOD's, shown in Figure 5.8, indicates that a significant number of pixels are very clean cases with small optical depths so this issue must be confronted. Some possible solutions are to inflate the a priori covariance matrix, using different a priori for different regions, using ancillary data (perhaps from a LIDAR) to set the first guess and returning the retrieval to linear space.

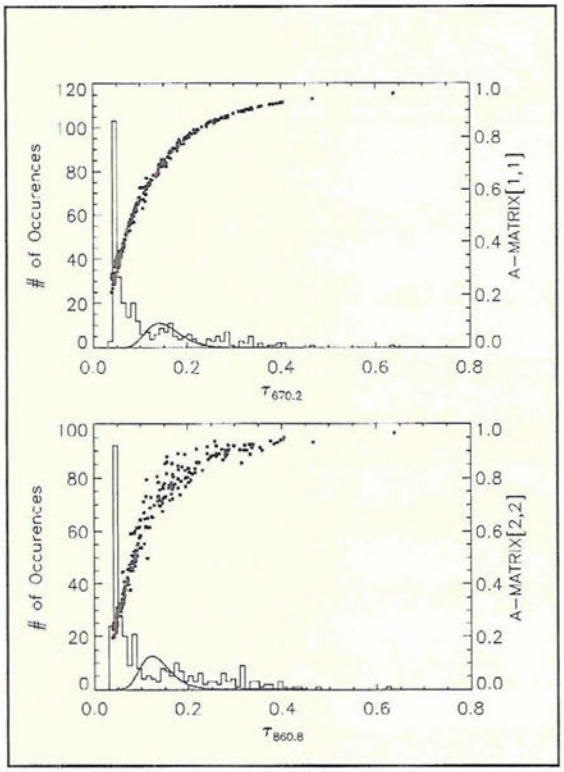

Figure 5.9: Retrieved AOD's at both wavelengths are binned for the unmodified a priori covariance retrieval. The continuous function is the a priori error PDF while the scattered points are the A matrix diagonals for the individual retrievals.

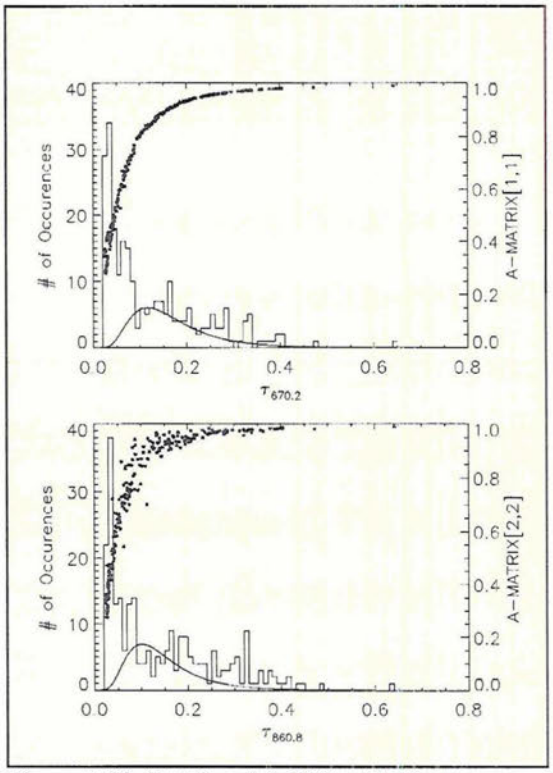

Figure 5.10: Retrieved AOD's at both wavelengths are binned for the doubled a priori covariance retrieval. The continuous function is the a priori error PDF while the scattered points are the A matrix diagonals for the individual retrievals.

CHAPTER 6

CONCLUSIONS AND FUTURE WORK

This thesis involved the development of several atmospheric radiative transfer tools as well as an application of these tools towards the remote sensing of aerosol properties from space. The tools developed include the computation of aerosol and molecular scattering and absorption properties along with a polarized radiative transfer model. These tools were applied towards a comprehensive sensitivity analysis and error characterization of the forward model to aerosol optical depth. This analysis was subsequently used to develop a two-channel aerosol optical depth retrieval based upon the optimal estimation framework. This chapter reviews the major results of the Thesis as well as offer several suggestions for the extension of this work.

6.1 Summary of the Calculation of Extinction Properties

The scattering and absorption properties for both the molecular atmosphere and aerosols have been modeled using standard techniques. Molecular absorption has been modeled using the HITRAN database while molecular scattering properties have been calculated according to the Rayleigh approximation. Mie theory was used to model the optical properties of atmospheric

aerosols. This implicitly assumes spherical aerosol particles. The fully polarized scattering matrix is expanded in a series of generalized spherical functions.

6.2 Summary of Forward Model

A fully polarized, doubling/adding radiative transfer model was developed. The model permits both Gaussian and Lobatto quadrature schemes. A Stokes parameter of variable length may be solved, allowing for a computational savings. Multiple homogenous atmospheric layers are allowed and the layer interface boundary conditions are matched using the interaction principle. Two lower reflecting surface boundary conditions are currently modeled. The first is a simple Lambertian surface. The second is a rough ocean reflecting surface which is a function of wind speed. The model uses several symmetry relations in order to increase the efficiency of the calculations.

6.3 Summary of Sensitivity Analysis

An atmospheric aerosol model was developed which is representative of a clean maritime environment. The aerosol model specifies a bimodal size distribution as well as optical parameters. As an initial step towards developing an aerosol retrieval, the sensitivity of the forward model to aerosol optical depth was analyzed for fifteen atmospheric scenes. These scenes included three solar zenith angles and five aerosol optical depths. The top of the atmosphere total and polarized radiances for each scene were modeled. Three quantities were then calculated for each atmospheric scene for the hemisphere of top of the atmosphere viewing angles. The first quantity calculated was the signal, defined as the derivative of the total and polarized radiance with respect to AOD. The second quantity calculated was the noise, which is

also referred to as the error. Twelve different sources of noise were considered. Each individual source of noise was calculated as the range of radiance as a function of the forward model assumptions. Finally, the signal to noise ratio was calculated as the ratio of the previous two quantities. The single scattering approximation was used to explain the physical basis for the observed phenomena. The highlights of the sensitivity analysis are outlined below.

- Both the total and polarized TOA radiances tend to increase with optical depth and with solar zenith angle.
- The average signal tends to increase with solar zenith angle and decrease with optical depth.
- Depending on the scene, the average signals were found to be anywhere from around ten percent to around three hundred percent of the average radiance.
- The largest sensitivities were found in the sun glint, in the backscatter directions and at viewing angles near the horizon.
- The average total error tends to increase with solar zenith angle and with optical depth.
- The average errors for the polarized radiances often exceed one hundred percent of the average polarized radiance value. The average total radiance value for the errors can be as high as fifty percent of the radiance value but are generally much lower in a fractional sense than the polarized errors.
- The largest single sources of error are the sun glint at low optical depths and the ratio of the number concentration of the two modes of the aerosol size distribution.
- The largest errors tend to be in the sun glint region and at large zenith angles.
- There tends to be a minimum in error in the backscatter region

- The average signal to noise ratio tends to increase with solar zenith angle and optical depth.
- The signal to noise ratio is generally about three times as large for the total as for the polarized radiances.
- The most consistent area of large signal to noise ratio tends to be in an annulus around the backscatter direction. There also exists large signal to noise ratio at large zenith angles. The polarized radiances show an area around the sun glint of large SNR.

There are two major conclusions of the sensitivity analysis. First, the majority of the information in deriving optical depth tends to come from the total radiance as opposed to the polarized radiance. Second, the TOA fields of signal to noise ratio show a significant viewing angle dependence. The largest SNR's tend to be in the backscatter direction while the lowest SNR's tend to be in the glint angles.

6.4 Summary of the Optical Depth Retrieval

A two-channel optimal estimation retrieval algorithm was developed utilizing multi-angular radiance measurements. Optimal estimation is a statistical framework based upon Bayes' theorem. The statistics of aerosol optical depth are log normal and therefore the retrieval was implemented in log space. This has the effect of modifying the model sensitivity, generally lowering it at small optical depths. The measurement error statistics were based upon the noise calculations used in the sensitivity analysis.

Several sources of retrieval biases were analyzed using synthetic measurements. These biases include a priori bias, viewing geometry bias and measurement noise bias. Finally, the algorithm was applied to a small set of POLDER data. The main results are outlined below.

- The optimal estimation algorithm introduces an a priori bias into the retrieved answer. This bias can significantly affect the retrieval of extreme values of optical depth in the wings of the a priori distribution.
- It is expected that a priori bias will cancel in an average sense over many retrievals.
- It is also expected that the true PDF of retrieved AOD's can be reconstructed by averaging the retrieved PDF's as opposed to the retrieved values.
- The signal to noise ratio of the particular viewing geometry of the measurements significantly affects the retrieval. Viewing geometries with high signal to noise ratio tend to have much less bias than those with low signal to noise ratio.
- It was found that only a few of the twelve measurements angles need to have high signal to noise ratios in order to overcome this bias.
- Measurement noise introduced through incorrect aerosol model assumptions can bias the retrieved values.
- Due to the single scatter nature of the problem, the measurement noise tends to be fairly linear. It is therefore expected that averaging will be able to eliminate a large portion of this bias.
- The retrieval algorithm was applied to a small subset of POLDER II data. There appears to be qualitative agreement between the POLDER AOD product and the optimal estimation retrieval.

- Doubling the a priori error covariance elements allows the retrieval to reach lower optical depths for this dataset. Otherwise it is unable to reach low optical depths due to the small signal in log space.

6.5 Future Work

This Thesis was primarily an effort to develop the tools necessary in order to understand the physics of the aerosol retrieval problem. This is a necessary initial step in the development of a comprehensive aerosol retrieval. The eventual goal of this research is the development of a multi-sensor aerosol retrieval method. A list of necessary additions to the aerosol optical depth retrieval follows.

- Explore the low signal at low optical depth issue, further examining the effects of increasing the a priori covariance and returning to a linear space retrieval. Another possibility is to use ancillary data from CALIPSO to determine an a priori guess.
- Create look up table of measurement error covariance matrices at finely spaced solar zenith angles and optical depths.
- Correct for the small molecular absorption effects.
- Initialize surface wind speed from observations/reanalysis.
- Compare with large sampling of POLDER products to determine biases.
- Explore the addition of off diagonal elements to the measurement error covariance matrices.

In addition to polishing the functionality of the AOD retrieval a second step of the retrieval must be developed to retrieve the more fundamental parameters of the aerosol model using added information from the A-train constellation. This will necessitate the following steps

- Determine a method for defining an improved a posteriori aerosol model from the results of retrieval step #1. Modifying the ratio of the number concentration of the two modes of the size distribution to match the ratio of the retrieved wavelength dependent optical depths is the most likely candidate.
- Determine the ideal retrieval vector of size distribution and optical parameters using the information content approach.
- Develop the second step of the retrieval utilizing polarization information.
- Add Lidar information from CALIPSO to help constrain size distribution as well as vertical aerosol profile.
- Work by Cairns et al. (2005) has indicated that the addition of a channel near 2.1 microns may help constrain the large mode size distribution parameters with little sensitivity to the small mode. MODIS is a possible source of such a measurement in the A-train constellation. A measurement which shows preferential sensitivity to the large mode may prove extremely useful as some preliminary analysis has indicated that the sensitivity is dominated by the small mode due to the much larger number concentration of small particles in the aerosol sized distribution.

ACRONYMS

AOD: Aerosol Optical Depth

AVHRR: Advanced Very High Resolution Radiometer

CALIPSO: Cloud-Aerosol Lidar and Infrared Pathfinder Satellite Observation

CCN: Cloud condensation Nuclei

HITRAN: High resolution transmission molecular absorption database

LIDAR: Light Detection and Ranging

MISR: Multi-angle Imaging Spectroradiometer

MODIS: Moderate Resolution Imaging Spectroradiometer

NIR: Near Infrared

PARASOL: Polarization and Anisotropy of Reflectances for Atmospheric Sciences Coupled with Observations from a LIDAR.

POLDER: Polarization and Reflection of the Earth's Reflectances

SSA: Single Scatter Albedo

TOA: Top of the Atmosphere

REFERENCES

Asano, S. et al., 1995: Estimation of cloud physical parameters from airborne solar spectral reflectance measurements for stratocumulus clouds, *Journal of the Atmospheric Sciences*, **52**, 3556-3576.

Bohren, C. and D. Huffman, 1983: *Absorption and Scattering of Light by Small Particles*. John Wiley & Sons.

Chandrasekhar, S., 1960: *Radiative Transfer*. Dover Publications.

Chowdharry, J. et al., 2005: Retrieval of aerosol and absorption properties from photopolarimetric observations over the ocean during the CLAMS experiment, *Journal of the Atmospheric Sciences*, **62**, 1093-1117.

Cox C. and W. Munk., 1954. Measurements of the roughness of the sea surface from photographs of the Sun's glitter, *Journal of the Optical Society of America*, **44**, 838-850.

D'Almeida, G., P. Kopke and E. Shettle., 1991: *Atmospheric Aerosols: Global Climatology and Radiative Characteristics*. A. DEEPAK Publishing.

De Rooij, W. and C. van der Stap., 1984: Expansion of Mie Scattering Matrices in Generalized Spherical Functions, *Astronomy and Astrophysics*, **131**, 237-248.

Deuze, J. et al., 2000: Estimate of the Aerosol Properties over the Ocean with POLDER, *Journal of Geophysical Research*, **105**, 15329-15346.

Evans, K. and G. Stephens., 1991: A New Polarized Atmospheric Radiative Transfer Model, *Journal of Quantitative Spectroscopy and Radiative Transfer*, **46**, 413-423.

Hagolle, O. et al., 1999: Results of POLDER In-Flight Claibration, *IEEE Transactions on Geoscience and Remote Sensing*, **37**, 1550–1566.

Hansen, J. and L. Travis., 1974: Light Scattering in Planetary Atmospheres, *Space Science Reviews*, **16**, 527-610.

Ignatov, A and L. Stowe., 2000: Aerosol Retrievals from individual AVHRR channels. Part I: retrieval algorithm and transition from dave to 6S radiative transfer model, *Journal of the Atmospheric Sciences*, **59**, 313-334.

Ignatov, A. and L. Stowe, 2002: Aerosol retrievals from individual AVHRR channels. Part II: quality control, probability distribution functions, information content, and consistency checks of retrievals, *Journal of the Atmospheric Sciences*, **59**, 335-362.

Intergovernmental Panel on Climate Change (IPCC), 2001: *Climate Change 2001: The Scientific Basis. Contribution of Working Group I to the Third Assessment Report of the Intergovernmental Panel on Climate Change*, Edited by Houghton, J. T. et al., Cambridge University Press.

Kahn, R. et al., 2005: Multiangle Imaging Spectroradiometer (MISR) global aerosol optical depth validation based on two years of coincident Aerosol Robotic Network (AERONET) observations, *Journal of Geophysical Research*, **110**, 1-16.

Kaufman, Y. and D. Tanre., 1998: MODIS ATBD: Remote Sensing of Aerosol.

King, M. et al., 1999: Remote sensing of tropospheric aerosols from space: past, present and future, *Bulletin of the American Meteorological Society*, **80**, 2229-2259.

Koepke, P., 1984: Effective reflectance of oceanic white caps, *Applied Optics*, **23**, 1816-1824.

L'Ecuyer, T. et al., 2005 *accepted*: Cloud retrievals using MODIS from an information content perspective. Part I: liquid clouds, *Journal of Applied Meteorology*.

Liou, K., 1992: *Radiation and Cloud Processes in the Atmosphere*. Oxford University Press.

Liou, K., 2002: *An Introduction to Atmospheric Radiation*. Academic Press.

Morel, P., 1983: Optical modeling of the upper ocean in relation to its biogenous water content (case I waters), *Journal of Geophysical Research*, **93**, 10749-10768.

Rodgers, C., 2000: *Inverse Methods For Atmospheric Sounding: Theory and Practice*. World Scientific Publishing.

Rothman, L.S. et al., 2004: The HITRAN 2004 molecular spectroscopic database, *Journal of Quantitative Spectroscopy and Radiative Transfer*, **96**, 139-2004.

Schwartz, S., 2004: Aerosols, Clouds and Climate Change, *Nucleation and Atmospheric Aerosols*, Ed. M.Kashahara and M. Kulmala, Kyoto University Press, 323-338.

Spurr, R., 2004: A new approach to the retrieval surface properties from earthshine measurements, *Journal of Quantitative spectroscopy and Radiative Transfer*, **83**, 15-46.

Stamnes, K., S. Tsay, W. Wiscombe, and K. Jayaweera., 1988: Numerically stable algorithm for discrete-oridinate-method radiative transfer in multiple scattering and emitting layered media, *Applied Optics*, **27**, 2502-2509.

Stephens, G., 1994: *Remote Sensing of the Lower Atmosphere: An Introduction.* Oxford University Press.

Twomey, S., 1977: The influence of pollution on the shortwave albedo of clouds, *Journal of the Atmospheric Sciences*. **34**, 1149-1152.

Van De Hulst, H.C., 1981: *Light Scattering by Small Particles*. Dover Publications.

Wiscombe, W., 1976: Extension of the doubling method to inhomogenous sources, *Journal of Quantiative Spectroscopy and Radiative Transfer*, **16**, 477-489.

Wiscombe, W., 1980: Improved Mie scattering algorithms, *Applied Optics*, **19**, 1505-1509.